

Review

Conceptual models for partially premixed low-temperature diesel combustion

Mark P.B. Musculus*, Paul C. Miles, Lyle M. Pickett

Sandia National Laboratories, USA

ARTICLE INFO

Article history:

Received 4 October 2011

Accepted 23 August 2012

Available online 20 February 2013

Keywords:

Diesel engine

Emissions

Low-temperature combustion

Optical diagnostics

Conceptual model

ABSTRACT

Based on recent research within optically accessible engines and combustion chambers, conceptual models for low-temperature combustion (LTC) diesel engines are proposed. To provide a reference to which the LTC conceptual models may be compared, an established conceptual model framework for conventional diesel combustion is first reviewed and updated. Then, based on multiple optical diagnostic observations and homogeneous reactor simulations using detailed chemical kinetic mechanisms, extensions to the existing conceptual model are proposed. The LTC conceptual models are not intended to describe all LTC strategies, but rather a common subset of low-load, single-injection, partially premixed compression ignition conditions that are diluted by exhaust-gas recirculation to oxygen concentrations in the range of 10–15%. The models describe the spray formation, vaporization, mixing, ignition, and pollutant formation and destruction mechanisms that are consistent with experimental observations and modeling predictions for LTC diesel engines. Two separate subcategories are offered for either heavy-duty, large-bore or for light-duty, small-bore engines. Relative to the existing conventional diesel conceptual model, the features of the LTC conceptual models include longer liquid-fuel penetration, an extended ignition delay that allows more premixing of fuel, a more distinct and temporally extended two-stage ignition, more spatially uniform second-stage ignition, reduced and altered soot formation regions, and increased overmixing leading to incomplete combustion.

© 2013 Elsevier Ltd. All rights reserved.

Contents

1. Introduction	247
2. Background: conceptual model for conventional diesel combustion	249
3. Pre-combustion jet dynamics	250
3.1. Jet penetration and fuel vaporization during injection	252
3.2. Penetration and fuel vaporization after end of injection	252
4. Two-stage ignition phenomena	257
4.1. Chemical kinetics of ignition	258
4.2. Optical diagnostics of first-stage ignition	261
4.3. Optical diagnostics of second-stage ignition	263
5. Late-cycle processes	266
5.1. Soot oxidation	266
5.2. Late-injection PPCI UHC and CO emission sources	267
5.3. Early-injection PPCI UHC and CO emission sources	270
5.4. The impact of dilution	271
5.5. Experimental measurements of late-cycle UHC and CO	271
6. LTC conceptual models and summary	274
6.1. Single-injection, EGR-diluted PPCI in heavy-duty engines	274
6.2. Single-injection, EGR-diluted conditions in light-duty engines	277
7. Concluding remarks	281

* Corresponding author. Engine Combustion Department, Sandia National Laboratories, PO Box 969, Livermore, CA 94551-0969, USA. Tel./fax: +1 925 294 3435.
E-mail address: mpmuscu@sandia.gov (M.P.B. Musculus).

Acknowledgments	281
Nomenclature	281
References	281

1. Introduction

The past two decades have witnessed drastic reductions in regulated limits for pollutant emissions from diesel engines. For example, heavy-duty engine emissions limits in the United States [1], the European Union [2–4], and Japan [5] for particulate matter (PM), nitrogen oxides (NO_x) and unburned hydrocarbons (UHC) in the early 2010s are only 2%, 3–12%, and 6–12%, respectively, of their 1990 levels. Comparable reductions were also required in the light-duty sector [5,6]. Likewise, in China and India, the evolution of emissions regulations for both heavy- and light-duty diesel engines from 2000 through 2010 required reductions of similar magnitudes, mirroring the Euro I through Euro IV regulatory limits, though at an accelerated pace [5].

Historically, the earlier emissions targets were achieved for the most part without exhaust-gas aftertreatment. In-cylinder strategies utilizing higher fuel injection pressure, higher intake boost, lower intake temperatures, adjustments to fuel injection timing, low to moderate levels of exhaust-gas recirculation (EGR), and improved combustion chamber design were sufficient [7]. The later targets, however, have been achieved or are expected to be achieved through a combination of both in-cylinder strategies and aftertreatment devices. After years of research and development, viable aftertreatment technologies are now available, but their widespread adoption is impeded by higher economic costs, durability issues, fuel economy penalties, and greater space requirements compared to engines without aftertreatment [8]. Consequently, improvements to in-cylinder strategies to further reduce the engine-out emissions and thereby lessen the aftertreatment burden are of great interest.

Reduction of NO_x is a significant challenge for diesel exhaust aftertreatment; hence, in-cylinder strategies that address NO_x emissions have been widely investigated. In diesel engines, NO_x is formed primarily by the thermal (Zeldovich) mechanism, wherein production rates increase exponentially with temperature [9–11]. Accordingly, recent research into in-cylinder strategies for NO_x emissions reduction has largely focused on strategies to reduce in-cylinder combustion temperatures. Such strategies can be broadly classified as low-temperature combustion (LTC). In all LTC strategies, the combustion temperatures are reduced by dilution of the in-cylinder combustible mixtures, either with excess charge gas to create mixtures that are more fuel-lean than stoichiometric, or with moderate to high levels of EGR. In either case, the diluent gases increase the fuel-specific heat capacity of the combusting mixtures, thereby reducing the combustion temperatures. In the case of dilution by EGR, the oxygen concentration is also decreased, which further slows NO_x formation kinetics.

In addition to reductions in NO_x formation rates, the formation kinetics of soot, a primary component of PM, are also slowed by reducing combustion temperatures [12,13]. At the same time, however, the in-cylinder soot oxidation rates decrease with temperature and oxygen concentration even more than formation rates [14,15]. As a result, net PM emissions typically increase as EGR is added, at least initially [16–18]. At very high EGR rates, soot formation can become so low that PM emissions decrease even with reduced oxidation [15–19]. Unfortunately, combustion efficiency is poor at such extreme EGR rates, and UHC and carbon monoxide (CO) emissions become excessive well before soot

formation is substantially inhibited [17,20]. Rather than using such extreme EGR rates, most LTC strategies address PM emissions by increasing pre-combustion mixing. Soot forms during and after combustion in regions that are more fuel-rich than stoichiometric, so increasing mixing prior to combustion can reduce or eliminate the soot-forming, fuel-rich mixtures [21].

Numerous LTC strategies with various names and acronyms have been proposed in investigations in the literature. In recent years, the defining characteristics of the various strategies have become less distinct as they have evolved and/or broadened so that they overlap with each other. For the purposes of this discussion, the LTC strategies can be broadly categorized into two groups, according to the degree of premixing.

For one category, which falls within the strategy often termed “homogeneous-charge compression ignition” (HCCI),¹ vaporized fuel is well mixed with the charge gas prior to compression, and is everywhere fuel lean [22]. The fuel may be delivered either external to the combustion chamber during or prior to induction, or by direct-injection during the intake stroke or very early in the compression stroke. HCCI strategies typically employ long in-cylinder mixing times prior to combustion, or even external mixing strategies (e.g., intake port injection), to produce relatively uniform, fuel-lean mixtures throughout, often with minimal use of EGR, especially at low-load. Ignition timing is kinetically controlled, and is therefore decoupled from the timing of the fuel injection event. As it has matured, most practical HCCI applications have evolved from early uses of very uniform mixtures to intentionally inhomogeneous charge gas mixtures and temperatures for better control of heat release rate [23]. Even for “inhomogeneous” HCCI strategies, however, mixtures are everywhere fuel lean, and by this definition, they are not the subject of this work.

This work focuses on the other broad category, here termed “partially premixed compression ignition” (PPCI),² which uses direct injection with more moderate mixing times. Here, the distinction between PPCI and HCCI is that the charge distributions for PPCI are more heterogeneous at ignition than HCCI, and include not only fuel-lean but also fuel-rich mixtures. Low combustion temperatures are achieved by employing EGR. Ignition is also more closely coupled to the fuel injection event than with HCCI, though chemical kinetics still play an important role.

To provide time for sufficient premixing before ignition, fuel injection in PPCI strategies must be advanced farther from ignition compared to conventional diesel conditions. For conventional diesel conditions, fuel injection is typically slightly before top-dead-center (TDC) and ignition usually occurs before the end of injection. Conventional diesel combustion therefore usually has a negative ignition dwell, which is the time from the end of injection to ignition. As a result, only a portion of the injected fuel is premixed prior to initiation of combustion. For PPCI LTC strategies, the ignition dwell is usually positive, which provides time for some degree of premixing for all of the injected fuel, including fuel from the very end of injection. A positive ignition dwell is typically

¹ The term “HCCI” has frequently been applied very broadly in the literature to include strategies that would be characterized here as PPCI.

² Other terms include “Premixed-Charge Compression Ignition (PCCI)” and “Premixed Compression Ignition (PCI)”.

achieved with high EGR rates, which delay ignition. Shorter injection durations also help to achieve a positive ignition dwell, so that PPCI LTC strategies are typically employed for low-load operation. Long ignition dwell times can also lead to excessive pressure rise rates and noise at high fueling rates, which also limits PPCI LTC strategies to lower loads.

The PPCI LTC strategies may be further divided into two subcategories according to the fuel-injection and combustion timing, which is either earlier or later than for conventional diesel combustion. Some studies have investigated early-injection PPCI, where fuel is injected in the middle to late compression stroke [17,24–37]. Other studies have explored late-injection PPCI, which includes Nissan's "Modulated Kinetics" (MK) regime [38,39], for which fuel is injected very near TDC or in the early expansion stroke [17,33–43]. In either case, compared to conventional diesel injection timing, the gases into which the fuel is injected are either initially cooler and less dense because of less compression (for early-injection PPCI), or become cooler during and after injection because of expansion (for late-injection PPCI). Combined with the ignition-delaying effects of EGR, the pre-ignition chemistry is slowed to provide greater pre-combustion mixing than conventional diesel combustion.

Although PPCI LTC strategies are attractive because they have been demonstrated to achieve engine-out compliance with stringent emissions limits for NO_x and PM, other emissions, including CO and UHC emissions, often exceed regulated limits [17,25–33,35–37,40,42,43]. Combustion noise, associated with a rapid rise of the in-cylinder pressure, can also impose constraints on the required dilution or injection timing, driving further increases in CO and UHC. As a consequence of the increased CO and UHC emissions, as well as non-optimal heat release phasing, fuel consumption can be higher than for conventional diesel conditions [24–27,31,32,34,36,37,40].

Typical, light-load emissions behavior observed for both early- and late-injection PPCI LTC strategies, in both light-duty [17] and heavy-duty engines [34,37], is shown in Fig. 1. In the upper-left portion of the figure, the emissions behavior and maximum pressure rise rate are shown for light-duty, early-injection PPCI combustion as the charge O₂ concentration is varied (by adjusting the EGR rate). At this light load, PM emissions are small and NO_x emissions are limited to acceptable levels with O₂ concentrations below ~15%. With this dilution rate, the CO and UHC emissions are reasonably low. The pressure rise rate is excessive, however, and to restrain it within reasonable limits (~5–10 bar/°) the EGR rate must be increased, leading to increased CO and UHC emissions. Note that, when expressed on an energy content basis, the CO emissions are responsible for a greater part of the loss in combustion efficiency than UHC, and CO emissions increase more rapidly than the UHC emissions as the O₂ concentration is decreased. The lower-left portion of Fig. 1 shows corresponding behavior observed in a heavy-duty-engine, although for a more limited range of intake charge O₂ concentrations. Similar behavior is observed in other studies (e.g., [16]), though the engine loads investigated were typically somewhat higher.

Emissions and cylinder-pressure rise-rates for late-injection PPCI operation are shown on the right-hand side of Fig. 1. PM emissions increase as the start-of-injection (SOI) is retarded, reaching a peak near TDC and then falling rapidly with additional injection retard. Even at the PM peak, emissions are within reasonable limits. NO_x emissions decrease when SOI is retarded beyond ~−20°, and reach acceptable levels in the light-duty engine when SOI is later than ~−10°. At this injection timing, UHC and CO emissions begin to rise, but are still at tolerable levels. Once again, however, the pressure rise rate is quite high. Further retarding the timing to ~0° is required to achieve rise rates less than 5 bar/°, at which point the CO and UHC emissions become problematic. Note

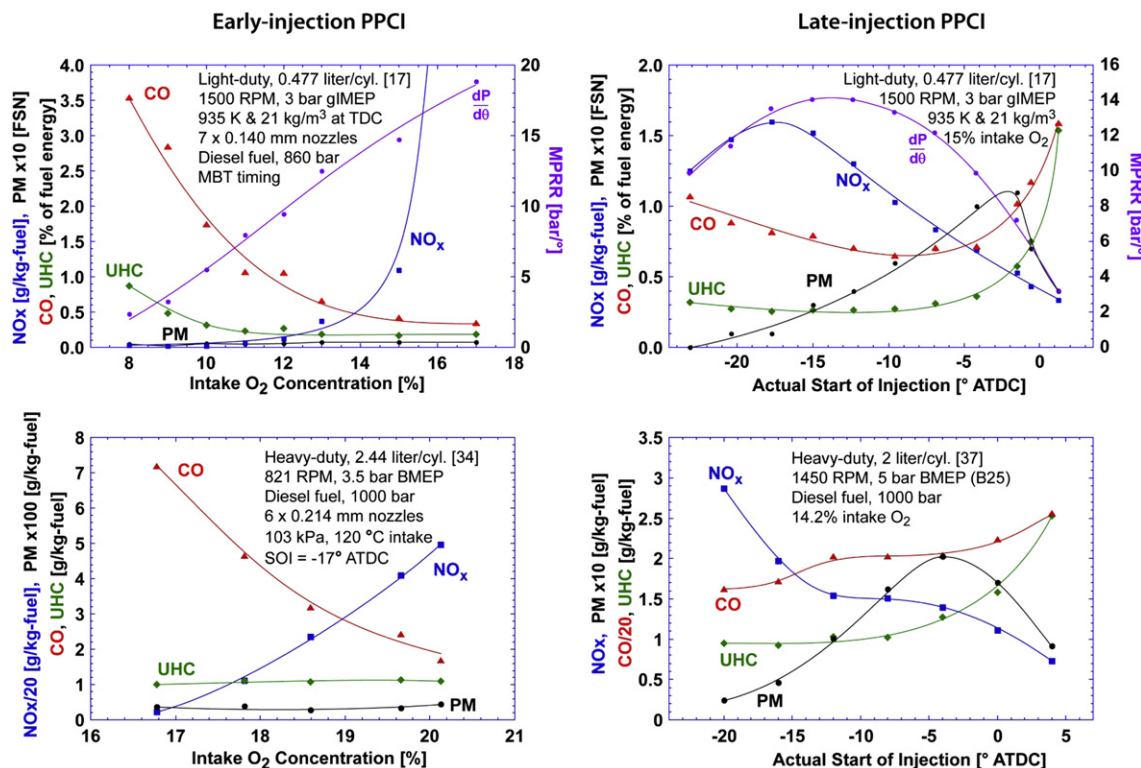


Fig. 1. Emissions and cylinder-pressure rise rates measured for both early-injection (left) and late-injection (right) PPCI LTC operation in light-duty (top) and heavy-duty (bottom) engines. Reprinted with permission, SAE papers 2008-01-1658 (c) 2008 and 2003-01-0341 (c) 2003, SAE International.

that, as with early-injection PPCI operation, the bulk of the energy loss associated with incomplete combustion is tied to the CO emissions. In contrast to the early-injection behavior, though, the UHC emissions rise much more rapidly than the CO emissions as combustion is further retarded. Heavy-duty engines again exhibit similar behavior, as shown in the lower-right portion of the figure, with UHC emissions increasing considerably more rapidly than CO as SOI is retarded to just a few degrees after TDC [34,37].

To realize the full potential of either early- or late-injection PPCI LTC strategies, the in-cylinder physical and chemical mechanisms leading to the emissions behavior described above must be well understood. For conventional diesel combustion, significant insight into the in-cylinder spray, ignition, combustion, and pollutant-formation processes has been provided by optical diagnostic techniques. Based on observations made using these diagnostics, several conceptual models have been proposed for conventional quasi-steady diesel combustion [44–50]. In particular, Dec proposed a conceptual model for conventional diesel combustion in 1997 [44]. His conceptual model has proven useful as a foundation for understanding and modeling the in-cylinder processes responsible for conventional diesel engine performance and pollutant emissions characteristics.

The objective of this work is to offer extensions of Dec's conceptual model for typical EGR-diluted low-load PPCI LTC conditions, similarly based on optical diagnostic observations. Additionally, following the approach of Flynn and co-workers [51] for conventional diesel combustion, the experimental observations are complemented by homogeneous reactor simulations using detailed chemical kinetic mechanisms that serve to clarify the impact of finite-rate chemistry on the ignition and combustion process for PPCI LTC conditions. The proposed LTC conceptual models are not intended to describe all LTC strategies, but rather a common subset with the following characteristics:

1. LTC is achieved by EGR, with intake oxygen concentrations in the range of 10–15%. Under such dilution levels, combustion temperatures are still high enough that soot may form in fuel-rich mixtures.
2. Fuel injection timing may be either early- or late-injection PPCI. In either case, the ignition dwell is positive so that fuel is partially premixed before combustion. The ignition dwell is short enough, however, that ignition is still somewhat coupled to the fuel injection timing, and the residual jet structure is often still intact at ignition.
3. The fuel injector uses conventional small-orifice diesel nozzles to produce typical diesel-like sprays (e.g., spray is not hollow cone).
4. Fuel is delivered in a single-injection event (no pilot, split, or post injections).
5. Fuels are diesel-type, with two-stage ignition chemistry (not gasoline-like fuels).

The proposed LTC conceptual models are a synthesis of various current experimental and modeling studies. Within the engine research community, a wide range of operating conditions have been explored to achieve LTC. Compiling and comparing bits of information from so many disparate investigations to form a coherent picture describing LTC processes is hindered by differences in operating conditions that affect observations and results. To provide a more consistent basis for the conceptual model, we feature examples of research from studies using operating conditions as similar as possible, many of which were performed in multiple facilities at our own laboratory. Following these more detailed examples, we also provide a more general review of observations from the literature for each topic.

2. Background: conceptual model for conventional diesel combustion

This section provides a brief summary of the conceptual model for conventional diesel combustion proposed in 1997 by Dec [44], upon which the extension for low-load PPCI LTC is built. A few additional elements, provided by subsequent studies relevant to the conceptual model description, are also included in the description. The original conceptual model applies to conventional diesel conditions, having a single-injection, little or no EGR, and a negative ignition dwell with fuel injection shortly before TDC. Fuel injection is also typically long enough that much of the fuel burns during mixing-controlled combustion, so that the combustible jet experiences a significant “quasi-steady” period, with some fuel burning as more fuel continues to be injected. Fig. 2 is a schematic illustration of the important elements of the conventional diesel jet during the quasi-steady period. (For the jet evolution prior to the quasi-steady period, Figs. 30–32 include additional schematics, which are used later in the discussion of the LTC conceptual models). The evolution of in-cylinder processes leading to the quasi-steady period is briefly reviewed below.

In conventional direct-injection diesel engines, liquid fuel is injected at high pressure (~100 MPa) through multiple orifices (~0.2 mm diameter) forming sprays of droplets emanating from each hole of the fuel injector. The spray from each hole penetrates into the combustion chamber, expanding into a roughly conical jet as the volume of in-cylinder gases entrained into the jet increases with downstream distance from the injector. Entrainment correlations [52–54] predict that increasing entrainment downstream causes the equivalence ratio to vary along the jet axis approximately inversely with the downstream distance, and direct fuel vapor measurements [55] confirm this prediction. Here, the equivalence ratio is defined as the ratio of the local fuel-ambient charge mass ratio to the stoichiometric fuel-ambient mass ratio. The thermal energy provided by the entrained in-cylinder gas heats and vaporizes the liquid fuel. At some location downstream of the injector, termed the “liquid length”, all of the fuel enters the vapor phase [52,56,57]. The liquid length can be reliably predicted using an entrainment correlation to find the downstream location where the fuel-ambient ratio is such that the thermal energy added to the jet by the entrained gas is just sufficient to fully-vaporize the fuel [56,58]. The success of these predictions implies that for high-pressure diesel injection, vaporization is limited by mixing (i.e., entrainment), not by droplet atomization and vaporization processes.

In the long-time limit of injection durations greater than a few hundred microseconds, the penetration rate scales as $\rho_d^{-0.35}$ [52],

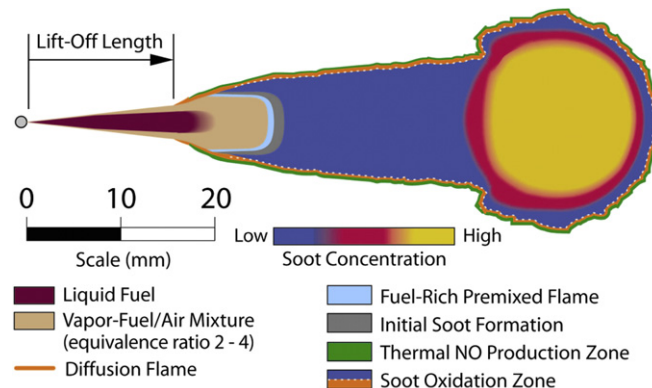


Fig. 2. Schematic of Dec's conceptual model for conventional diesel combustion during the quasi-steady period of diesel combustion [44]. Reprinted with permission, SAE paper 970873 (c) 1997, SAE International.

where ρ_a indicates the ambient density. Consequently, higher density (boosted operation or injection near TDC) will slow the penetration of the fuel jet. The liquid length also is reduced as the ambient density increases, scaling with $\rho_a^{-0.7}$ [56].

After the fuel is fully vaporized, momentum carries the fuel-ambient mixture downstream of the liquid length where it continues to entrain more of the hot in-cylinder gases. First-stage ignition reactions then commence, as indicated by weak chemiluminescence and fluorescence of intermediate reaction species such as formaldehyde [47,50,59,60]. A short time ($\sim 100\text{--}200\ \mu\text{s}$) after chemiluminescence from the initial ignition reactions is first detected, the reactions evolve into a highly exothermic second stage of ignition, leading to the “premixed burn” phase of diesel combustion. As the temperature rises, polycyclic aromatic hydrocarbon (PAH) soot-precursor species quickly form in the hot ($\sim 1600\text{--}2000\ \text{K}$) fuel-rich combustion products of the premixed burn. Soot formation follows, filling the entire downstream jet cross section.

Near the peak heat release rate of the premixed burn, a diffusion flame forms on the periphery of the fuel-rich, high-temperature downstream region of the jet. Nitrogen oxides form in the hot, near-stoichiometric mixtures on the periphery of the jet, near the diffusion flame. The upstream edge of the diffusion flame does not extend fully to the injector nozzle, but rather it remains some distance downstream, termed the “lift-off length” [61,62]. Because the flame is lifted, fuel and air are premixed upstream of the diffusion flame, and Dec hypothesized that a standing premixed reaction zone would form near the lift-off length, as depicted in Fig. 2. Later studies in other facilities showed formaldehyde forms upstream of the lift-off length in the jet cross section and is consumed downstream of the lift-off length, consistent with such a standing premixed reaction zone [48,50]. Combustion products leaving this premixed reaction zone, combined with hot products entrained from the diffusion flame, increase temperatures within the fuel-rich core of the jet. Hence, in addition to the soot formed as a result of the premixed burn, additional soot continues to form in the hot fuel-rich core of the diesel jet during the quasi-steady period. As fuel injection continues, soot persists throughout the

downstream jet cross section, from somewhat downstream of the lift-off length to the head of the jet. After the initial transient of the jet penetration and ignition processes, but before the end of injection, the diesel jet enters a “quasi-steady” period—when the characteristic description of the combusting jet does not change (Fig. 2).

During the quasi-steady period, the magnitude of the lift-off length is critical for soot formation. Upstream of the lift-off length, oxygen in the entrained gases mixes with the vaporized fuel prior to reaction in the standing premixed combustion zone. The amount of entrainment upstream of the combustion zone increases with increasing lift-off length, so that the equivalence ratio of the mixture entering the standing premixed combustion zone decreases with increasing lift-off length. The magnitude of the lift-off length and the equivalence ratio at the lift-off length are affected by many factors, including ambient gas temperature, density, and oxygen concentration, injection pressure and orifice size, as well as fuel properties [62,63]. Soot formation decreases as the equivalence ratio (ϕ) at the lift-off length decreases, and below a threshold near $\phi = 2$ at the jet centerline, no soot forms in the jet [55,62]. Under typical diesel conditions, the equivalence ratio at the lift-off length is well above the threshold for soot formation, so that the jet is typically filled with soot, as depicted in Fig. 2.

3. Pre-combustion jet dynamics

Beginning with this section, experimental observations and homogeneous reactor simulations that serve as the basis for the LTC conceptual model for low-load, single-injection, EGR-diluted, partially premixed low-temperature direct-injection (DI) diesel combustion (PPCI LTC) are presented. The experimental images are acquired from multiple engine and combustion chamber facilities with optical access, using various optical diagnostic techniques. Fig. 3 shows examples of one heavy-duty optical engine (left) and one constant-volume combustion vessel with optical access (right). The optical engine has windows placed in the piston crown and cylinder head to provide imaging access, and windows located around the top of the cylinder-wall provide cross-optical access for

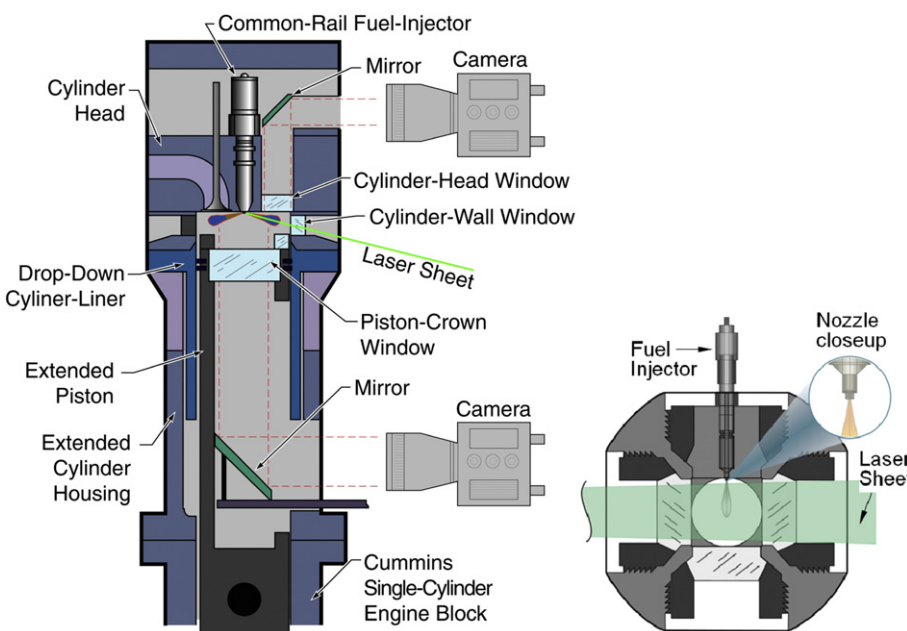


Fig. 3. Representative schematics of an optical engine (left) and a constant-volume combustion chamber (right), showing optical access for laser diagnostics and cameras for imaging.

laser diagnostics. Light-duty, smaller-bore optical engines are similar, although greater fidelity in preserving the geometry of the piston bowl is required due to the importance of the interactions between the fuel jets and the bowl walls. The constant-volume vessel in Fig. 3 has a cubical combustion chamber 108 mm on each side, with optical access provided by side-port sapphire windows. A single-orifice, common-rail fuel injector is mounted at the center of a metal side-port such that the diesel spray is directed into the center of the chamber. Some images presented herein are from these two facilities, and other images are from other similar facilities. Due to space considerations, complete details of the experimental facilities and methods are not provided here, but these details may be found in the references provided in the discussion of each topic area considered below.

A series of images showing the initial penetration of liquid and vapor fuel for an early-injection PPCI LTC condition at a load of 4 bar gross indicated mean effective pressure (gIMEP) in a heavy-duty engine are assembled in Fig. 4. The operating conditions are noted in the figure. The white dot on the left side of the images

indicates the injector location, and the portion of the piston bowl-wall within the field of view is indicated by the curved white line. As indicated by the scale at the bottom of the images, the piston-bowl radius is approximately 50 mm, and the cylinder wall radius is 69.5 mm (outside field of view, to the right). Co-planar laser sheets of two different wavelengths are used to illuminate the fuel jets. Although eight fuel jets issue from the injector, only one of them, the central, horizontal jet penetrating from left to right, is fully illuminated by the 30-mm wide laser sheets, the edges of which are delimited by the horizontal dashed lines. The other seven jets are only partially illuminated. The timing of each image, in crank angle (CA) degrees after the start of injection (ASI), is indicated at the top left of each image.

The grayscale images show the broadband diesel-fuel fluorescence from laser excitation at 284 nm using a thin sheet propagating from right to left, and aligned along the jet axis (14° angle from the firedock). The fluorescence signal can arise from both liquid and vapor fuel, so some parts of the grayscale images represent both liquid and vapor fuel. Diesel fuel absorbs ultraviolet

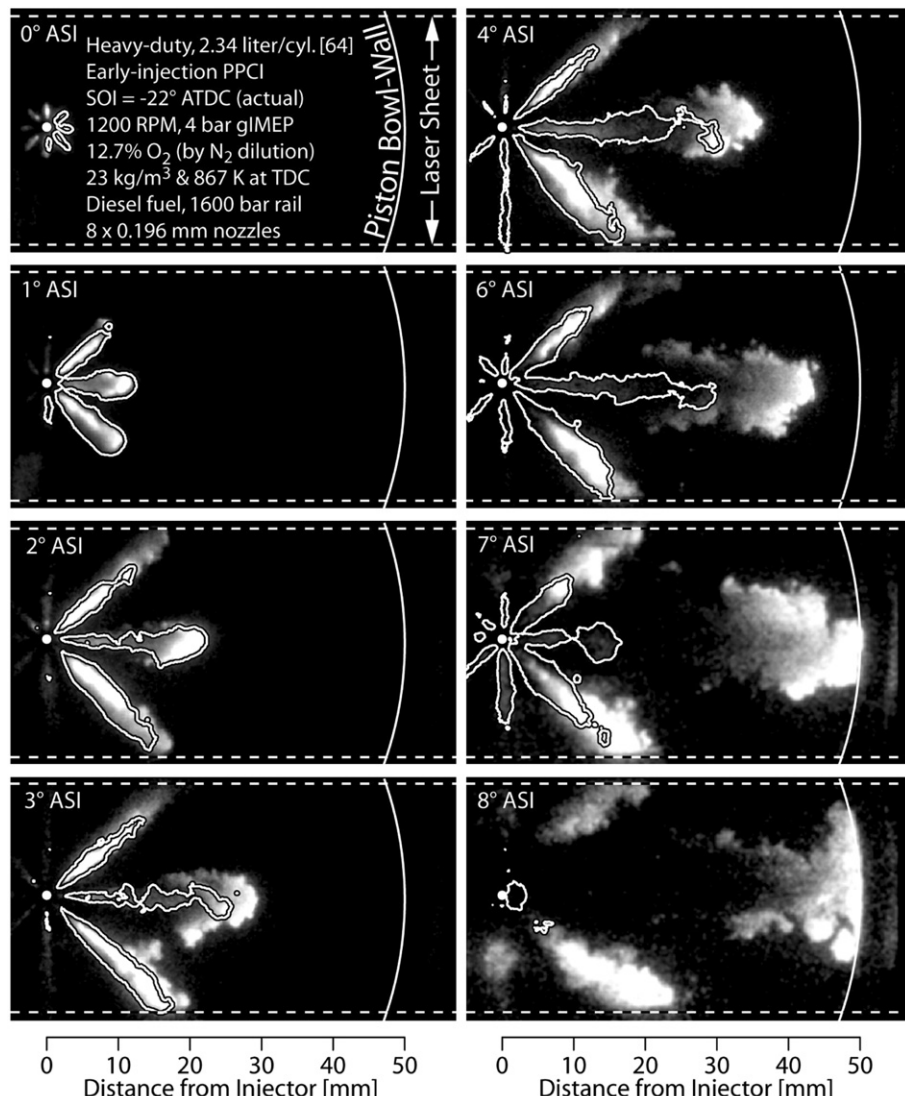


Fig. 4. Fuel fluorescence from both liquid and vapor diesel fuel (grayscale, significant attenuation) and Mie-scattered light from liquid-fuel only (contours) observed for an early-injection PPCI operating condition in a heavy-duty engine [64]. The curved white line is the piston bowl-wall (49 mm radius), and the laser sheet (dashed lines) propagates from right to left along the axis of the jet penetrating to the right. The final, definitive version of Fig. 4 has been published in International Journal of Engine Research, 8(1), 2007 by SAGE Publications Inc., All rights reserved. © <http://jer.sagepub.com/content/8/1/97.full.pdf>.

light very strongly, and the ultraviolet laser sheet is appreciably attenuated by fuel on the right side of the images where the laser sheet enters. As a result, fuel on the left side of the image is often not well illuminated by the ultraviolet laser light, especially for the later images. The fluorescence signal in many images is therefore dominated by fuel at the leading edge of the jet. Due to this strong attenuation, as well as other factors, the intensity of the fluorescence emission should not be interpreted as an indication of the local fuel concentration. Instead, interpretation of the grayscale images should focus on the spatial and temporal evolution of the leading edge (right side) of the penetrating fuel jet.

In addition to the fuel fluorescence imaging, a simultaneous visualization of liquid fuel is provided by images of elastic Mie scattering of laser light at 532 nm. Light at 532 nm is not absorbed nearly as strongly as ultraviolet light, so that liquid scattering images do not suffer from the attenuation in the fluorescence imaging described in the preceding paragraph. Hence, reliable liquid fuel signals are acquired throughout the images. The liquid fuel images are not shown directly, but have been reduced to a contour line indicating the outer edge of the liquid fuel spray, which is overlaid on the grayscale fluorescence images. There is significant background scatter from engine surfaces (e.g., cylinder head, valves) in the raw images, so to improve clarity in the composite images, the contour level for the liquid fuel images is set to 35% of full scale. The scattered light intensity drops off rapidly near the liquid length [65], so the liquid boundary at the 35% contour agrees with visual inspection of the liquid length, to within a few mm. Comparison of the liquid-fuel contours and the fluorescence images provides an indication of the relative spatial distribution of liquid and vapor fuel. That is, the fluorescence signal (grayscale) arising from within the contours may be due to both liquid- and vapor-fuel fluorescence, while the grayscale fluorescence outside of the contours is mainly from vapor fuel.

3.1. Jet penetration and fuel vaporization during injection

The initial fuel jet penetration displayed by the liquid-fuel contours and the grayscale fluorescence images in Fig. 4 is similar to that of conventional diesel combustion. The initial penetration rate, however, is somewhat faster, primarily because the injection pressure in the LTC experiments (1600 bar [64]) was much higher than in the conventional diesel experiments (600 bar pressure [66]) upon which Dec based his conceptual model [44]. From 4° ASI to 6° ASI, the liquid-fuel penetration remains approximately constant, as the liquid length of 30–35 mm is established for this condition. For conventional diesel conditions, with injection closer to TDC into hotter and more dense gases, the liquid length is somewhat shorter, typically 20–25 mm, and will be even shorter for highly boosted conditions [66]. Conversely, for other LTC strategies with even earlier injection, or with lower in-cylinder densities (e.g., lower boost or lower compression ratio), the liquid length will extend much farther, such that liquid fuel may impinge on in-cylinder surfaces (as discussed in the next sub-section). In smaller bore, light-duty engines featuring bowl rim radii of 20–25 mm, liquid impingement can easily occur.

The vapor fuel (grayscale) initially penetrates together with the liquid fuel, but by 3° ASI and later, as the liquid length is established, the vapor fuel penetrates downstream of the liquid. As described above, because of laser-light attenuation, the upstream vapor fuel (left side of image) is not well illuminated by the laser, so that only the vapor fuel near the leading edge (right side of image) of the central, horizontal jet is apparent in the grayscale fluorescence images, especially after 3° ASI. The upstream portions of the jets on either side of the horizontal jet, however, are partially illuminated by the laser sheet, which provides an indication of the

upstream fuel distribution. For example, at 6° ASI in Fig. 4, the leading edge of the horizontal jet has penetrated nearly 45 mm downstream, but the upstream fluorescence signal, within about 30 mm of the injector, is weak or non-existent in this horizontal jet. The partially illuminated jets on either side, however, show significant fluorescence within 30 mm from the injector, showing that fuel still remains in the upstream regions of the jets.

3.2. Penetration and fuel vaporization after end of injection

For the injection event in Fig. 4, the injection rate peaks at about 5° ASI, and injection ends near 7° ASI, after a ramp-down of about 2°, which is approximately 300 µs at 1200 rotations per minute (RPM). For this operating condition and injector, as the injection rate ramps down and ends, the liquid fuel penetration (contour line) becomes shorter. Within only 1° after the end of injection, by 8° ASI, the liquid penetration length essentially decreases to zero, and almost no liquid fuel remains in any of the jets.

For operating conditions with cooler and less-dense ambient gases, or with faster end-of-injection ramp-down rates, the liquid fuel behavior during and after the end-of-injection transient can be very different. For example, Fig. 5 shows liquid-fuel Mie-scatter images from a cooler, lower ambient-density condition [67]. In Fig. 5, the grayscale indicates the Mie-scattering signal level, rather than a fluorescence signal level, and the contour shows the outer boundary of the liquid-fuel. The Mie-scatter images in Fig. 5 were acquired from a single-hole injector (on the left side of the images) in a constant-volume combustion chamber (Fig. 3) at the ambient conditions indicated in the figure. For these conditions, the injection duration is short enough that liquid fuel never reaches the quasi-steady liquid length, which is indicated for reference by a dashed line at the right of the images. The end-of-injection ramp-down is also relatively short, with a duration of approximately 100 µs (~0.7° at the engine speed of Fig. 4).

With a relatively fast end-of-injection ramp-down, and the cool, low ambient density, the maximum liquid-fuel penetration length does not retreat back to the injector during and after the end of injection as in Fig. 4. Instead, after the end of injection at 360 µs ASI,

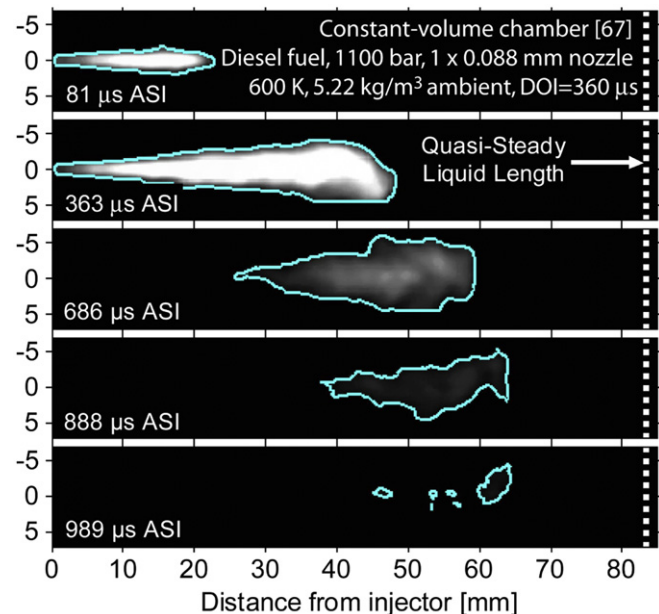


Fig. 5. Liquid diesel-fuel images at low ambient density in a constant-volume chamber [67]. The mean quasi-steady liquid length achieved with a long injection event is overlaid as a dashed line.

the liquid fuel detaches from the injector, and liquid fuel remains downstream until about 1000 μs ASI.

Clearly, comparison of Fig. 4 with Fig. 5 shows that ambient conditions and injector dynamics can alter the liquid fuel vaporization behavior after the end of injection. Furthermore, operating conditions intermediate between those of Figs. 4 and 5 can produce liquid fuel distributions that split after the end of injection, with liquid fuel remaining for a short time both near the injector and far downstream, but with a liquid-free gap near the middle [67].

An example of such a split liquid fuel distribution, observed in a light-duty engine operating in an early-injection PPCI combustion regime, is shown in Fig. 6 at a timing shortly after the end of injection. The fuel injector is the same as that used to obtain the images shown in Fig. 5, but is fitted with a conventional multi-hole nozzle. To obtain this image, a vertical laser sheet aligned with the jet axis is introduced through a window in the cylinder liner, and Mie-scattered light is collected and imaged. Image distortion due to curvature of the piston bowl and cylinder liner window is corrected using transformations derived from images of calibration targets. Although the most intense light scattering is observed near the injector, distinct regions of liquid fuel are found both in the clearance volume and in the bowl. Liquid in the clearance volume forms films along the piston top and the head that are detected later in the cycle in images of unburned hydrocarbons obtained with laser-induced fluorescence.

The curious vaporization behavior of liquid fuel after the end of injection suggests that mixing processes change significantly after the peak in the fuel injection rate. As described earlier, prior to the end of injection, the liquid fuel penetration length may be reliably predicted by finding the downstream location in the jet where a sufficient amount of energy has been entrained with the hot ambient gases to completely vaporize the fuel. If vaporization is similarly limited by entrainment and mixing after the end of injection, then upstream vaporization of liquid fuel in Figs. 4 and 5 implies that upstream mixing (i.e., fuel-specific entrainment) must increase after the end of injection. Indeed, in single-phase jets, which are analogous in many ways to diesel jets, it has been long recognized that the mixing rate per unit of fuel injected increases during periods of injection rate decreases (and vice versa) [68–74].

Though the fuel vaporization behavior demonstrates that mixing changes as the injection rate decreases, it is not immediately apparent if the fuel-specific entrainment rate increases because the entrainment increases, or if the entrainment rate decreases, but only less rapidly than the fuel delivery (e.g., the entrainment rate may remain relatively constant for some period as injection is ending). To explore the theoretical entrainment behavior after the end of injection, a simplified one-dimensional numerical jet model

was developed [75]. The model was based on a previously-developed analytical entrainment correlation [52,56] that reliably predicts diesel jet penetration, entrainment, and the quasi-steady liquid length. The new model extends the correlation by incorporating spatial and temporal discretization to allow for non-steady injection rates. Model predictions for starting and quasi-steady jets agree with previously established analytical model predictions [52,56] and, using a number of empirically based [75] assumptions about the jet geometry (e.g., spreading angle) during and after the end of injection, the one-dimensional jet model also predicts entrainment during these periods.

Fig. 7 shows normalized entrainment-rate predictions of the model after the end of injection for ambient conditions similar to those of Fig. 4. Each curve is for a different time after the end of injection (AEI). The curves show the entrainment rate along the jet axis, relative to the entrainment rate for a steady jet. Thus, a value of unity indicates the same entrainment rate as a steady jet, and values greater than unity indicate an increase in entrainment over a steady jet. For illustrative purposes, the injection rate profile used in the simulation features an instantaneous ramp-down ("top-hat" injection profile), which creates a stronger entrainment rate increase after the end of injection compared to slower ramp-down rates.

The model predicts that when the fuel flow from the injector stops, an axial mass flux deficit arises near the injector. The axial mass flux deficit arises because the model assumes a constant jet spreading-angle, even as injection ends, which is consistent with multiple experimental observations (as described in [75]). Hence, continuity requires that the ambient gas entrainment must increase to compensate for the reduced mass flux at the nozzle. After this initial increase in entrainment, momentum exchange between the jet fluid and the low-momentum ambient gases further reduces the local axial velocities in the jet, which reinforces the mass flux deficit, driving yet more entrainment. This process builds and propagates downstream as a wave of increased entrainment. The model predicts that this "entrainment wave" grows as it propagates downstream, asymptotically approaching a peak entrainment-rate increase of a factor of three at the head of the entrainment wave. The local fluid dynamical processes responsible for increasing entrainment while maintaining a relatively constant spreading angle are complex and not well understood. Recent large-eddy simulations (LES) of transient high-speed gas-jets, which are in many ways analogous to diesel jets, predict that the separation between large flow structures increases during and after the ending transient [76]. Ambient fluid is entrained between the large structures as they separate from one another, while the outer envelope of the structures (i.e., the spreading angle) remains relatively constant.

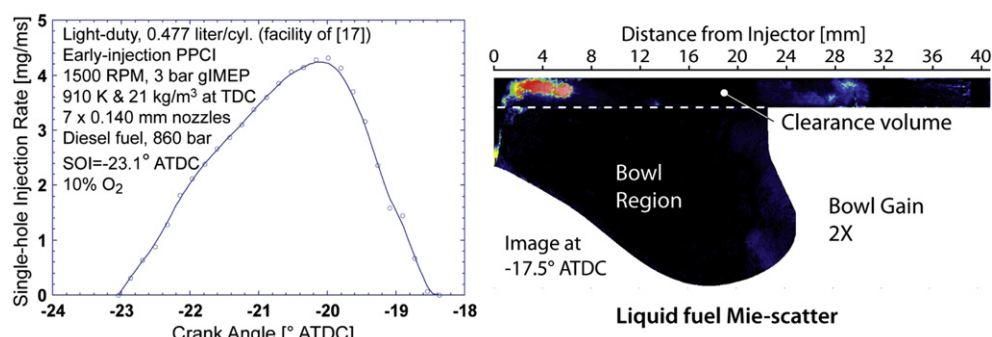


Fig. 6. Right: Mie-scatter liquid-fuel image shortly after end of injection for early-injection PPCI in a light-duty engine (unpublished, obtained in same engine as Ref. [17]). The image was acquired in two parts; clearance-volume and bowl-region images were selected from separate engine cycles and assembled into the full image to represent the maximum liquid penetration. Left: Corresponding rate of injection.

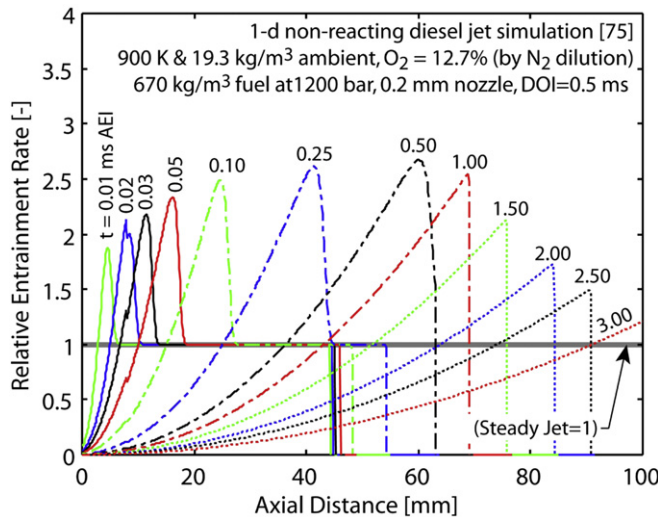


Fig. 7. The entrainment rate relative to a steady jet predicted by the one-dimensional jet model for ambient conditions similar to those of Fig. 4 [75]. Each curve is labeled by the corresponding time after the end of injection.

The model predicts that the enhanced entrainment is not sustained indefinitely, however. After the passage of the entrainment wave, momentum exchange with the low-momentum ambient gases gradually reduces the axial velocity of the jet, so that it becomes stagnant, with entrainment falling below that of a steady jet, eventually approaching zero at long times after the end of injection. Despite the decreased entrainment rate, however, local equivalence ratios also decrease as a result of the decreased fuel flux. The net result is that the entrainment rate per unit of fuel, which can be interpreted as a mixing rate, remains significantly higher after the passage of the entrainment wave compared to the steady jet.

The same range of conditions where experiments showed that liquid-fuel vaporization behavior transitioned from retreating to splitting to detaching after the end of injection was investigated with the model. Using an assumption of mixing-limited vaporization, liquid vaporization can be predicted with the model. The model reproduced the same trends (retreating, splitting, and detaching), with comparable spatial and temporal liquid fuel distributions [67,77]. The model results showed that the transitions were governed by the timescale of flow convection to the liquid length compared to the timescale of the injection rate ramp-down. For conditions where the flow timescale was relatively short (i.e., shorter liquid length, as in Fig. 4), the entrainment wave reaches the liquid length quickly, increasing entrainment and completely vaporizing the fuel downstream first, causing the liquid length to retreat back to the injector. For conditions with a relatively long flow timescale (i.e., longer liquid length, as in Fig. 5), the entrainment wave reaches the liquid length later, and therefore affects the upstream mixtures earlier, causing the upstream fuel to completely vaporize first so that the liquid spray detaches from the injector. Splitting of liquid after the end of injection like that shown in Fig. 6 is caused by rate-of-injection ramp-down shapes that also propagate an entrainment wave downstream but leave a low-mixing region near the injector.

The agreement between the model predictions and experimental observations of liquid-fuel vaporization suggests that, after injection has ended, fuel near the injector can experience greater mixing than mixtures farther downstream. As a result, the axial equivalence ratio distribution after the end of injection may rapidly invert from the quasi-steady jet behavior. As described in the

review of the conceptual model for conventional diesel combustion, the equivalence ratio in a quasi-steady jet varies inversely with the axial distance from the injector – the most fuel-rich mixtures are near the injector. In contrast, the one-dimensional model predicts that after the end of injection, the entrainment wave increases the mixing upstream so that mixtures near the injector quickly become more fuel-lean than downstream mixtures. The model predicts this inversion of the equivalence ratio profile for both retreating (Fig. 4) and detaching (Fig. 5) liquid fuel distributions; the ambient conditions and the injection ramp-down rate govern the local fuel evaporation rates.

Quantitative experimental measurements of vapor-fuel concentrations in the jet after the end of injection confirm the model predictions of fuel-lean mixtures quickly forming near the injector. One example is in Fig. 8, which shows ensemble-averaged equivalence ratio contours measured in the same heavy-duty engine as the data in Fig. 4, though with late- rather than early-injection PPCI [78]. The liquid-fuel behavior for late injection is the same, displaying a retreating liquid penetration-length as in the early injection of Fig. 4. The equivalence ratio contours were calculated from quantitative planar laser-induced fluorescence (PLIF) of toluene, which was introduced as a tracer for the fuel (n-heptane). In Fig. 8, the injector is on the left of each image, but it is rotated so that the fuel jet that was horizontal in Fig. 4 is instead directed downward and to the right. With the injector rotation, one of the other eight jets also enters the field of view, propagating upward and to the right.

Another example is in Fig. 9, which shows instantaneous (not ensemble-averaged) vapor-fuel density measurements by laser-induced fuel-tracer exciplex fluorescence in a constant volume chamber [79]. The single-hole injector is located at the top of the images of Fig. 9, and the jet penetrates downward. For the images prior to the end of injection, strong scattering/fluorescence from liquid fuel (top of image) is masked off. The fuel concentration data in Fig. 9 may be roughly converted to equivalence ratios for comparison with Fig. 8. If vaporization cooling and the volume occupied by the fuel vapor are neglected, then for injection into an ambient density of 25 kg/m^3 , the equivalence ratio calculated for an ambient oxygen concentration of 12.7% has approximately the same numerical value as the vapor fuel density in Fig. 9 (i.e., a vapor-fuel density of 1 kg/m^3 is approximately stoichiometric).

The 0° AEI images in both Figs. 8 and 9 show that when the measured injection rate decreases to zero at the end of injection, the vapor-fuel distribution in the jet is characteristic of a quasi-steady jet, with the most fuel-rich mixtures (highest equivalence ratios) near the injector. By only 1° AEI in Fig. 8, however, the peak equivalence ratio near the injector falls from 9 to only 3. By 3° AEI in Fig. 8, the mixtures near the injector are at most stoichiometric, and the mixtures downstream are more fuel-rich, which is the opposite of the axial equivalence ratio distribution for steady jets. By 5° AEI, mixtures near the injector are quite lean, with equivalence ratios on the jet centerline as low as 0.5.

This rapid leaning behavior after the end of injection is apparent not only in ensemble-averaged measurements, but in instantaneous images as well. Similar behavior is apparent in the single-shot images of Fig. 9, though the mixing to stoichiometric and fuel-lean mixtures near the injector occurs even more rapidly. The differences in the rate of leaning may be explained by differences in the injection ramp-down characteristics in the two experiments. The injection ramp-down period for Fig. 8 is approximately $300 \mu\text{s}$, while it is only approximately $100 \mu\text{s}$ for Fig. 9. For faster ramp-down rates, the entrainment wave described above increases near-injector entrainment more rapidly, leading to leaner mixtures more quickly [75]. Further

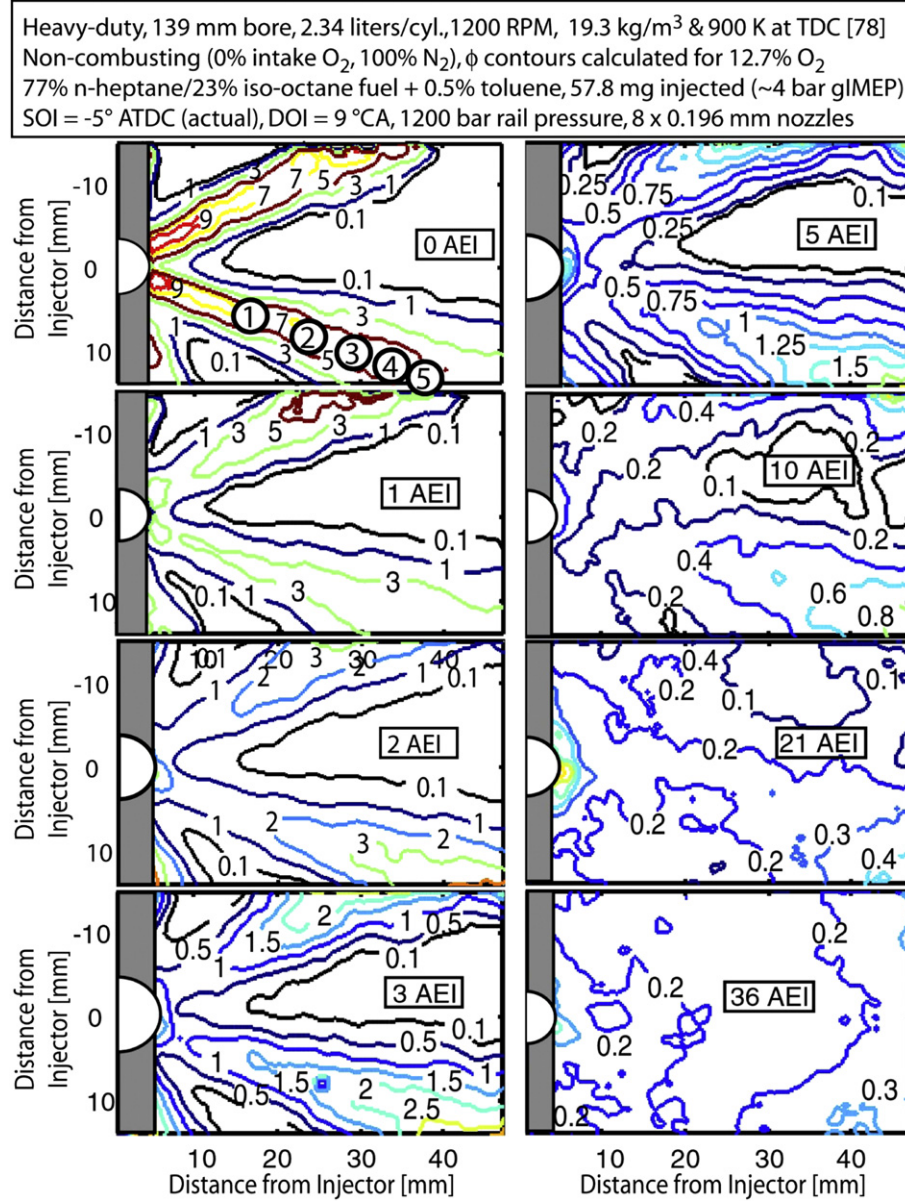


Fig. 8. Ensemble-averaged equivalence-ratio contours measured using toluene-PLIF [78]. The circled numbers in the top-left image show the time in crank-angle degrees for the jet to penetrate to the position of each circle.

dada from a Rayleigh-scattering measurements in a constant-volume combustion chamber under similar conditions as those for Fig. 8 (see the top of Fig. 15 for an example), also show lean mixtures near the injector after the end of injection [78], confirming the fuel tracer measurements.

Comparisons of equivalence ratio contours at similar downstream positions before and after the end of injection are consistent with an increased mixing rate after the end of injection. For example, in the upper-left image of Fig. 8, the circled numbers indicate the approximate time in crank angle degrees for fuel at the leading edge of the jet to reach each position during the initial jet penetration. From a Lagrangian perspective (i.e., moving with the flow), the equivalence ratio at each position gives a rough indication of the degree to which the fuel has mixed with the ambient gases at the corresponding time after leaving the nozzle. For instance, during the injection event, fluid that emanated from the injector will travel approximately 25 mm from the injector over a period of 2 crank angle degrees, to the position of the "2" circle,

where centerline equivalence ratios are between 5 and 7. After five crank angle degrees, the fluid will have moved about 45 mm to the "5" circle, where the centerline equivalence ratio is between 3 and 5. After the end of injection, the equivalence ratios at similar times and distances are much leaner, indicating more rapid mixing. At 2° AEI, centerline equivalence ratios 25 mm from the injector (corresponding to the "2" circle position in the 0° EOI image) are between 2 and 3, compared to 5 to 7 for the steady jet. At 5° AEI, centerline mixtures 45 mm from the injector (corresponding to the "5" circle position in the 0° EOI image) are near an equivalence ratio of 1.5, compared to 3 to 5 for the steady jet. Mixtures closer to the injector have even lower equivalence ratios, which indicate more rapid leaning near the injector after EOI. Hence, direct measurements of fuel vapor concentration show that mixing after EOI occurs faster than in the steady jet, which is consistent with the entrainment wave predictions of the one-dimensional jet model. Modeling predicts that the entrainment wave propagates more slowly at higher ambient densities, so that the increase in entrainment after

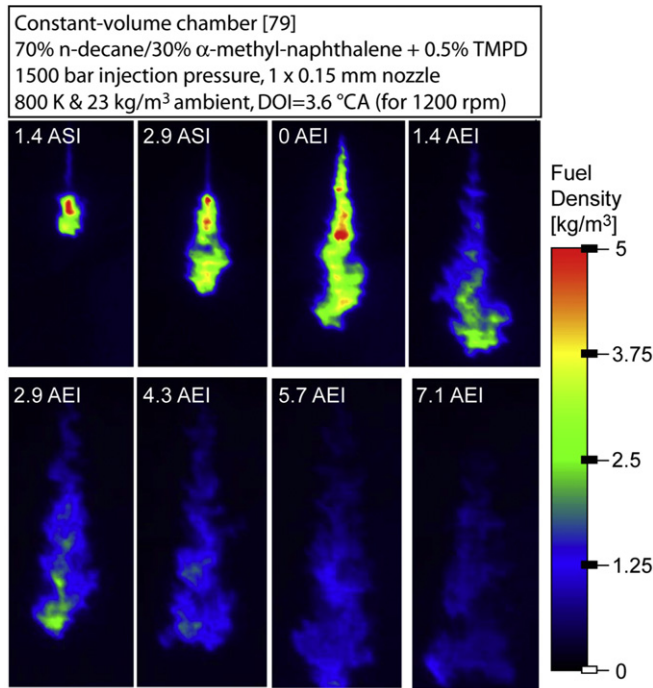


Fig. 9. Single-shot vapor-fuel density measured using laser-induced exciplex fluorescence in a constant-volume chamber [79]. For a 12.7% ambient oxygen concentration, the vapor fuel density in kg/m³ is also approximately equal to the equivalence ratio. Reprinted with permission, SAE paper 2005-01-2100 (c) 2005, SAE International.

the end of injection develops more slowly at higher density, scaling as $\rho^{-0.35}$, similar to the penetration rate. After the delayed passage of the entrainment wave, however, the simulation predicts that the entrainment-rate increase upstream of the head of the entrainment wave is slightly greater at higher ambient density (roughly 10% increase for doubling of ambient density).

In addition to increasing mixing rates after the end of injection, the entrainment wave may also act to limit excessive penetration of liquid fuel, which can be problematic under some LTC operating conditions. For the heavy-duty engine conditions of Fig. 4, the in-cylinder gases are hot and dense enough, and the cylinder geometry is large enough, that liquid fuel does not impinge on in-cylinder surfaces. With earlier injection into cooler, less dense in-cylinder gases or for smaller engines, however, the penetration can be large enough that liquid fuel can impinge on in-cylinder surfaces and form liquid films. One example has been shown previously in Fig. 6. A second example is depicted in Fig. 10, which shows a series of side-view images of Mie-scattered light from liquid-fuel sprays in a heavy-duty diesel engine, obtained under a low-load early-injection PPC condition [80]. In these images, the white ellipse (bottom) shows the bottom of the piston bowl, and the two curved white lines show the top of the far cylinder wall (top) and the top outer edge of the piston (middle). The injector has two rows of 103- μ m nozzles with a narrow included angle (70° for outer row), and injection starts near 40° before top-dead center (BTDC). For these conditions, the fuel spray impinges on the bottom of the piston bowl between 2.8° and 3.8° ASI, as indicated by a deflection of the spray by the bottom of the piston bowl. Due to the early injection-timing, the cylinder gases are relatively cool and have a low density, and long liquid-lengths are produced. Natural luminosity imaging shows that the liquid fuel films subsequently formed on the piston promote sooty combustion later in the cycle [80]. Many other studies report the formation of liquid fuel films under early-injection conditions [22,26,28,81–84].

Problems with excessive liquid-fuel penetration may be addressed to some degree by shortening the fuel-injection duration. For example, the images of liquid fuel presented in Fig. 5 were for a relatively short pilot-type injection, with a duration of only 360 μ s. Under the cool, low-density conditions of the test, the liquid fuel penetration was relatively long, reaching 65 mm from the injector. For the 140-mm bore (70-mm radius) heavy-duty optical engine used in Fig. 4, this penetration would approach, but not quite reach the cylinder wall. If the quasi-steady liquid length were established by using a longer injection, however, the liquid-length would have exceeded 80 mm, as shown by the vertical dashed line in Fig. 5. With such large penetration, liquid fuel would have impinged on the cylinder of even the large-bore engine used in Fig. 4.

The difference between the liquid-fuel penetration for the short and long injections can be explained by the action of the entrainment wave [85]. As described earlier, the momentum exchange between the jet fluid and the entrained ambient gases reduces the axial velocities in the jet. With greater entrainment after the end of injection, the slowing of the jet as it penetrates into the ambient is also greater than for a steady jet. As a result, when the entrainment wave reaches the head of the jet, the jet tip velocity, and hence the penetration rate, are reduced. Furthermore, due to increased entrainment of ambient gases and a reduced liquid fuel injection rate, the vaporization of the fuel is accelerated. The combination of decreased penetration rate and increased vaporization rate therefore decreases the maximum liquid fuel penetration for shorter injections. The one-dimensional jet model predicts that the entrainment wave penetrates at twice the initial jet penetration rate, so that it reaches the head of the jet approximately two injection durations after the start of injection. Indeed, penetration measurements show that the slope of the penetration curve changes abruptly at a time equal to two injection durations after SOI, further supporting the entrainment wave hypothesis [85,86].

The entrainment wave also affects vaporization of liquid fuel upstream of the tip of the liquid spray [67,85]. When the penetration is relatively short, such as in Fig. 4, the entrainment wave quickly reaches the tip of the liquid spray, where the liquid fuel is closer to the threshold of vaporization. The increased entrainment promotes vaporization, and the mixtures near the tip of the spray, which are closer to the threshold for vaporization, transition to full vaporization first. Thereafter, mixtures closer and closer to the injector cross the threshold for complete vaporization, causing the liquid retreat shown in Fig. 4. For conditions with longer liquid fuel penetration, such as in Fig. 5, the entrainment wave reaches the tip later. Hence, regions upstream of the liquid spray tip may cross the threshold for vaporization sooner than those at the tip, as in Fig. 5. In general, increasing ambient density causes the vaporization behavior after the end of injection to transition from initial upstream vaporization, as in Fig. 5, to liquid length recession, as in Fig. 4. Both liquid fuel penetration and the speed of the entrainment wave decrease with increasing density, but liquid fuel penetration decreases more strongly. Hence, the entrainment wave reaches the tip of the liquid fuel sooner, so that the liquid fuel tends toward greater recession at higher ambient densities.

Although liquid fuel vaporization and mixing after the end of injection were not the focus, several studies that provide vapor-phase fuel images show that the equivalence ratio rapidly decreases in the near-injector region after the end of injection, and that fuel vapor persists in this region; it is not completely convected away downstream [50,79,87]. Therefore, a mixture distribution stretching from fuel-lean near the injector to more fuel-rich downstream is expected to form after the end of injection in LTC engines, provided there is no serious modification by in-cylinder flow or wall-interaction effects. Since the LTC strategy requires

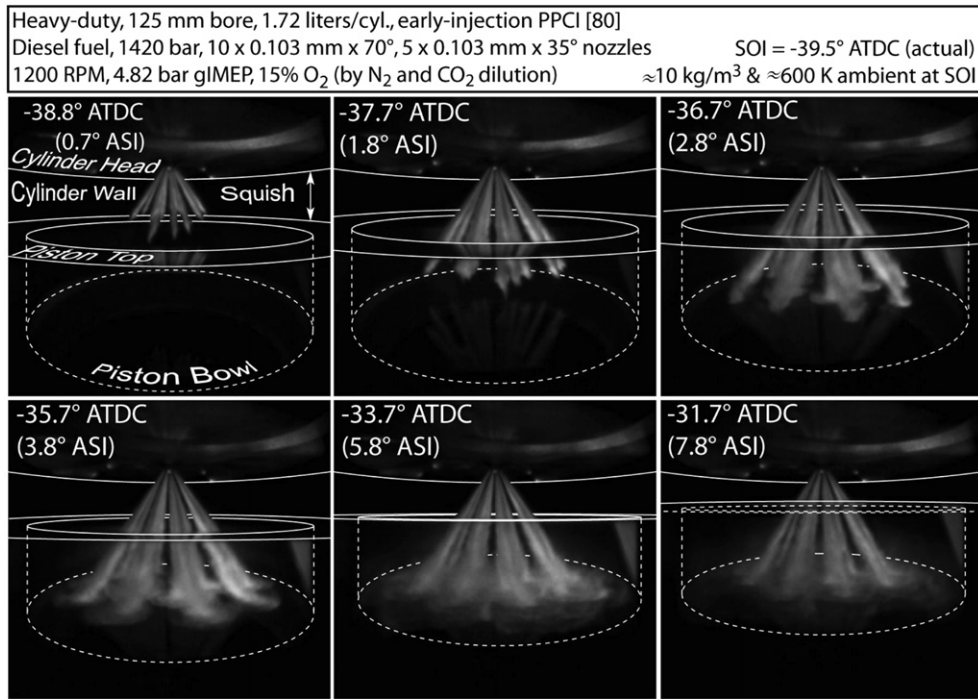


Fig. 10. Side-view images of liquid-fuel sprays from a narrow included-angle, dual-row injector for a low-load early-injection PPCI condition in a heavy-duty engine [80]. The white dashed ellipse (bottom) shows the bottom of the piston bowl, and the other curved white lines show the top of the far cylinder wall and the top of the piston.

a positive dwell between the end of injection and the start of combustion, this type of fuel-ambient mixing field is expected to exist when ignition and combustion commence.

Finally, although the experimental observations of liquid fuel vaporization and mixing after injection described above, as well as computer modeling [76,88], are consistent with the entrainment-wave hypothesis, as yet no definitive experimental velocity measurements are available to confirm the increased entrainment flows predicted by the models. Hence, the entrainment-wave explanation is as yet a hypotheses, and direct experimental measurements of entrainment velocities are needed to confirm its validity. Although some velocity data are available [86,89], the strong velocity gradients and high variability at the edge of the jet where entrainment may be quantified have precluded definitive evidence of entrainment-wave related flows. High-fidelity LES simulations that predict increased entrainment also explain why definitive measurements are elusive. The simulations predict that increases in entrainment flow velocities will be difficult to measure experimentally because relatively large velocity variations caused by large structures mask the changes in the underlying mean entrainment flow [76]. Indeed, significant averaging of the full three-dimensional LES velocity field and multiple realizations of the end-of-injection events were required to reveal the entrainment increase with any statistical significance. With point or even planar velocity measurements, a very large experimental dataset will likely be required to reveal the mean entrainment flow dynamics underlying the local velocity fluctuations at the jet periphery.

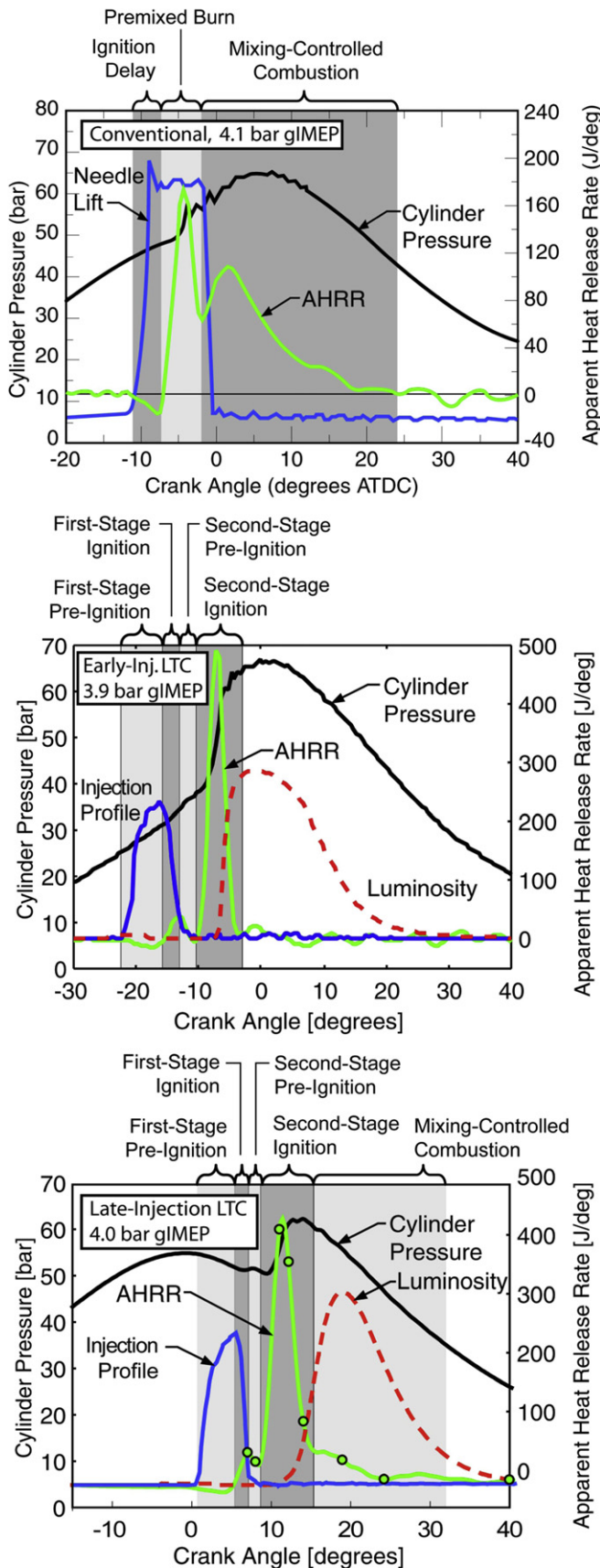
4. Two-stage ignition phenomena

The characteristics of ignition and heat release for LTC conditions are distinctly different from those for conventional diesel combustion. Because of greater dilution, greater premixing, and generally cooler in-cylinder gases, the initial ignition reactions for low-temperature combustion proceed at a slower rate than for

conventional diesel combustion. As a result, the individual ignition stages of typical diesel fuel become more distinct in heat-release-rate analysis.

For conventional diesel combustion, it is common to roughly divide the apparent heat release rate (AHRR) into three parts: ignition delay, premixed burn, and mixing-controlled combustion. The top plot of Fig. 11 shows cylinder pressure, AHRR, and needle-lift for the low-load (4.1 bar gIMEP) condition that was part of the basis for Dec's conceptual model of conventional diesel combustion [44]. Fuel injection begins near -11° after top-dead center (ATDC), when the in-cylinder gases are relatively hot (990 K) and dense (16 kg/m^3). As described in the background section, the liquid-fuel spray mixes with the ambient gases, which provide the thermal energy to vaporize the fuel. The vaporization of the fuel reduces the sensible thermal energy of the ambient gases, which decreases the cylinder pressure from what it would have been without vaporization. The vaporization is therefore manifest as a decrease in the AHRR during the ignition delay period. Ignition reactions proceed in the hot mixture of vaporized fuel and ambient gas. As they become more exothermic, the chemical rate of heat release eventually exceeds the vaporization energy rate (near -7.5° ATDC). This point, when the AHRR becomes positive, is a commonly used marker for the end of the ignition delay and the start of combustion.

During the premixed burn that follows, the ignition reactions rapidly accelerate, resulting in a peak AHRR near 180 J/degree as the available oxygen is consumed in the overall fuel-rich mixtures. The AHRR during the premixed burn is controlled primarily by chemical kinetics in the distribution of mixtures formed during the ignition delay and by the total mass of fuel which has been premixed. After the premixed burn, the AHRR typically decreases to a lower level, during which time combustion occurs in the standing premixed reaction zone shown in Fig. 2 and in the diffusion flame at the interface between the fuel-rich diesel jet and the surrounding ambient gases. The overall rate of combustion is then controlled not by chemical kinetics, but rather by mixing; that is, by the rate at



which rich mixture is delivered to the standing reaction zone and by the rate at which fuel and oxygen in the ambient gases are delivered to the diffusion flame. Shortly after the end of injection, combustion occurs solely within the diffusion flame.

For typical PPCI conditions, the AHRR shows additional features related to the chemical kinetics of diesel-fuel ignition that are not usually apparent in conventional diesel AHRR. The middle and bottom plots of Fig. 11 show examples of cylinder pressure, AHRR, and injection rate profiles for low-load EGR-diluted PPCI conditions with either early [64] or late [90] fuel injection. Both PPCI conditions are of similar loads to the conventional diesel condition, with gIMEPs of 3.9 bar (early injection) and 4.0 bar (late injection).

For the early-injection PPCI condition (middle plot in Fig. 11), fuel injection begins near -22° ATDC, when the in-cylinder gases are cooler ($\sim 770\text{ K}$) and less dense ($\sim 11\text{ kg/m}^3$) than for conventional diesel combustion conditions. After the start of injection, the AHRR for the LTC condition at first behaves similarly to that for conventional diesel combustion, with fuel vaporization causing a negative dip in the AHRR. Near -15° ATDC, the ignition reactions become exothermic enough to overcome fuel vaporization, and the AHRR becomes positive. This first stage of positive AHRR is relatively small and short-lived, peaking near -13° ATDC (9° after the start of injection). Near -11° ATDC, the AHRR falls back to near zero before rising rapidly in a second stage of ignition, to a peak near 500 J/deg at about -8° ATDC (14° after the start of injection). Note that the peak AHRR is nearly 3 times that for conventional diesel combustion, leading to significantly greater levels of combustion noise. Thereafter, the AHRR falls to nearly zero, with relatively minor mixing-controlled combustion heat release. The late-injection PPCI condition (bottom plot in Fig. 11) shows similar features, though with a somewhat lower peak AHRR and more significant mixing-controlled combustion. Consequently, for both early- and late-injection conditions, the LTC AHRR preceding the mixing-controlled portion may be roughly divided into four different parts (first-stage pre-ignition, first-stage ignition, second-stage pre-ignition, and second-stage ignition). Each part corresponds to a distinct phase of the chemical kinetics of ignition, as described in the following section.

4.1. Chemical kinetics of ignition

Typical diesel fuel is a mixture of thousands of chemical species, including single- and multiple-ring aromatics, olefins, and branched- and straight-chain alkanes [91]. The detailed chemical kinetics of ignition for such mixtures under diesel conditions is quite complex. Diesel fuel is normally composed of a large fraction of long, straight-chain alkane species, which are responsible for much of the two-stage ignition chemistry characteristic of diesel fuels. Indeed, the diesel fuel cetane number is defined according to the fraction of straight-chain hexadecane in the diesel primary reference fuel blend of hexadecane with heptamethylnonane. Considerable insight into the chemical kinetics of diesel fuel ignition may therefore be gained through analysis of a single straight-chain alkane surrogate.

Straight-chain (normal) n-heptane (C_7H_{16}) is a convenient surrogate for diesel fuel because its ignition delay and AHRR

Fig. 11. Fuel-injector needle-lift or injection profile, cylinder pressure, apparent heat release rate (and soot luminosity) for typical conventional diesel combustion [44] (top) reprinted with permission, SAE paper 970873 (c) 1997, SAE International), and two low-load EGR-diluted PPCI operating conditions with either early [64] (middle) or late [90] (bottom) injection. The circles along the apparent heat release rate in the bottom plot indicate timings of image acquisitions in Figs. 14, 17 and 19. The final, definitive version of Fig. 11 (middle) has been published in International Journal of Engine Research, 8(1), 2007 by SAGE Publications Inc., All rights reserved. © <http://jer.sagepub.com/content/8/1/97.full.pdf>.

behavior in engines are similar to that of diesel fuel, though its density and boiling point are significantly lower than for diesel fuel. Several chemical kinetic reaction mechanisms have been proposed for n-heptane for use in computer simulations of autoignition and combustion. The reaction schemes include skeletal mechanisms [92], which use reduced sets of characteristic reactions that represent whole families of elementary reactions, as well as more complex detailed kinetics, with all of the important elementary reactions included. The detailed mechanism, developed at Lawrence Livermore National Laboratory (LLNL) and at the Galway–Mayo Institute of Technology [93,94], is particularly well validated against available experimental data, and has been widely used to predict ignition. In addition to predicting ignition, analysis of the chemical species evolution provides insight into the chemical kinetics of ignition under various operating conditions.

Fig. 12 shows the results of a constant-pressure simulation of n-heptane ignition using the LLNL/Galway–Mayo reaction mechanism supplemented with the NO_x formation kinetics of GRI-mech 3.0 [95], at representative LTC conditions. The simulation was performed using the Senkin module of Chemkin [96], in a closed, homogeneous reactor—meaning that all of the mixing to a given equivalence ratio occurs before the start of the calculations, with no additional mixing after the start of reaction. In real diesel jets, of course, mixing and cylinder compression/expansion occur at the same time as chemical reactions, so that the fuel/air mixture fraction, temperature, and species composition evolve differently than in a constant-pressure closed reactor. Nevertheless, homogeneous reactor simulations provide important insight into the effect of premixing (equivalence ratio) on diesel fuel ignition processes under representative LTC conditions. The simulation was initialized with a stoichiometric mixture of vapor-phase n-heptane in an ambient gas containing 12.7% O₂ and the balance N₂, starting at a temperature of 787 K—the temperature achieved when fuel initially at a temperature of 363 K vaporizes and mixes adiabatically with the ambient gas at 840 K to a stoichiometric mixture. The pressure was held constant at 50 bar.

In Fig. 12, the slope of the temperature plot (red) roughly correlates with the AHRR, showing that ignition occurs in two stages. The

first, smaller rise in temperature near 0.9 ms (6.5° at 1200 rpm) corresponds to the small bump in the AHRR that occurs slightly later, at 9° ASI (near –13° ATDC) with diesel fuel in Fig. 11, middle. The earlier temperature rise predicted by the simulation relative to the engine experiment is consistent with a finite mixing time needed to prepare the mixture for combustion (the ‘physical’ component of the ignition delay period). Later, near 1.7 ms (12° at 1200 rpm), a second, larger temperature rise occurs which corresponds to the peak in the AHRR that occurs 14° after the start of injection in the engine with diesel fuel, near –8° ATDC in Fig. 11, middle.

Analysis of the evolution of several key species in the chemical kinetics simulation provides important insight into the two-stage ignition behavior of diesel fuels. Furthermore, the behavior of certain species like formaldehyde and OH, which are accessible by laser diagnostics, aids interpretation of laser-diagnostic data. The following paragraphs provide an overview of the evolution of key species throughout the two-stage ignition sequence, for which two different peroxide species are central to the first and second stages of ignition.

Analysis of the simulation results plotted in Fig. 12 reveals that, prior to the first stage of ignition, a sequence of pre-ignition reactions builds a pool of ketohydroperoxide (KHP) species, which is the central player in the first-stage ignition. The sequence begins with O₂ and later OH and hydroperoxy (HO₂) radicals abstracting a hydrogen atom from the parent fuel molecule. Thereafter, the resulting alkyl radical (R) reacts with O₂ to form a peroxy radical (RO₂). The RO₂ isomerizes, wherein a hydrogen atom shifts position to the O₂ end of the molecule. The isomerized peroxy radical then undergoes a second O₂ addition reaction, isomerizes again, and decomposes into a relatively stable ketohydroperoxide (KHP) having three oxygen atoms. The KHP species may further decompose, but below ≈800 K the production rate is greater than the decomposition rate, so that a pool of KHP builds [97].

Decomposition of the RO₂ and KHP molecules produces OH and other radicals that further attack the parent fuel molecules and accelerate the above steps. Various oxidation reactions involving radical species and hydrocarbon fragments build, raising the temperature. As the temperature approaches 850 K, chemical equilibrium for the reaction of R with O₂ shifts so that RO₂ formation is curtailed, slowing the reaction sequence that builds the KHP pool. Likewise, at these temperatures, equilibrium for the second O₂ addition reaction favors dissociation, further slowing the KHP buildup. The KHP continues to rapidly decompose, thus depleting the pool of KHP, as shown in Fig. 12. The KHP is the source for the radical species necessary for oxidation and heat release, and the heat release rate peaks at this time. When the KHP pool is finally exhausted, the heat release rate also decreases significantly, signaling the end of the first stage of ignition. It is this rapid depletion of the KHP pool that leads to the so-called “negative temperature coefficient” regime, wherein heat release rates slow despite increasing temperature.

In addition to increasing temperature, three important species are also formed during the first stage of ignition. First, oxygenated hydrocarbons that are products of KHP decomposition further decompose into formaldehyde (H₂CO). After its initial formation in the first stage of ignition, formaldehyde is gradually removed through oxidation by OH and other species. Importantly, the evolution of formaldehyde after the first stage of ignition (dashed red curve in Fig. 12) is remarkably similar to that of the total pool of all UHC species (blue curve in Fig. 12). As such, formaldehyde represents a marker for UHCs after the first stage of ignition, which is important because formaldehyde can be conveniently accessed by laser-induced fluorescence, as will be described later.

In addition to formaldehyde, a pool of hydrogen peroxide (H₂O₂) is also formed. H₂O₂ is important because it is the central player in

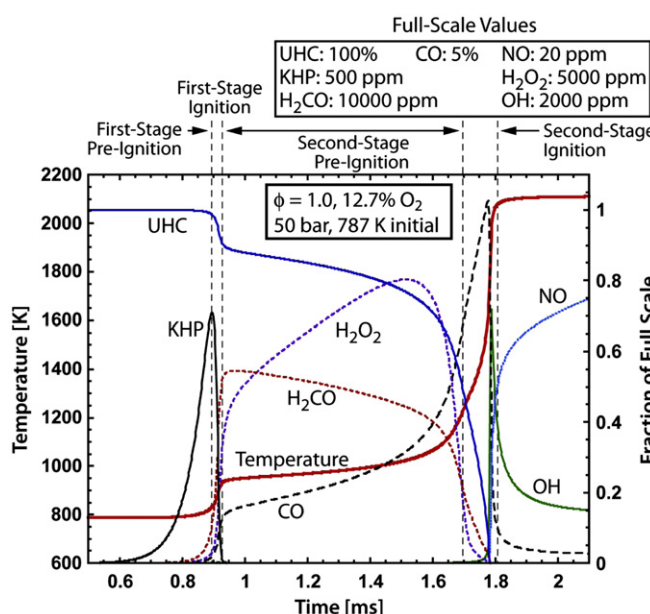


Fig. 12. Simulation of vapor-phase n-heptane ignition using the LLNL/Galway–Mayo mechanism [93] in a stoichiometric mixture of 12.7% O₂ and the balance N₂ at a constant pressure of 50 bar.

the second-stage of diesel fuel ignition. H_2O_2 is produced primarily by combination of hydroperoxy radicals (HO_2) that are formed during the first stage of ignition, but also by the reaction of formaldehyde with HO_2 to produce formyl radicals (HCO). After the first stage of ignition, oxidation of formaldehyde and other reactions continue to produce HO_2 radicals, which continue to build a relatively stable pool of H_2O_2 . At the same time it is being formed, some H_2O_2 decomposes into OH radical species, but until the temperature reaches 1000 K, the production reactions outweigh decomposition, and the H_2O_2 pool continues to build. As the available pool of OH and other species continues to oxidize unburned hydrocarbon species, the temperature gradually rises. During this period, the primary sink for OH is oxidation of formaldehyde.

As the temperature rises above 1000 K, H_2O_2 decomposition exceeds production, and the resulting pool of OH accelerates the overall rate of oxidation. The sudden release of OH radical species from decomposition of the H_2O_2 pool increases the overall oxidation rate, leading to the rapid temperature rise of the second stage of ignition, where most of the fuel chemical energy is released. The pool of H_2O_2 is a critical species affecting the onset of the second stage of ignition, with its decomposition into a pool of OH providing the radicals needed to yield runaway oxidation of the remaining hydrocarbon species.

A third important species, CO, is also produced during the first stage of ignition. Fig. 12 shows, however, that most of the CO is produced later, in the early part of the second stage of ignition. The primary sources of CO are the oxidation and decomposition of HCO that is formed through various routes, including reaction of formaldehyde with HO_2 . Late in the second stage of ignition, after the consumption of unburned hydrocarbons (see Fig. 12), the OH population increases rapidly to many times its level after H_2O_2 decomposition. At this time, the CO is rapidly oxidized as the temperature approaches its maximum. The appearance of this large OH population therefore marks the end of the second-stage ignition, when UHC and CO are consumed.

Note that these same reactions are present for conventional diesel combustion, but the higher ambient temperatures, richer ignition mixtures, and lower dilution levels accelerate the transitions between phases, so that the individual ignition stages are less distinct in the AHRR of conventional combustion.

To summarize, for stoichiometric EGR-diluted LTC, the n-heptane chemical kinetics simulations show that combustion occurs in four distinct steps, including two ignition stages, as illustrated in Fig. 12. During the first-stage pre-ignition reactions, oxidation of the fuel molecules builds a pool of KHP. Decomposition of the KHP builds a pool of radicals that oxidize hydrocarbon fragments from the fuel, raising the temperature in the course of the first stage of ignition. The first stage of ignition ends when the temperature rises sufficiently that the KHP pool is depleted. During the second-stage pre-ignition, pools of H_2O_2 and CO build as the formaldehyde formed during the first stage is gradually oxidized, along with other unburned hydrocarbons. When the temperature has increased sufficiently, the H_2O_2 decomposes, releasing a pool of OH radicals that initiate a high-temperature second-stage ignition, where most of the formaldehyde, CO, and UHC are consumed and where OH is formed in abundance.

For mixtures that are richer or leaner than stoichiometric, the general description of the ignition reactions is largely the same as for the stoichiometric condition described above, though the timing of events is different, and the fates of species such as CO and UHC after the second-stage ignition are much different. The most significant timing difference is the location of the second stage ignition, which is strongly affected by the mixture stoichiometry. To illustrate the effects of mixture stoichiometry on ignition processes, Fig. 13 shows two additional simulations made for conditions

similar to the stoichiometric mixture in Fig. 12, but with equivalence ratios of 0.7 (fuel-lean, top) and 2.0 (fuel-rich, bottom). Like Fig. 12, these simulations were carried out at a constant pressure of 50 bar; however, the initial temperatures differed to allow for the differing amount of energy required to vaporize and heat the fuel at each equivalence ratio (using the same unmixed temperatures of 840 K for the ambient gases and 363 K for the liquid fuel). Thus, after vaporization and adiabatic mixing, leaner mixtures will have a higher temperature than richer mixtures.

The building and destruction of the KHP pool, which is responsible for the first stage of ignition, is shifted earlier or later for (hotter) fuel-lean and (cooler) fuel-rich mixtures, respectively, relative to the stoichiometric condition in Fig. 12. Independent variations of temperature and equivalence ratio in the simulations indicate that the timing shift is primarily due to differences in mixture temperature. When temperature is constant, the timing of

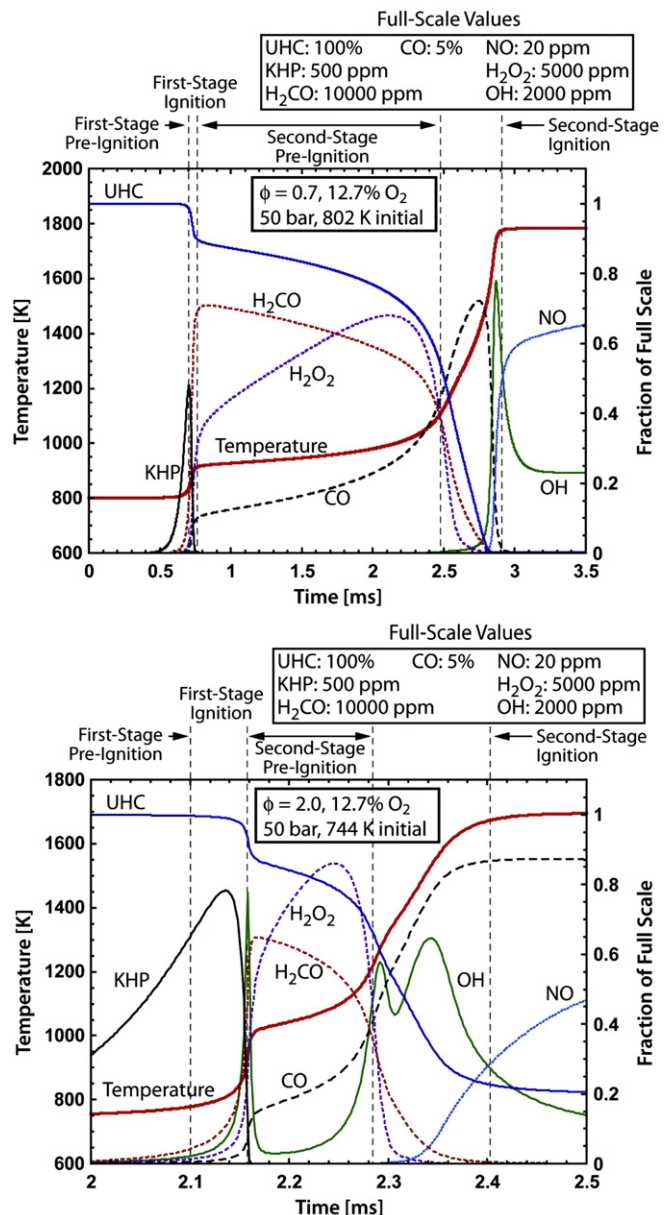


Fig. 13. Simulation of ignition of vapor-phase n-heptane using the LLNL/Galway–Mayo mechanism [93] for either fuel-lean (top) or fuel-rich (bottom) conditions in 12.7% O_2 and balance N_2 with a constant pressure of 50 bar.

the first stage of ignition is nearly constant, regardless of equivalence ratio [90]. The dwell between first- and second-stage ignition, however, is strongly affected by mixture stoichiometry, both at constant temperature and after considering equivalence-ratio dependencies upon initial temperature. Figs. 12 and 13 show that the depletion of the H₂O₂ pool during second-stage ignition occurs about 2.0, 0.8, and 0.2 ms after its formation for equivalence ratios of 0.7, 1.0, and 2.0, respectively. Clearly, rich mixtures achieve second-stage ignition much more quickly after first-stage ignition than lean mixtures. This is due, at least in part, to the increased temperature rise that occurs during the first stage of ignition. With $\phi = 2$, the temperature at the end of first stage ignition is nearly 1000 K, and is already approaching the temperature at which rapid H₂O₂ decomposition occurs.

The predicted influence of equivalence ratio on formaldehyde (H₂CO), which is a key species for laser diagnostics, is also important. Figs. 12 and 13 show that formaldehyde is formed at the first stage of ignition when the KHP pool decomposes, and persists until it is destroyed at the second stage of ignition. Formaldehyde exists during the dwell between the two stages of ignition, the length of which depends on mixture stoichiometry. Hence, the simulations indicate that differences in mixture stoichiometry can be deduced from the duration of the persistence of formaldehyde during the dwell between the first and second stages of ignition. These predictions have important implications for interpretation of optical diagnostic observations presented in the next section.

In addition to the difference in the timings of the two stages of ignition, mixture stoichiometry also strongly affects the concentrations of key species including OH, NO, and CO. For the stoichiometric mixture in Fig. 12, the peak OH concentration during second stage ignition (1200 ppm) is significantly higher than for either the fuel-lean (300 ppm) or fuel-rich (6 ppm) conditions. Indeed, simulations performed over a continuous range of equivalence ratios show that OH can provide an indication of the proximity of mixtures to the stoichiometric condition [98]. NO formation is rapid in zones of high OH concentration, and in magnitude mirrors the OH behavior, reaching the highest concentrations for the stoichiometric mixture. OH can thus provide an indirect and qualitative indication of likely NO distributions and regions of formation, which is useful due to the diagnostic difficulties associated with direct optical detection of NO.

Finally, the behavior of CO is similar for the fuel-lean and stoichiometric mixtures simulated here, reaching a similar peak prior to second-stage ignition. An important observation for interpretation of optical diagnostic images is that the CO reaches a peak near the boundary between the consumption of formaldehyde and the appearance of OH. For rich mixtures, the CO reaches a significantly higher level and will persist long after the second stage of ignition, if no additional mixing occurs. (The implications of mixing after combustion on CO and other species will be discussed in later sections).

4.2. Optical diagnostics of first-stage ignition

Based on the evolution of key species during ignition described in the previous section, optical diagnostics may be selected to probe diesel LTC ignition processes. Formaldehyde, in particular, is easily detected by optical diagnostics [47,50,99–103] and provides much insight into the spatial and temporal development of first-stage ignition.

Shown on the left in Fig. 14 are single-shot images of planar laser-induced fluorescence of formaldehyde (false-colored red) at two different crank-angles after the start of injection for a late-injection LTC condition in a heavy-duty engine [90]. The black-to-red colorbar at the bottom of each image gives a general

indication of the source of fluorescence. The colorbar is derived from the ensemble-averaged fluorescence emission spectrum acquired along the nominal jet axis. Red in the colorbar represents a strong signature of formaldehyde in the ensemble-averaged fluorescence spectrum at each downstream location. Black represents fluorescence interference that does not bear the spectral signature of formaldehyde, the most likely source of which is PAH fluorescence. Hence, regions in the image that are directly above more reddish parts of the colorbar are, on average, more likely from formaldehyde, while regions above darker parts of the colorbar are more likely from other species, like PAH. Because the colorbar is representative of the spectral content of the fluorescence signal, it does not correlate with the intensity of the fluorescence.

In Fig. 14, the strongly red colorbar for both images indicates that the fluorescence signal is almost entirely from formaldehyde. On the right are contours of equivalence ratio, measured under non-combusting conditions using planar laser-induced fluorescence of toluene fuel tracer [90]. All of the data in Fig. 14 were acquired from the same heavy-duty engine as those of Fig. 4, and the field of view is similar, with the injector on the left and the piston bowl-wall on the right. Unlike Fig. 4, however, the laser sheets for the images in Fig. 14 were aligned parallel to, and 7 mm below, the firedock. As a result of their parallel orientation, the sheets cross the jet axis at an angle of 14°. The images in Fig. 14 therefore do not show a cross-section along the jet axis, but rather a cross-section at a 14° angle to the jet axis. As a result, the region very near the injector does not intersect with the jets.

For this late-injection condition, Fig. 11 shows that first-stage ignition occurs near 6° ASI, coincident with the peak injection rate and slightly earlier relative to the start of injection than the early-injection condition in Fig. 11. Formaldehyde appears at 7° ASI (top-left image), near the peak of the first-stage AHRR (see circles in Fig. 11 that indicate image timings). The appearance of

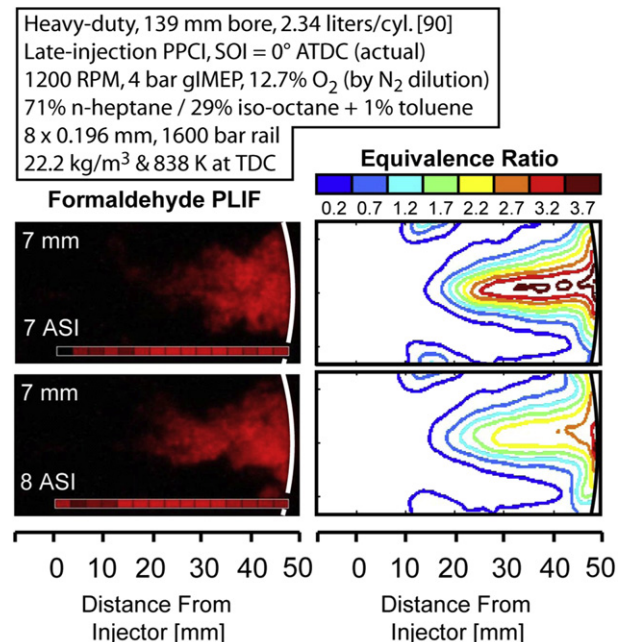


Fig. 14. Left: Single-shot images of formaldehyde PLIF for a late-injection PPCI condition in a heavy-duty engine with the laser sheets parallel to and 7 mm below the firedock (i.e., not along jet axis) [90]. The colorbar at the bottom of each image indicates the relative contribution of formaldehyde to the total fluorescence. Right: Ensemble-averaged equivalence ratio contours (calculated for 12.7% charge-gas oxygen) measured with toluene fuel-tracer PLIF under oxygen-free (non-combusting) conditions at the same thermodynamic state as the formaldehyde PLIF images [90].

formaldehyde is sudden – images acquired at 6° ASI (not shown) show no detectable fluorescence. Furthermore, the formaldehyde appears nearly simultaneously throughout most of the jet, with little change in the distribution from its first appearance at 7° ASI until the onset of second-stage ignition near 11° ASI. The ensemble-averaged equivalence ratio contour map (top-right image) shows that on average, mixtures in the jet range from fuel-lean conditions (equivalence ratios less than one) near the edges of the jet to fuel-rich conditions near the jet axis (equivalence ratios of nearly four). Other studies of diesel jets show similar rapid appearance of formaldehyde at the first stage of ignition [50,101,102,104]. Chemiluminescence emission from first-stage ignition reactions also appears over much of the jet at ignition [64,105], though unlike planar laser diagnostics, line-of sight considerations for chemiluminescence imaging preclude conclusions about the distribution within any specific cross section.

The apparent, simultaneous appearance of formaldehyde throughout a wide range of mixtures across the jet is inconsistent with single-zone simulations given in Figs. 12 and 13, which showed that formaldehyde should appear later in cooler, fuel-rich mixtures. The reason for this discrepancy between experimental observations and simulation predictions is not clear. However, the simple, closed, homogeneous reactor simulations do not capture all of the physical processes occurring in the engine. For example, the simulations neglect mixing between zones during ignition, as well as pressure and temperature variations that occur with compression and expansion. Mixing of radical species between adjacent zones of varying stoichiometry will certainly occur during stages of ignition, with radicals originating from lean zones mixing into rich zones, and vice versa. The transport of these radicals and thermal energy will alter the evolution of the ignition reactions from that of a closed reactor. Furthermore, the changes in pressure due to compression and combustion heat release may push rich mixtures to ignite sooner than they otherwise would at constant pressure. Indeed, multi-dimensional simulations that account for vaporization cooling, mixing, and pressure dynamics, albeit with a smaller (skeletal) reaction mechanism, predict a nearly simultaneous appearance of formaldehyde across a range of equivalence ratios [106]. In addition, closed-reactor chemical-kinetics simulations at the same initial temperature (i.e., without accounting for vaporization cooling as was done in Figs. 12 and 13) show that first-stage ignition does not depend upon equivalence ratio [90].

Although formaldehyde appears throughout the jet during first-stage ignition, the formaldehyde fluorescence intensity is stronger downstream, which suggests that the local formaldehyde concentration may increase with distance from the injector. Indeed, the formaldehyde concentration between the first and second stages of ignition is roughly proportional to the fuel concentration (see Fig. 13, for instance), so increasing formaldehyde concentration downstream is consistent with the increasing downstream equivalence ratios in Fig. 14 or in Fig. 8 near 5° AEI.

After its initial appearance, the formaldehyde distribution remains relatively unchanged until the second stage of ignition, even as the mixtures in the jet continue to lean out to lower equivalence ratios (e.g., mixture leaning from 7° to 8° ASI shown in equivalence ratio maps in Fig. 14). The single-shot formaldehyde images in Fig. 14 also illustrate that the formaldehyde distributions typically display a wavy structure along the outer contours (also see the images in [101,102]). Because of its nearly simultaneous appearance at first-stage ignition across a range of equivalence ratios, the structure of the formaldehyde distribution suggests a similar structure for the edge of the fuel jet. The equivalence ratio contours on the right side of Fig. 14 do not show this structure because they are ensemble averaged. Instantaneous images of fuel concentration, such as those from laser exciplex-fluorescence in

Fig. 9 however, do show significant structure after the end of injection. Another example is the upper portion of Fig. 15, which shows a single-shot equivalence ratio contour map along the diesel jet axis at 1.2 ms after the end of injection. In this case, the equivalence ratios were measured using a Rayleigh scattering technique in a constant-volume combustion chamber [78]. Below the equivalence-ratio map is a single-shot image of formaldehyde fluorescence [107], acquired at a similar time after the end of injection, in the same heavy-duty optical engine as in Fig. 14. Unlike the formaldehyde fluorescence images in Fig. 14, the image in Fig. 15 was acquired with the laser sheet oriented along the jet axis, so that it shows formaldehyde fluorescence signal much closer to the injector tip. Although the two images in Fig. 15 were acquired under slightly different ambient temperatures and densities, and from different facilities, they both illustrate significant structure along the jet boundaries after the end of injection. In the absence of combustion, the jet becomes still more variable, with an increasingly “wavy” outer edge. Schlieren movies also illustrate that after the end of injection, the outer boundary of the jet distorts and grows from the tight conical confines that are maintained during injection [108]. After the end of injection, these wavy structures lead, in an ensemble-averaged sense, to a growth in the average outer boundary of the jet. This growth is evident in the ensemble-averaged equivalence ratio contours of Fig. 8.

Finally, for the early-injection condition of Fig. 4, in which the downstream liquid fuel vaporizes prior to that of the liquid fuel near the injector, the first-stage of ignition occurs very near the end of injection. In addition to the mixing considerations described earlier, the temperature rise associated with the first-stage ignition heat release may also contribute to the more rapid downstream fuel vaporization for operating conditions where liquid still remains at first stage ignition [105]. However, experiments conducted under non-combusting conditions confirm that the downstream fuel vaporization after the end of injection occurs even without any ignition heat release [67,85].

In light-duty engines operating under LTC conditions, the fuel jets can strike the piston bowl walls even before the first stage of ignition, substantially altering their structure – as demonstrated by Fig. 6. High levels of flow swirl cause additional complications. Nevertheless, available images of fuel and H₂CO distributions in light-duty engines indicate that the basic physical picture deduced

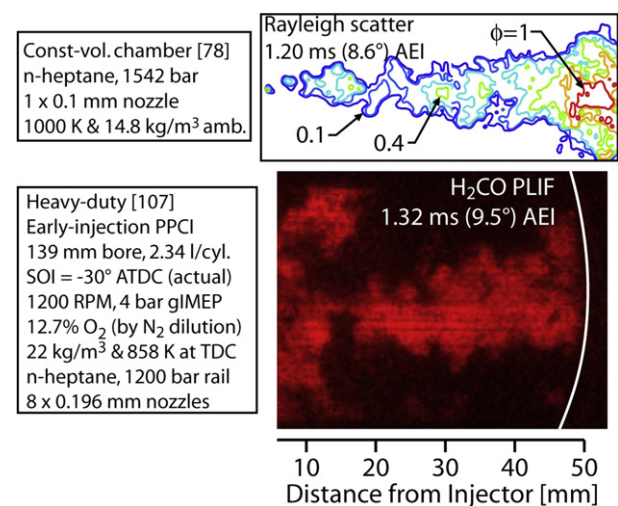


Fig. 15. Top: Single-shot vapor-fuel equivalence ratio contours along the jet axis at 8.6° after EOI obtained from Rayleigh scattered light [78]. Bottom: Single-shot H₂CO PLIF along the jet axis at a similar time after EOI [107].

for the mixture preparation and first stage of ignition in heavy duty engines is applicable, as described in the following paragraphs.

Fig. 16 shows mean equivalence ratio distributions [109] and a single-cycle H₂CO PLIF image [110] measured in the same light-duty engine at the same early-injection LTC operating conditions as the liquid-fuel distributions in Fig. 6. For the measurements shown in Fig. 16, however, the fuel is a mixture of iso-octane (25%) and n-heptane, which matches the ignition delay and subsequent heat release characteristics of the 2007 diesel certification fuel. Although the data were acquired after the end of injection, the schematic on the bottom-right of the figure illustrates the relationship of the laser sheet to the various fuel-jet axes; on the right-hand side of the image the laser sheet contains the jet axis, while on the left-hand side it bisects the angle between adjacent jets.

The first stage of ignition, which commences near -14° ATDC, is well underway at the time (denoted by the black dot in the heat release rate shown in the upper-left of Fig. 16) the equivalence ratio distributions and H₂CO PLIF images are acquired. At this time, the fuel jets have impinged on the bowl rim where they split and penetrate both into the squish volume and into the bowl. Notice that the flow swirl has transported much of the fuel out of the plane of the laser sheet in the jet-axis plane, and that the off-axis plane now contains significant amounts of fuel. The portion of the fuel jet deflected into the bowl follows the contours of the piston bowl periphery, such that the head of the jet is ultimately directed back towards the center of the cylinder. Like Fig. 14, however, fuel-rich mixture is found near the head of the jet, whether in the squish volume or in the bowl, while the region of the jet closest to the injector is fuel-lean. Neither swirl nor wall interactions have drastically changed the structure of the jet – they have just split and re-directed it.

Although images are not available with the same crank-angle resolution as in the heavy-duty engine, the available data indicate that the appearance of H₂CO is likewise quite rapid. At -15° ATDC only weak fluorescence is observed in the H₂CO PLIF images, and is due mainly to impurities in the fuel blend. By -12.5° ATDC, the

bottom-left portion of Fig. 16 shows that H₂CO is found throughout the split head of the jet, either in the squish region of the off-axis plane at the left of the cylinder or in the bottom right of the bowl in the jet-axis plane. (Note that the bottom left of the bowl is not illuminated well as the laser sheet enters from the right and is refracted by the optical piston pip.) Comparison of the mixture composition and H₂CO data shows that the H₂CO originates from mixtures spanning a broad range of equivalence ratios. In the upper central portion of the cylinder the H₂CO fluorescence intensity is low, as expected due to the low equivalence ratios measured in this region. Overall, the data indicate that the first stages of ignition develop in a very similar fashion in both heavy- and light-duty engines.

Other H₂CO LIF measurements in the literature show that the formation of formaldehyde occurs throughout the fuel jet cross section in PPCI operation with positive ignition dwell [101–103], similar to the results shown above. However, the identification of the equivalence ratios at the transition to first-stage ignition is less certain in other studies of light-duty, LTC operation in the literature, primarily because of the lack of quantitative measurements of the mixture distribution.

4.3. Optical diagnostics of second-stage ignition

The chemical kinetics discussion of Section 4.1 and Figs. 12 and 13 show that for fuel-lean to fuel-rich mixtures, formaldehyde is consumed during second-stage ignition. Furthermore, for fuel-lean to stoichiometric mixtures, significant concentrations of OH appear at second-stage ignition. The behavior of these two optically detectable species, therefore, provides much information about the spatial and temporal evolution of second-stage ignition. Optical detection of PAH further provides complementary information on the locations of partially-oxidized, fuel-rich mixtures.

Fig. 17 shows a series of simultaneous single-shot images of planar laser-induced fluorescence of formaldehyde, PAH, and OH

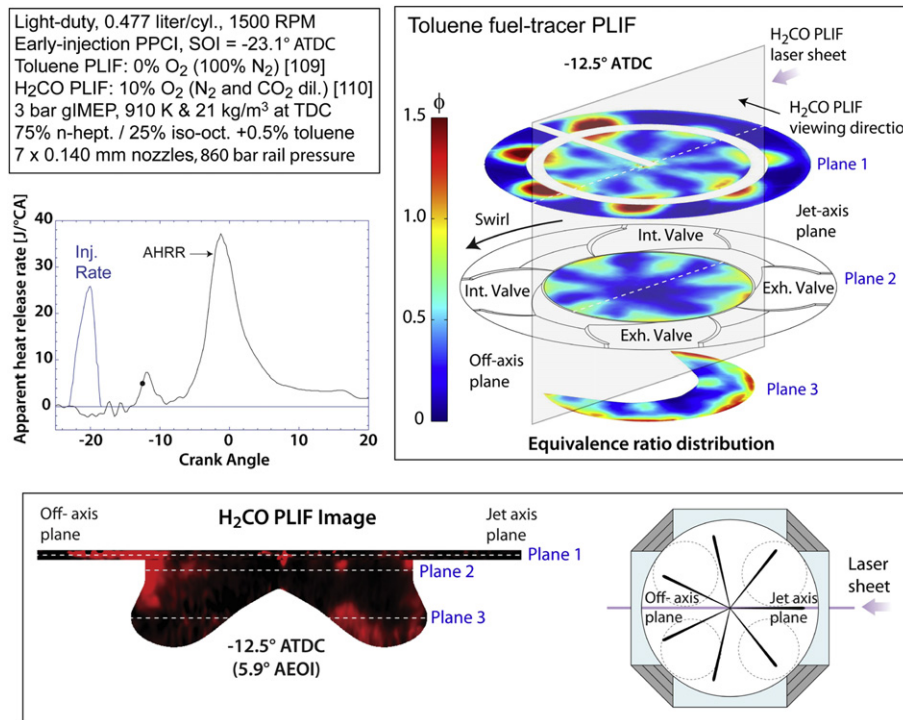


Fig. 16. Light-duty early-injection PPCI. Upper-left: injection rate and apparent heat release rate. Upper-right: mean equivalence ratio distribution measured with toluene-PLIF approximately mid-way through the first stage of ignition [109] reprinted with permission, SAE paper 2012-01-0692 (c) 2012, SAE International. The measurements were performed under oxygen-free (non-combusting) conditions as in Fig. 14. Bottom: single-cycle H₂CO PLIF image (unpublished, but taken from full dataset of [110]).

for a late-injection LTC condition in the heavy-duty diesel engine [90]. Like Fig. 14, the images are acquired in horizontal planes at different elevations below the cylinder head, which are indicated in the upper-left corner of each image. The images span the period from the first appearance of OH, near the peak in the AHRR (see circles along AHRR curve Fig. 11, bottom), until late in the cycle, when most of the heat release is complete. In each image, OH is false-colored green, and combined formaldehyde and PAH fluorescence is false-colored red. As in Fig. 14, the colorbar at the bottom of each image indicates the strength of the formaldehyde signature in the spectrum of the combined fluorescence along the jet axis. Red regions of the image with red in the colorbar below indicate significant formaldehyde fluorescence. Conversely, red regions in the images with black in the colorbar below indicate fluorescence from other sources, most likely PAH.

OH fluorescence (green) first appears near 11° ASI (11° ATDC), which is about midway through the second-stage ignition heat release, near the peak AHRR (see circles along AHRR curve Fig. 11, bottom). The timing of the OH appearance is consistent with the chemical kinetics of fuel-lean and near-stoichiometric mixtures (Figs. 12 and 13), which show that significant OH first accumulates when the temperature is near midway through the rapid rise during second-stage ignition. Also, spatial overlap between OH (green) and formaldehyde fluorescence (red), which appears as yellow in the Fig. 17 images, is minimal. The lack of spatial overlap between OH and formaldehyde fluorescence is consistent with expectations derived from the chemical kinetics of ignition. That is, Figs. 12 and 13 show that for fuel-lean and near-stoichiometric mixtures where significant OH is formed, the formaldehyde is consumed before significant OH appears.

The OH generally appears downstream in the jet, closer to the piston bowl wall on the right side of the images. Other studies have also reported a similar downstream appearance of OH for comparable operating conditions [101,102]. Recall that Figs. 12 and 13 show that OH concentrations in rich mixtures (less than ten ppm) is much lower than for mixtures of fuel-lean or intermediate, near-stoichiometric mixtures (hundreds or thousands of ppm). The appearance of significant OH downstream therefore suggests that those mixtures are of intermediate stoichiometry, between

approximately $\phi = 0.5$ and $\phi = 1.2$ [98]. Indeed, the equivalence ratio measurements at 12° ASI (right-center column of Fig. 17) show that on average, mixtures are of intermediate stoichiometry in the regions where OH is generally detected, though the correspondence is not perfect (some average rich regions show OH in instantaneous images). As with Fig. 14, the fluorescence images are single-shot, while the equivalence ratio maps are ensemble-averaged, so the two measurements will not correspond exactly. However, on average, the OH first appears downstream in the jet, in regions of intermediate stoichiometry. Chemiluminescence images (not included here) also show that after weak first-stage chemiluminescence emission, stronger second-stage chemiluminescence first appears nearly simultaneously with OH and in similar downstream locations as OH [64,105].

In addition to the distinct separation of first- and second-stage ignition processes and the associated timing of formaldehyde and OH appearance for LTC compared to conventional diesel combustion, the spatial distribution of OH is also broader. As described in Fig. 2 and the related discussion, OH initially appears on the periphery of the jet in conventional diesel combustion, and it generally remains on the periphery in a thin diffusion flame throughout the quasi-steady period [44,111]. Fig. 17 shows that for these LTC conditions, OH first appears downstream and quickly fills much of the jet cross-section. Although some thin structures are discernable in a few of the earlier images at 11° and 12° ASI, the spatial distribution in most of the jet is quite broad, with large pockets of relatively uniform OH fluorescence. Within a few crank angle degrees, by 14° ASI, the thin structures have largely disappeared, and the OH fluorescence is distributed in relatively uniform pockets. In other studies with similar, positive ignition dwells, including early-injection PPCI conditions, the OH behavior is similar, with broad distributions across the jet width [101,102,105,112].

While the images in Fig. 17 show no significant overlap between formaldehyde and OH, consistent with the replacement of formaldehyde by OH at second-stage ignition (Figs. 12 and 13), OH does not appear everywhere in the jet where formaldehyde is absent. For example, in Fig. 17, when OH first appears within the fuel jet, some of the fluorescence images show dark interior regions where

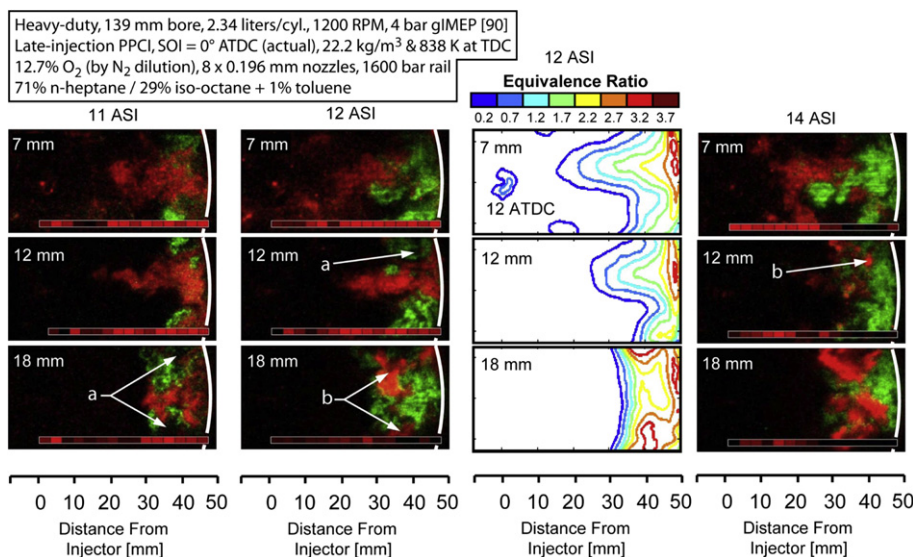


Fig. 17. Combined single-shot formaldehyde PLIF and PAH PLIF/Soot LII (red) and OH PLIF (green) for a late-injection LTC condition in a heavy-duty engine [90]. Red in the colorbar indicates a strong signature of formaldehyde in the fluorescence spectrum. The third column shows ensemble-averaged equivalence ratio contours (calculated for 12.7% charge-gas oxygen) measured with toluene fuel-tracer PLIF under oxygen-free (non-combusting) conditions at the same thermodynamic state as the formaldehyde PLIF images. (For interpretation of the references to color in this figure legend, the reader is referred to the web version of this article.)

neither formaldehyde nor OH is detected, labeled “a” in the figure. Soon after these initial voids are observed, later images show significant broadband PAH fluorescence (colored bright red in the image, with black in the colorbar below) in similar regions, as indicated by the “b” labels. The images from successive crank angles are not acquired sequentially, from within a single engine cycle. Consequently, due to cycle-to-cycle variation, the early dark voids do not correspond exactly to the later PAH fluorescence regions. However, the typical behavior shows that the regions that frequently develop voids in formaldehyde fluorescence that are not filled by OH fluorescence later show PAH fluorescence.

The equivalence ratio contours in Fig. 17 show that the regions where PAH fluorescence appears are typically fuel-rich. In particular, the bottom row of images in Fig. 17, which corresponds to a plane low in the piston bowl, shows voids in OH and formaldehyde fluorescence at 11° ASI, with PAH appearing at 12° ASI, and equivalence ratios that are fuel-rich (greater than one) on average. By 14° ASI, the PAH regions have grown much larger. The PAH species are precursors for soot, so soot likely forms in the same regions. Indeed, in addition to PAH fluorescence, some of the broadband signal is likely due to laser-induced incandescence of soot. Laser-induced incandescence and natural luminosity imaging (not shown here) confirm that soot distributions are similar to the PAH distributions of Fig. 17, with soot appearing in the downstream part of the jet, near the piston bowl-wall [105].

The location of soot formation near the head of the jet is somewhat dependent on the operating condition. For the condition selected for the images in Fig. 17, the injection timing and duration were adjusted to the threshold of sooting. That is, with either a later injection or a shorter injection duration, very little or no soot would have formed. The soot formation behavior illustrated in Fig. 17 therefore corresponds to “threshold-sooting” LTC conditions. A more detailed study of fuel jets over a range of conditions showed that LTC conditions providing a shorter or negative ignition dwell result in soot forming farther upstream in the jet, closer to the injector [113]. A parametric sweep of ignition dwell, achieved by decreasing the intake temperature, showed soot forming farther downstream with increasing ignition dwell. With the longest ignition dwell, soot only formed at the piston bowl-wall, near the head of the jet [113]. Other studies that don't necessarily have positive ignition dwell, but that increase ignition delay by decreasing the charge O₂ concentration (increasing EGR rate) reach similar conclusions [114,115]. With lower charge O₂ concentration, soot forms further downstream, and the delay time between second-stage ignition and the first measureable soot formation increases [114,115].

Under the threshold-sooting conditions of Fig. 17, the fuel-rich regions that go on to form PAH and soot are on either side of the jet axis, where the jet merges and interacts with neighboring jets after impinging on and spreading along the piston bowl-wall. The interaction between neighboring jets contributes to the creation of fuel-rich pockets near the piston-bowl wall. However, even in jets that have no significant interaction with other jets, soot still forms near the head of the jet under threshold-sooting LTC conditions [105,115]. Fundamental studies of jet mixing processes confirm that the head vortex region can be significantly more fuel-rich than the quasi-steady region that follows [116], which would therefore imply greater soot formation at the head. The interaction between neighboring jets likely inhibits mixing even further, further promoting rich mixtures near the head of the jet.

While soot and its precursors are relatively straightforward to probe with laser diagnostics, in-cylinder NO is much less accessible. Previous successful demonstrations of in-cylinder NO PLIF in the same heavy-duty optical engine were for conventional high-temperature diesel combustion, with very high engine-out NO_x [117]. Even then, signals were quite weak, near the detection

threshold. For low-NO_x LTC conditions, direct imaging of NO has not been demonstrated, and may not be possible with current laser-induced fluorescence detection techniques. However, chemical kinetics considerations show that, for mixtures of intermediate stoichiometry, the rapid increase in temperature that occurs during 2nd-stage ignition is associated with high OH concentrations, which remain elevated in the high-temperature post-combustion gases. These same high temperature regions form significant NO. Indeed, Figs. 12 and 13 show that the period of rapid NO formation is concurrent with peak OH concentration, and post-ignition NO concentrations correlate well with post-ignition OH concentration – mixtures of intermediate stoichiometry have both the highest OH and NO concentrations after second-stage ignition. The OH distributions in Fig. 17, therefore, should approximately represent NO distributions. Accordingly, much like the earlier observations regarding OH, the likely initial NO distributions for PPCI LTC conditions are significantly different than for conventional diesel combustion. Instead of initial NO formation near the thin, high-temperature diffusion flame as illustrated in Fig. 2, NO should initially form throughout the jet cross section, in the regions where OH is detected and where the equivalence ratio contour maps show that the mixtures are of intermediate stoichiometry. Note that after the initial formation of NO in conventional diesel combustion, later-cycle imaging shows broad distributions of NO [117].

Simultaneous measurements of H₂CO and OH in light-duty engines are limited, but the available data [101] are consistent with the picture described above based on the simulations of chemical kinetics and the measurements in heavy-duty engines. Formaldehyde is formed beginning at the onset of first-stage ignition, and is first visible in the upstream regions of the jet where leaner mixtures are expected. A few crank angle degrees later, formaldehyde fills the jet cross section, including the richer regions near the head of the jet. OH is first observed near the peak heat release portion of the second-stage ignition process, and, as in Fig. 17, is largely found near the head of the jet. Likewise, little overlap is observed between H₂CO and OH. This work was performed in an engine with a flat piston-top, however, and the similarity of the results to those obtained in heavy-duty engines should not be surprising, since the interaction between the fuel jets and the combustion chamber surfaces is not dissimilar.

For light-duty engines with a bowl-in-piston geometry, simultaneous H₂CO/PAH and OH measurements similar to those shown in Fig. 17 are not available, but existing images of combined H₂CO/PAH fluorescence excited with 355 nm laser light illustrate aspects of the second-stage ignition process that closely parallel the behavior observed in heavy-duty engines. Example images obtained in a late-injection LTC operating condition are shown in Fig. 18. This operating condition is comparable to the late-injection condition examined in Fig. 17, and is characterized by an O₂ concentration of 15% and SOI = 1.25° ATDC. However, the fuel employed is a commercial #2 diesel fuel. Additional details can be found in [118]. The emissions measured at this operating condition are exhibited in the upper-right portion of Fig. 1, at the latest injection timing shown. Recall that in light-duty engines, the fuel jets impinge on the bowl lip region and are split into portions which penetrate into either the squish region or down further into the bowl. In comparison to the early-injection LTC condition examined in Fig. 16, relatively little fuel enters the squish volume with near-TDC injection timing, and the bulk of the fuel is deflected into the bowl. Consequently, richer mixtures are expected within the bowl region with late injection timing.

Inspection of the cycle-averaged PLIF images in Fig. 18 shows that as the heat release transitions from low-temperature heat release to high temperature heat release, the observed H₂CO/PAH fluorescence also transitions through a local minimum in intensity.

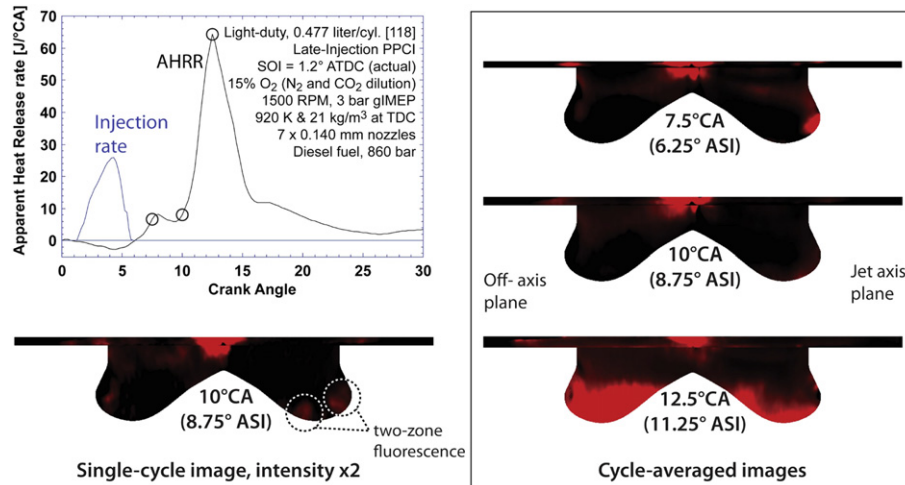


Fig. 18. Formaldehyde and PAH PLIF observed in a light-duty engine with late-injection PPCI operation (unpublished images from dataset of Ref. [118]). The images shown were acquired at equal camera gains and the cycle-averaged images are displayed with equal intensity scales. The intensity of the single-cycle image has been enhanced to emphasize the two-zone nature of the fluorescence from the bowl in the jet axis plane.

At 7.5°, bright fluorescence is observed from mixture near the head of the jet, in the re-entrant portion of the bowl. This fluorescence is expected to be dominated by H₂CO emissions from rich mixture in the head of the jet, as is anticipated from the equivalence ratio distributions in Figs. 16 and 17. As combustion progresses through the local minimum in heat release to the start of high-temperature heat release near 10°, the observed fluorescence dims. This corresponds closely with the timing of the first appearance of OH fluorescence in the images of Fig. 17, at which time Figs. 12 and 13 show that H₂CO is largely consumed. The fluorescence intensity subsequently increases again at 12.5°, and continues to increase for several crank-angle degrees thereafter. This second increase, first observed at the time of peak heat release, corresponds closely to the timing of the appearance of PAH fluorescence in Fig. 17.

Single-cycle PLIF images obtained at this time very often exhibit a two-zone distribution of fluorescence within the bowl in the jet axis plane; an example is shown in the lower left portion of Fig. 18. This two-zone distribution persists into the high temperature heat release period, as can be inferred from the bi-modal intensity distribution that is still suggested by the cycle-averaged image shown for 12.5°. Although the mixture formation and ignition processes leading to this two-zone distribution remain unclear, similar two-zone distributions are seen under early-injection conditions. In Ref. [119] it was hypothesized that the outer zone corresponded to fuel-lean mixture. However, more recent, direct measurements of the equivalence ratio distributions indicate that the mixture is likely fuel rich in both zones [109]. Overall, despite the differences between light-duty and heavy-duty engines in the spatial structures of the fuel jets due to interactions with the ambient flow and the combustion chamber walls, the progression of the ignition process is remarkably similar.

5. Late-cycle processes

5.1. Soot oxidation

The initial pockets of PAH and soot that form in rich regions near the piston bowl-wall in heavy-duty engines at first grow larger, but later in the cycle they are largely oxidized. Fig. 19 shows late-cycle single-shot images of combined formaldehyde and PAH fluorescence and soot incandescence with simultaneous OH fluorescence obtained in a heavy-duty engine [90], extending the late-injection

LTC sequence shown in Fig. 17. The circles along the AHRR curve in the bottom plot of Fig. 11 show the timing of the image acquisitions. The late-injection LTC plot in the bottom of Fig. 11 also shows that the combustion luminosity, which is mostly due to soot, peaks near 19° ASI, and then gradually decreases to near-zero at 40° ASI. The combined formaldehyde and PAH PLIF/soot LII images are consistent with the combustion luminosity, showing an increase in the size of the PAH/soot distributions in the lower plane at 19° ASI, as well as an appearance of PAH/soot in the middle and upper planes. Later in the cycle, the extent of the PAH/soot pockets decrease. Meanwhile, the OH distribution remains broad, filling much of the downstream jet cross section and generally surrounding the PAH/soot pockets. Similar soot pockets surrounded by OH have been observed for conventional diesel combustion, though much later in the cycle [120]. Although the PAH fluorescence images are not quantitative, the decrease in both the spatial extent and intensity of the PAH/soot, as well as the decrease in combustion luminosity in Fig. 11, indicate likely soot oxidation. Indeed, more quantitative 2-color soot thermometry measurements under similar conditions show significant soot oxidation late in the cycle [15,113]. The rate of soot oxidation depends on the combustion temperatures, which are affected by EGR [15,114,121,122].

Similar behavior is also observed in light-duty engines. The bright PAH PLIF/soot LII deep in the bowl at 15° ATDC (Fig. 18) is observed well into the expansion stroke, though its typical intensity and area are diminished considerably as the cycle progresses. The plume of burned combustion products in which PAH and soot are embedded also gradually rises out of the bowl into the clearance volume. Examples are shown in Fig. 20. Engine-out emissions are consistent with the in-cylinder oxidation of soot evidenced by the infrequent observation of soot at the latter crank angle (50° ATDC). Engine-out filter smoke numbers measured at this operating condition are very low, as seen in Fig. 1.

Although the engine geometries are different, the sequence of soot formation and oxidation bear strong similarities in other heavy-duty [114] and light-duty [121] engines operating in LTC mode. Soot formation occurs as fuel jets spread across the back wall, and pockets of soot linger at the location of neighboring jet-jet interaction [114,121]. While EGR dilution reduces the soot formed in-cylinder via premixed LTC, soot oxidation is slower because of the lack of ambient oxygen and low combustion temperature [114,121,122].

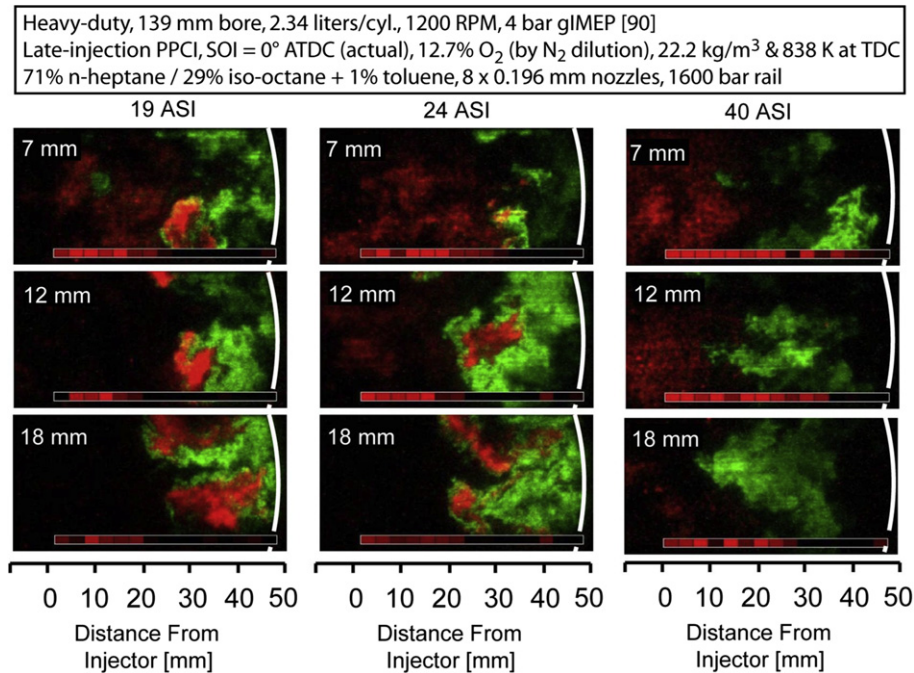


Fig. 19. Late-cycle single-shot combined formaldehyde and PAH PLIF/Soot LII (red) and OH PLIF (green) at a late-injection PPCI condition in a heavy-duty engine, continuing from Fig. 17 [90]. (For interpretation of the references to color in this figure legend, the reader is referred to the web version of this article.)

5.2. Late-injection PPCI UHC and CO emission sources

In contrast to the downstream mixtures shown in Fig. 19, which exhibit broad regions of OH indicative of mixtures that have attained second-stage ignition, the upstream mixtures show evidence that the second stage of ignition is not achieved.

Throughout the entire combustion event in the upper (7-mm) plane of Figs. 17 and 19, significant formaldehyde remains on the left side of the images – a region which is upstream in the jet, close to the injector. Later, as the piston moves downward, formaldehyde appears in the other planes, first in the 12-mm plane at 24° ASI and then in the 18-mm plane at 40° ASI. The formaldehyde also

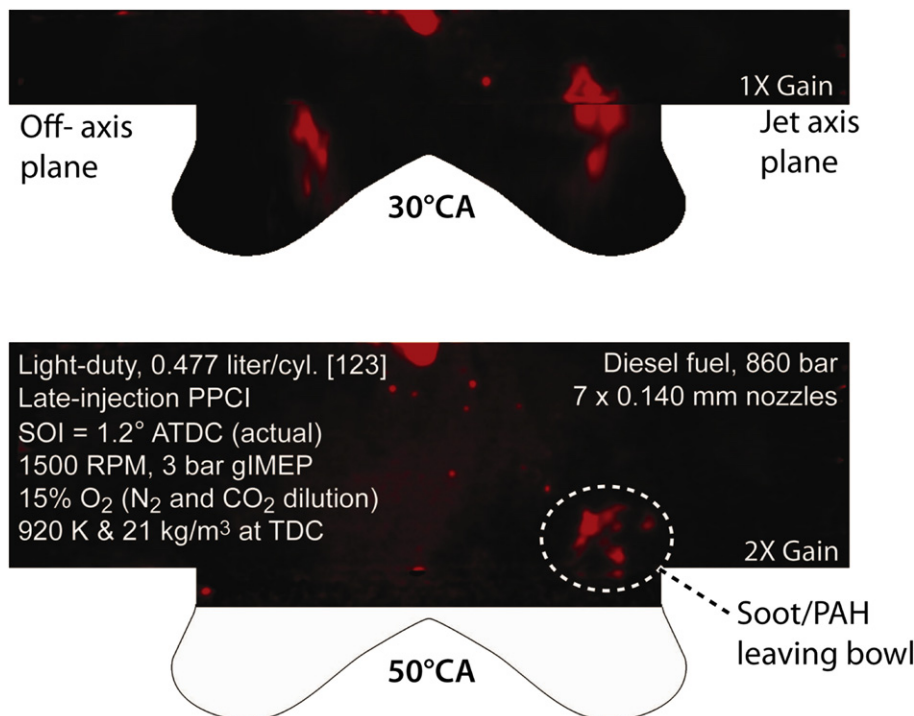


Fig. 20. Images of PAH PLIF/soot LII for a late-injection LTC operating condition in a light-duty engine (unpublished, from dataset of Ref. [123]). The image shown at 50° ATDC is not characteristic, as soot/PAH leaving the bowl is only infrequently observed.

becomes much more broadly distributed, without any clear indication of the initial conical-jet shape that was evident in the earlier images in Figs. 14 and 17.

Other studies show a similar progression of OH and formaldehyde from two-stage ignition though the late cycle, with near-injector formaldehyde remaining late in combustion [101,102,112]. Fig. 21 shows an example sequence for a late-injection light-duty engine [101]. The first row of images shows the appearance of formaldehyde (red) from first stage ignition (see AHRR plot, top), similar to Fig. 14. The second row shows the appearance of OH (green) downstream after the second-stage ignition, similar to Fig. 17. Finally, the third row shows the persistence of formaldehyde late in the cycle, especially near the injector, similar to Fig. 19.

According to the chemical kinetics considerations described earlier, the long persistence of formaldehyde is indicative of incomplete combustion and associated unburned hydrocarbons (UHC) and CO. Furthermore, the likely cause is overmixing to conditions that are too fuel-lean to achieve second-stage ignition in the time available before volume expansion cools the mixture during the power stroke. Indeed, direct mixing measurements under non-combusting conditions in Fig. 8 confirm that mixtures near the injector continue to become both more fuel-lean and more broadly distributed late in the cycle.

Once again, similar behavior is observed in light-duty engines. In Fig. 21, formaldehyde persists within the central region of the cylinder until at least 40° ATDC. Likewise, in the image obtained at 50° ATDC presented in Fig. 20, the central region of the cylinder is filled with low-intensity, diffuse fluorescence similar to the fluorescence observed in the upper planes at 40° ASI in Fig. 19 or in Fig. 21. The spectral characteristics of this fluorescence (albeit measured at a lower O₂ concentration and more advanced timing [124] than for the conditions in Fig. 19) indicate the presence of formaldehyde, again pointing to the incomplete combustion of overly lean mixtures. This diffuse, near-injector fluorescence is first observed much earlier in the cycle than in Fig. 19, less than 2° after the end of injection. Embedded in this diffuse mixture are spherical fuel droplets, which represent a separate source of UHC emissions that will be discussed in greater detail below.

Just as the impact of equivalence ratio on ignition kinetics was examined in Figs. 12 and 13, the coupling of the ignition kinetics with the charge temperature variation due to compression and expansion can be examined more closely with homogeneous reactor simulations. Fig. 22 shows the results of these simulations for an equivalence ratio of 0.7 and a charge O₂ concentration of 12.7%, conditions which were selected to allow comparison to Fig. 13. In this case, however, the pressure is not held constant, but is constrained to follow pressure traces typical of either late-injection PPCI [118] or early-injection PPCI [119] combustion measured in a light-duty engine. The upper figure corresponds to a late-injection condition, similar to the condition employed in Figs. 19 and 20. In contrast to Fig. 13, however, the initial temperature is increased to 870 K to reflect the higher temperature charge gas characteristic of near-TDC injection. The simulation commences near the beginning of the expansion stroke, at 4.5° ATDC. The lower figure corresponds to an early-injection condition. In this case, the simulation is initialized at -17.5° ATDC at an initial temperature of 802 K – which matches the initial temperature selected for the constant pressure simulations of Fig. 13. Discussion of the late-cycle simulation follows; discussion of the early-injection simulation is deferred until Section 5.3.

Comparison of the upper portion of Fig. 22 to Fig. 13 shows that charge expansion significantly changes the ignition kinetics. Due to the higher initial temperature, the first stage of ignition Fig. 22 (top) is considerably advanced relative to Fig. 13. However, the second stage pre-ignition period is somewhat longer than in Fig. 13, and

contains a short period of rapidly increasing temperature between 0.8 and 0.9 ms that is not seen in the constant pressure results. The gas temperature (sensible internal energy) is determined by both the chemical heat release and by the work done by the expanding gases. The short period of increasing temperature is not due to a local peak in the heat release rate, which begins to increase monotonically just before 0.8 ms. Rather, it is caused by the work term, which is increasing rapidly and which largely counterbalances the heat release beyond 0.9 ms. The expansion work is largest approximately 2 ms into the simulation; thereafter, as the pressure drops the work is reduced despite increasing piston speed and the temperature begins to rise more rapidly. Nevertheless, the peak temperature reached is considerably lower than with constant pressure, and the second-stage ignition period – during which CO is oxidized – spans several milliseconds. Note that during this period, the concentration of OH, which is the species predominantly responsible for oxidizing CO, is an order of magnitude lower than in the constant-pressure calculations.

Fig. 22 (top) shows that the UHC (and formaldehyde), as well as the vast majority of the CO, is ultimately oxidized under the late-injection condition with $\phi = 0.7$. However, the oxidation kinetics are very sensitive to the temperature history, which is closely linked to equivalence ratio or injection timing. The condition shown is on the very edge of acceptable combustion; a small reduction in ϕ can increase the yield (defined here as the mole fraction late in the cycle, at 90° ATDC) of each of these species dramatically. For example, with $\phi = 0.7$, the formaldehyde (H₂CO) yield is approximately 0.01 parts per million (ppm), but rises to near 1000 ppm when $\phi = 0.69$. Hence, the survival of formaldehyde on the left side of the images in Fig. 19 is fully expected for late-injection operation, and marks the presence of mixture with $\phi \leq 0.7$.

More generally, at a fixed time after injection, the chemical species present at a given location provide an indication of the local equivalence ratio. Thus, not only does the formaldehyde in Fig. 19 mark the presence of fuel-lean mixture (consistent with the late-cycle equivalence ratio maps in Fig. 8), but OH marks the presence of regions of intermediate stoichiometry where second-stage ignition occurs [98], and PAH marks regions where $\phi \geq 2$. Figs. 13 and 22 also show that when H₂CO and UHC oxidation is nearly complete, but OH concentrations are just beginning to rise, CO is reaching a peak. As a result, an important inference is that in regions of Fig. 19 near the border between formaldehyde and OH, we expect significant quantities of CO to be present.

To further examine the effect of equivalence ratio on oxidation kinetics, calculations such as those shown in Fig. 22 were performed for many equivalence ratios, using the same late-injection timing. The mole fraction of CO and UHC at 90° ATDC, when chemical reaction has essentially ceased, is shown as a function of ϕ in Fig. 23. Like H₂CO, both quantities show an abrupt increase when ϕ is reduced below 0.7. At these equivalence ratios, the temperature does not reach sufficient levels to promote breakdown of the H₂O₂ pool, and second-stage ignition is not achieved. Likewise, temperatures are reduced when the injection timing is further retarded, and the equivalence ratio at which this abrupt increase in UHC and CO emissions occurs shifts toward richer mixtures, as shown by the arrow in the lower portion of the figure. Superimposed on the plot is a Gaussian distribution that denotes a hypothetical equivalence ratio distribution. Timing retard at late-injection conditions also increases the ignition delay, and will shift the distribution toward leaner mixtures. These two effects thus reinforce each other, and are the probable cause of the rapid increase in CO and UHC emissions seen in late-injection PPCI combustion systems when timing is retarded excessively (see Fig. 1).

The CO and UHC behavior in Fig. 23 also helps explain the more rapid increase in engine-out UHC than CO as injection is retarded,

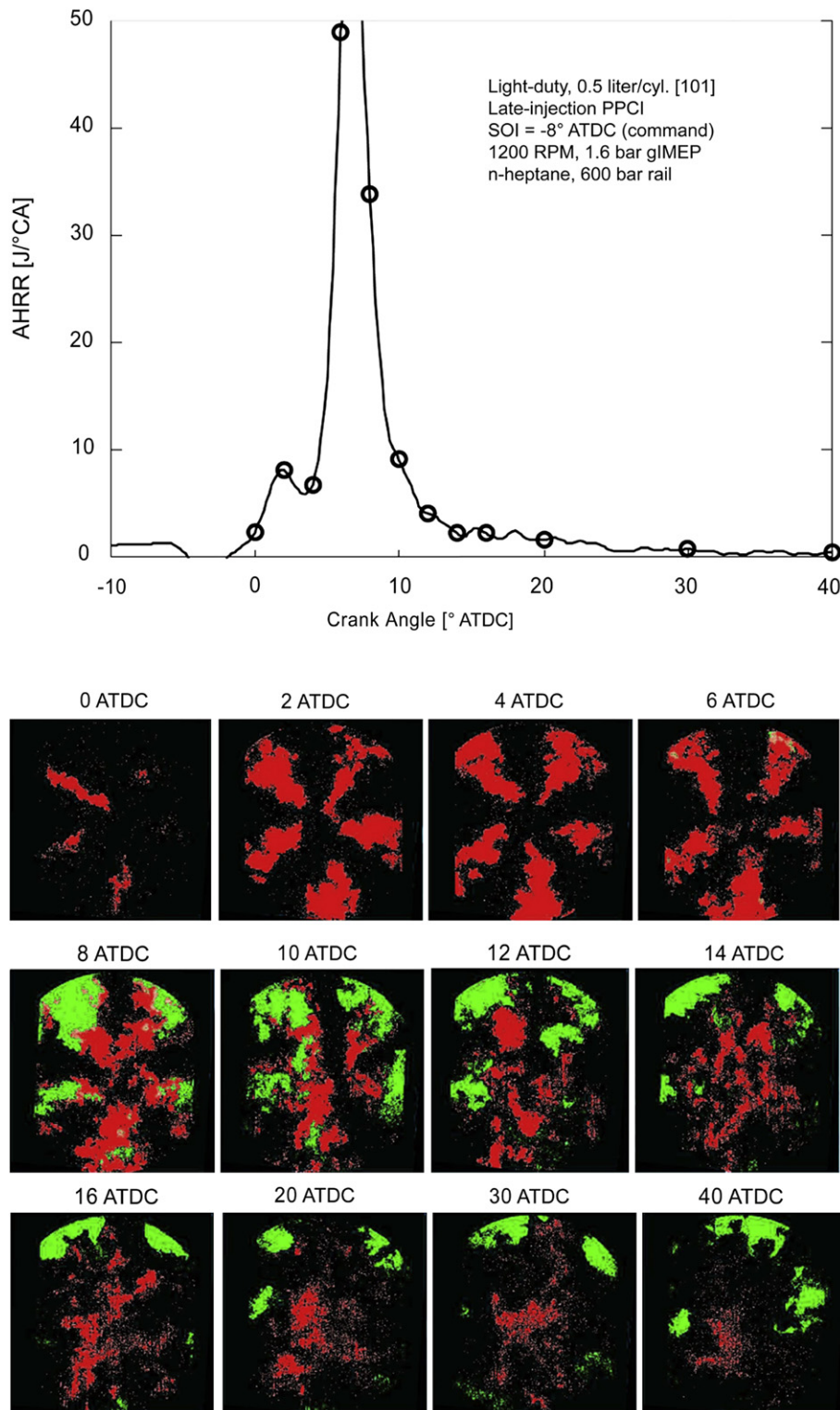


Fig. 21. Top: apparent heat release rate for a low-load, late-injection LTC condition in a light-duty engine [101]. Reprinted with permission, SAE paper 2004-01-2949 (c) 2004, SAE International. Bottom: simultaneous images of single-shot formaldehyde PLIF (red) and OH PLIF (green). The image timings are indicated by circles on the heat release rate plot. (For interpretation of the references to color in this figure legend, the reader is referred to the web version of this article.)

which is seen in Fig. 1. If the mixture distribution is shifted to the left, toward leaner equivalence ratios, emissions of UHC associated with lean mixtures will increase more rapidly than the CO emissions, due to the rapid fall-off of CO formation during the second-stage pre-ignition period at leaner equivalence ratios. In addition,

emissions of CO associated with under-mixed, rich regions will be reduced at a greater rate than UHC emissions, due to the differences in the CO and UHC for rich mixtures. While CO emissions are high for any mixture with insufficient O₂ to complete combustion, UHC emissions are not. Partial oxidation of UHC, forming H₂ and CO, can

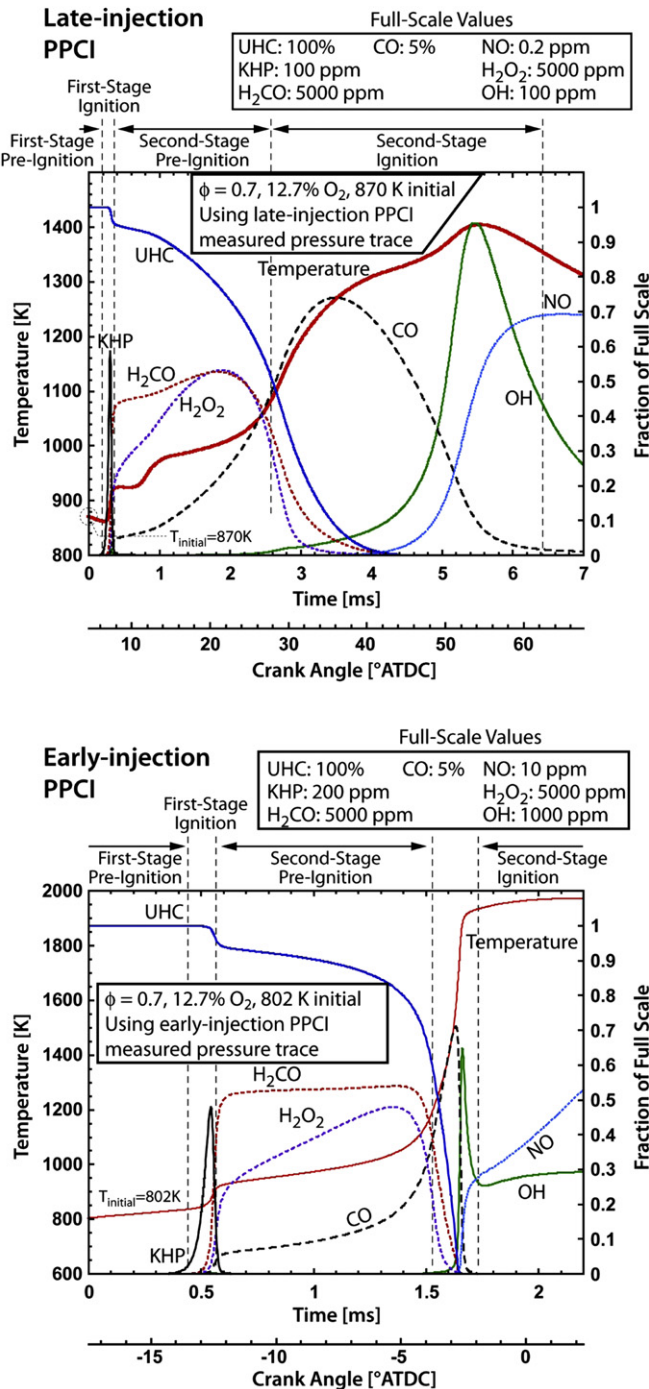


Fig. 22. Simulation of ignition of vapor-phase n-heptane using the LLNL/Galway-Mayo mechanism [93], allowing for pressure variation due to cylinder volume expansion for late-injection with initial temperature of 870 K (top) or cylinder volume compression for early-injection with an initial temperature of 802 K (bottom).

result in near-zero UHC emissions even for equivalence ratios considerably greater than unity.

5.3. Early-injection PPCI UHC and CO emission sources

Early-injection PPCI conditions do not suffer from incomplete combustion in lean regions to the same degree as late-injection PPCI conditions. For late injection, the cylinder contents cool during the expansion stroke, which inhibits the progression to

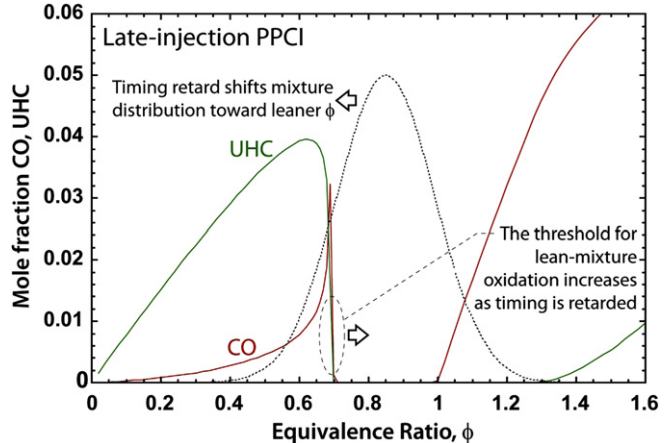


Fig. 23. Mole fraction of UHC (includes oxygenated compounds) and CO predicted by homogeneous reactor simulations as a function of ϕ . Conditions correspond to those of the upper portion of Fig. 22 (late-injection).

second-stage ignition. For early-injection LTC conditions, the cylinder contents are heated during the later part of the compression stroke, which helps to propel lean mixtures into second-stage ignition. As a result, much longer ignition delays (greater premixing) can be tolerated before UHC and CO emissions become problematic.

Support for these statements is found in a comparison of the evolution of the ignition process during compression (shown in the lower portion of Fig. 22) to the evolution under constant pressure conditions (Fig. 13). Although both simulations commenced at 802 K, first-stage ignition occurs approximately 0.2 ms earlier when compression heating of the charge gas accelerates the early ignition processes – despite the lower (38 bar) initial pressure. With compression, the pressure rises above 50 bar during first-stage ignition, and beyond this time the kinetics are accelerated relative to the conditions of Fig. 13 by both higher pressure and temperature. Second-stage ignition is accordingly advanced by approximately 1 ms. Note that the higher temperatures caused by charge compression lead to higher NO_x production, as well as higher peak and post-combustion OH concentrations. Both higher temperature and higher OH concentrations can be expected to increase the rate of CO oxidation, behavior which can be seen by comparing Fig. 13 with Fig. 22.

The impact of compression heating on the lean-mixture oxidation limits is clearly illustrated by the behavior of the CO and UHC mole fractions at 90° ATDC, which are shown in Fig. 24 for the pressure history and charge composition corresponding to the lower portion of Fig. 22. In contrast to the behavior observed with late-injection (Fig. 23), with early-injection the compression heating allows complete combustion of much leaner mixtures. The transition to high CO and UHC mole fractions as the mixture becomes leaner is also much more gradual, and occurs at a leaner equivalence ratio for UHC than for CO. These differences can be understood by examining the temporal variation of the various combustion intermediates such as those shown in Fig. 22 for these lean mixtures. As the mixture becomes progressively leaner (down to $\phi \approx 0.3$, for instance), the mixture still achieves second-stage ignition and UHC is consequently low. However, the process is slower and the expansion process begins to lower gas temperatures and impedes the full oxidation of CO. Only as the mixture becomes very lean (down to $\phi \approx 0.15$, for instance), does the process begin to resemble the late-injection process. In this case, the first-stage ignition process is sufficiently slow that expansion interferes with

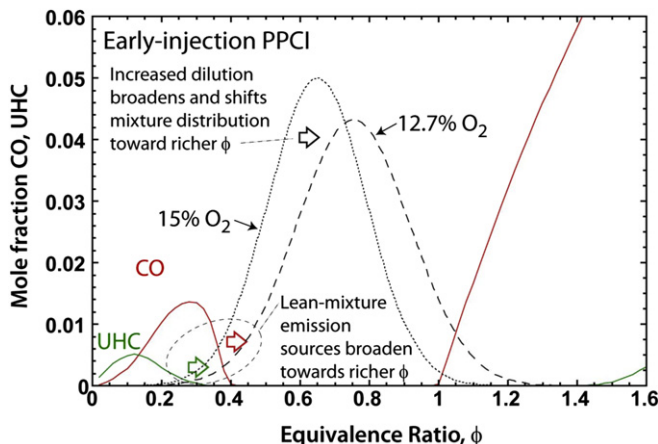


Fig. 24. Mole fraction of UHC (includes oxygenated compounds) and CO predicted by homogeneous reactor simulations as a function of ϕ . Conditions correspond to the lower portion of Fig. 22 (early-injection).

the transition to second-stage ignition, resulting in significant UHC (and H₂CO) and reduced CO formation.

5.4. The impact of dilution

The discussion in the previous two sections of the impact of expansion, compression, and equivalence ratio on the gas temperatures and on the subsequent oxidation process did not consider the impact of changes in dilution (EGR rate). Dilution will impact the oxidation process and UHC and CO emissions of both late- and early-injection combustion systems through at least three mechanisms:

- 1) The mixture equivalence ratio needed to achieve complete combustion of lean mixtures will increase as dilution is increased [123], because the heat capacity of the diluent gases keeps combustion temperatures low. This is shown by the arrows in the lower portion of Fig. 24. If the mixture equivalence ratio distribution is unchanged, the added dilution will increase both UHC and CO emissions.
- 2) If mixing processes are unchanged by dilution (that is, if the mixture fraction distribution does not change), then increasing dilution will broaden the equivalence ratio distribution and shift it toward richer mixtures – as shown by the hypothetical distributions superimposed on the figure. This will tend to reduce UHC and CO stemming from lean mixtures, counteracting the shift toward richer mixtures of the UHC and CO yield curves described in the preceding paragraph. However, emissions stemming from rich mixtures can be expected to increase.
- 3) Increased dilution will increase ignition delay, providing additional time for mixing if combustion phasing is held fixed. This will shift the mixture distributions back toward leaner mixtures, increasing UHC and CO emissions from lean mixtures and reducing emissions from rich mixtures. Indeed, equivalence ratio measurements in the igniting region of negative-dwell fuel sprays show no change in equivalence ratio distribution, because of this longer ignition delay [125].

The dominant source of UHC and CO emissions, for either rich or lean mixtures, will depend strongly on the specific mixture distribution formed, which will, in turn, be greatly dependent on the details of the operating condition and the engine geometry. However, whichever source is dominant, Fig. 24 shows that the yield of CO, expressed as a mole fraction, is considerably higher

than the yield of UHC for all but the leanest mixtures. Due to the narrower range of intermediate equivalence ratios providing a low CO yield, and the more rapid rise of CO yield at the edges of this range, it is not surprising that CO emissions are more problematic than UHC emissions in early-injection PPCI systems. Note further that, in spite of the lower heating value of CO compared to UHC, the energy content of the CO will also typically be greater than the energy content of the UHC – as is seen in the upper portion of Fig. 1.

5.5. Experimental measurements of late-cycle UHC and CO

There is considerable experimental evidence corroborating the understanding provided by the homogeneous reactor simulations described above. Evidence cited previously includes the persistence of formaldehyde in the upstream regions of the jet for the late-injection conditions of Figs. 19 and 20, the more rapid increase in UHC than CO when injection is retarded excessively for late-injection PPCI seen in Fig. 1, and the dominance of the CO emissions under early-injection LTC conditions with ignition delays comparable to the late-injection conditions of Fig. 19, formaldehyde is consumed and OH appears throughout a much larger fraction of the lean, upstream regions of the jet, in accordance with the difference in lean mixture UHC yields seen when comparing Fig. 23 to Fig. 24 and consistent with the promotion of second-stage ignition by charge compression. Moreover, exhaust measurements show that UHC emissions are highest under two types of conditions studied [126]. The first is when injection is late and ignition occurs shortly after the end of injection, similar to the conditions of Fig. 19. The second is when injection is very early so that the ignition dwell to first-stage ignition is very long (10°). Under such conditions, Fig. 8 shows that much of the jet reaches very low equivalence ratios ($\phi \leq 0.3$). According to Fig. 24, these very lean mixtures result in significant UHC emissions, even with the compression-heating effect.

The behavior of CO emissions can be expected to be similar to the UHC emission behavior described above. Indeed, similar trends in light-load UHC and CO emissions are usually seen when various combustion parameters are varied, e.g. [127]. Like NO, CO is a difficult species to probe with laser diagnostics. Currently, measured in-cylinder spatial distributions of CO are only available in light-duty engines, where the jet structure has been deformed and deflected by the piston bowl-wall. Nevertheless, these distributions, and their behavior relative to UHC distributions, provide further strong support for the concepts outlined above. Fig. 25 shows reconstructions of late-cycle, ensemble-averaged CO and UHC distributions in a vertical plane through the center of the combustion chamber for early-injection LTC conditions at three different loads. The reconstructions are based on spectrally-resolved laser-induced fluorescence (LIF) measurements, which allows the fluorescence signal to be decomposed into contributions from CO and C₂, as well as a broadband background component [123]. The UHC shown in Fig. 25 is derived from the C₂ signal. C₂ is formed by photofragmentation of various combustion intermediates by the CO probe beam, and is an indicator of partially-oxidized fuel. The C₂ signals are generally low in regions where mainly un-oxidized fuel is expected, even though the overall fluorescence intensity can be quite high.

Before continuing further with a discussion of in-cylinder CO and UHC measurements, a brief review of the evolution of the in-cylinder mixture distribution elucidated by imaging studies and supporting multi-dimensional simulations is warranted (it might also be helpful to look forward to Fig. 32 where this evolution is illustrated schematically for light-duty engines). As discussed in the context of Figs. 6 and 16, in light-duty engines with a conventional

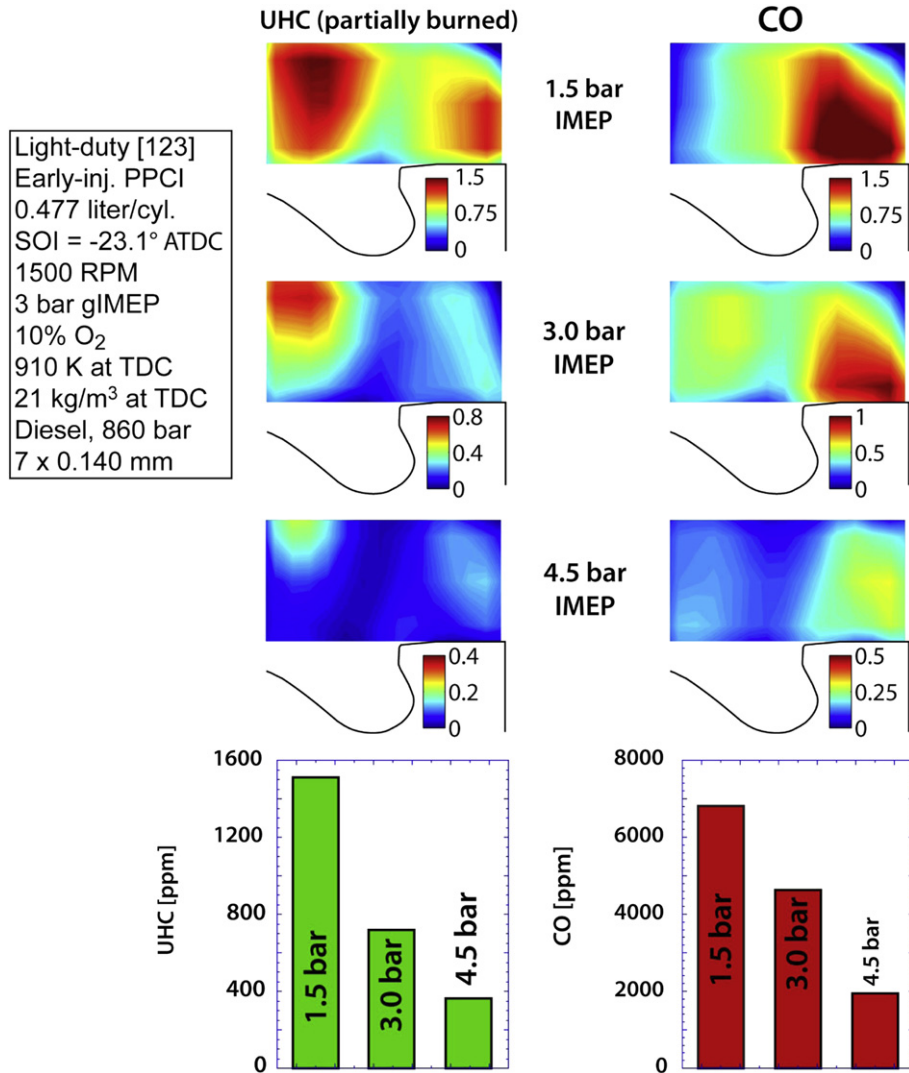


Fig. 25. Ensemble-averaged reconstructions of late-cycle UHC and CO distributions measured at 50° ATDC for an early-injection LTC condition using a spectrally-resolved line-imaging LIF technique (unpublished, from dataset of Ref. [123]). Measurements do not include the bowl region.

wide-angle injector geometry and typical spray targeting, much of the fuel jet is deflected into the bowl by the bowl lip, though some is directed into the squish volume. Of the fuel that enters the squish volume, mixtures near the head of the jet that penetrate farthest are likely to remain in the squish volume. As shown in Fig. 16, and analogous to Figs. 8, 14 and 15, this mixture will be richer than the average. Hence, mainly leaner mixtures are forced out of the squish volume by the rising piston, and will be located near the bowl rim at the start of combustion. Likewise, lean mixture from the tails (upstream regions) of the fuel jets will be found near the bowl rim and in the upper, central region of the combustion chamber. This behavior is illustrated by the fuel and subsequent H₂CO distributions shown in Fig. 16. At the start of the second-stage ignition process, richer mixtures characteristic of the head of the jet are found deep in the bowl, while leaner mixtures from the edges of the fuel jets and from the lean upstream regions of the jet are found near the bowl rim. Much of the remaining fuel that was injected directly into the squish volume has formed near-stoichiometric mixture, though lean regions exist at the edges of the jets and imaging studies indicate that fuel films on the head and piston surface may be found at the outer cylinder radii.

During second-stage ignition, rapid volume expansion within the bowl forces much of the lean, near-rim mixture into the squish volume. As combustion further progresses, this process is assisted by squish-volume expansion due to piston motion. Meanwhile, the near-stoichiometric mixtures in the squish volume achieve second-stage ignition and complete the oxidation process, leaving only the slower-reacting, leaner mixtures. Heat losses in the squish volume can be expected to further slow the ignition and oxidation of the remaining, lean squish volume mixtures.

The CO distributions in Fig. 25 provide considerable support for the above description of the light-duty mixture formation and combustion processes. At each of the engine loads investigated, CO is observed late in the cycle, and is concentrated within the squish volume. As the load increases, the squish-volume CO decreases, in close correspondence with the measured engine-out CO emissions, shown in the lower portion of Fig. 25. Although these emissions were measured in the optical engine, a detailed comparison has shown that the engine-out emissions of a geometrically similar single-cylinder metal engine can be quantitatively reproduced [128].

Two factors are primarily responsible for the decrease in CO with load. First, the formation of over-lean mixtures is lessened.

Higher-load conditions require longer injection durations and have shorter ignition delays. Thus, the injection dwell, or time for pre-mixing before ignition, is shorter. Fig. 8 shows that with a shorter ignition dwell, the upstream regions of the fuel jets will be more fuel-rich, and thus more likely to achieve second-stage ignition and complete the oxidation of CO. Moreover, with higher load, the amount of fuel injected directly into the squish volume is greater, and lean mixture formed in this region is likely to be less prevalent.

The second effect that reduces in-cylinder CO is the higher cylinder pressures achieved at higher loads. Apart from directly increasing reaction rates, the higher pressures also increase temperature through increased compression-heating. The pressure differential between first-stage ignition and peak pressure is only about 15 bar for the lightest-load condition in Fig. 25, but over 30 bar for the highest load. The higher pressures and temperatures reinforce the impact of generally richer mixtures, pushing more of the leaner mixture into second-stage ignition and thereby reducing in-cylinder CO.

The monotonic decrease in UHC with increasing engine load observed throughout the cylinder, as indicated in Fig. 25, is similar to the behavior of CO within the squish volume. However, in the upper-central regions of the cylinder, the CO first increases as load increases, then decreases again at the highest load. This behavior is fully consistent with the ignition kinetics illustrated in Figs. 12, 13 and 22. At the lowest load, 1.5 bar, there is a large amount of UHC in this region, due either to very lean mixtures expected near the injector (Fig. 8), or to fuel which is made available for mixing and combustion late in the cycle (while expansion is occurring, as described in the next paragraph). In either case, the progress of the ignition and oxidation process will be slow. As the load increases, higher pressure, temperature, and possibly richer mixtures will all result in accelerated progress toward second-stage ignition, reducing UHC and forming greater amounts of CO. Only at the highest load is the ignition process sufficiently accelerated that a large fraction of the fuel completes the second-stage ignition process and both CO as well as UHC decrease.

The source of the fuel introduced late in the cycle requires some explanation. Late introduction of fuel can be caused by poor near-injector atomization and vaporization (e.g. Figs. 4 and 6) or by dribbling of fuel from the injector sac volume and holes. With sac-type nozzles, dribbling of fuel from the injector has been shown to be a significant source of UHC under conventional diesel combustion conditions [129]. Recent studies have shown that injector sac and hole volume dribbling can also be an important source of UHC for low-temperature PPCI operation. In fact, dribbling from the injector sac may be a more significant source of UHC for LTC than in conventional combustion because the strongest combustion is far downstream of the injector for LTC. Variation of the nozzle sac volume has shown that, at the 3 bar, light-load condition considered, injector dribbling is responsible for roughly 15% of the engine-out UHC emissions [130]. LIF images of in-cylinder UHC distributions and elastic-scatter images show clear evidence of liquid droplets within the cylinder, which persist until well into the expansion stroke. Examples are shown in Fig. 26 (heavy-duty) and Fig. 27 (light-duty), and droplets can also be clearly seen in Fig. 20. Close examination of elastic scatter images indicates that the flux of liquid from the injector in Fig. 27 increases near 20–25° ATDC [119], when cylinder pressures have dropped to levels comparable to those present during the fuel injection event.

The presence of liquid droplets implies rich mixtures near the droplets due to recently vaporized fuel. Hence, the diffuse, gas-phase UHC in Fig. 27 could correspond to either lean mixture created by increased mixing after the end of injection (cf. Fig. 8), and/or to rich mixture from fuel which has only recently vaporized. Indeed, direct evidence of rich mixture near the injector is provided

by the late-cycle emergence of soot luminosity [113]. Figs. 13, 22, and 24 all show that the CO and UHC yield will usually be high for fuel-rich mixtures because of the oxygen deficit. Although the general reduction in UHC and CO with increasing load (richer mixtures) in Fig. 25 indicates that the source of most of the UHC and CO at the low-load condition investigated is fuel-lean mixtures, some UHC and CO may arise from rich mixtures. In addition to rich mixtures near the injector, rich mixture from the head of the fuel jet rising out of the bowl may be contributing to the CO remaining below the injector for the 4.5 bar IMEP condition in Fig. 25.

Overall, the picture that emerges is one in which the mixture near the injector is comprised of lean mixture formed by enhanced mixing after the end of injection, within which liquid droplets and pockets of rich mixture associated with fuel introduced late in the cycle are embedded. For low-load LTC conditions, the general effect of mixing after combustion is to push all mixtures toward more fuel-lean conditions. As a result, under low-load conditions with sufficient excess oxygen and sufficient post-combustion mixing time, CO stemming from rich mixtures will tend to be oxidized, along with soot and other products of rich combustion. Indeed, conventional diesel jets undergo significant fuel-rich combustion, and yet CO emissions are relatively low because of sufficient oxidation as the rich post-combustion gases mix with additional ambient O₂. For fuel-lean mixtures, by contrast, increased post-combustion mixing with ambient gases inhibits CO oxidation. As a result, most exhaust CO emissions for low-load PPCI conditions likely stem from fuel-lean mixtures.

Two additional sources of emissions can be identified from late-cycle images of UHC distributions. The first source is associated with the liquid and gaseous fuel that is injected into the squish volume under early-injection PPCI operation (see Figs. 6 and 16). Some of this fuel can penetrate sufficiently far into the squish volume that it is compressed into the top ring-land crevice as the piston rises. During expansion, the crevice UHC is released and, for optical engines with large crevice volumes, can be found in a corner vortex formed by the fluid leaving the crevice. This vortex, and its embedded UHC, is illustrated in the lower portion of Fig. 28.³ Notice that corner vortex UHC is not present on all cycles, as indicated by the single-cycle image in the upper portion of the figure. Multi-dimensional simulations indicate that a distinct, rotating corner vortex is only formed when the crevice volume is large [132]. However, in engines with a ring-land crevice volume typical of a serial production engine, crevice UHC will still be expected in a stagnant pocket of fluid in the cylinder corner. From estimates of the contribution to engine-out UHC due to injector leakage and of the reduction of gas-phase (lean-mixture) UHC observed as engine load is increased, the contribution to engine-out UHC emissions from the ring-land crevice can be estimated to be less than 20% at light loads [130].

The second obvious source of UHC emissions is the slow vaporization of liquid fuel deposited on piston or liner surfaces. Example images indicating the presence of these films are shown in Fig. 28. Bright regions of fluorescence are evident above the piston top within the squish volume. This fluorescence likely originates from the liquid films themselves or from PAH or soot LII in the rich mixtures above the films.

The importance of these liquid films to UHC emissions is likely to depend strongly on injector, bowl design, injector timing, and

³ Corner vortex UHC is not apparent in the images of Fig. 25, which were obtained 20° later in the cycle. However, UHC distributions using the measurement technique of Fig. 25, obtained at the same crank angle as Fig. 28, clearly show the corner vortex. Residual swirl likely rotates the corner vortex UHC out of the measurement plane by 50° ATDC.

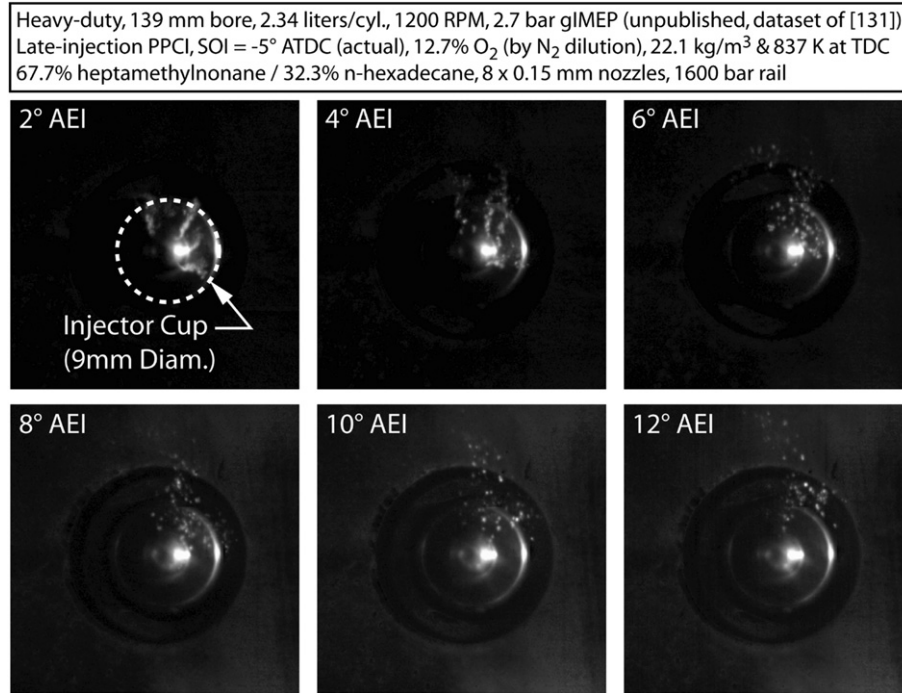


Fig. 26. Mie-scatter images of liquid droplets near the injector in a heavy-duty engine (bottom view) under late-injection PPCI conditions (data not previously published, but from dataset of [131]). The camera exposure is constant, but the illumination is brighter in later images because of increasing combustion luminosity.

engine load for various LTC engines. Experimental evidence suggests that liquid penetration into the squish region is to be avoided, as UHC emissions are generally higher [134,135]. While liquid films formed in the piston bowl region are not desirable either, there appears to be more tolerance to wall wetting here because hot combustion within the bowl tends to vaporize remaining liquid fuel more effectively, and oil-dilution by the fuel spray is avoided. Narrow-angle injection systems coupled with special bowl designs have been implemented, which intentionally deposit liquid fuel onto the piston bowl [81,82,136] and permit earlier injection timing. For example, Fig. 29 shows images of fuel-tracer fluorescence in the expansion stroke and fuel-cloud Mie-scattering in the exhaust stroke for a narrow-angle early-injection LTC condition in a light-duty engine [81]. The fuel-tracer fluorescence images (left) are from an optical engine, and show strong fuel

fluorescence near the bottom of the piston bowl. The Mie-scatter image is from a metal engine with endoscope access, and shows fuel clouds above the piston bowl that are present during the exhaust stroke, and that arise from fuel films that are deposited from the early injection during the compression stroke. Fig. 10 provides another example of liquid films within the piston bowl for an engine equipped with a narrow included-angle injector. The contribution of these fuel films to UHC emissions relative to bulk gas sources will depend upon the particular engine design and operating point. Nevertheless, studies agree that when liquid film formation occurs UHC and CO emissions generally increase [28,81,84].

6. LTC conceptual models and summary

As a summary of the observations from optical diagnostics, chemical kinetics simulations, and discussions in the preceding sections, we offer extensions of Dec's conceptual model for conventional diesel combustion [44]. The models are for highly dilute (~13% intake O₂), low-load (~4 bar gIMEP) conditions with ignition occurring at or after the end of injection. The first conceptual model for low-load LTC conditions is applicable to heavy-duty engines, in which the fuel-jet structure is less perturbed by in-cylinder surfaces and flows. The second pair is for light-duty engines with either early or late injection, in which in-cylinder surfaces and flows significantly deflect the fuel jets.

6.1. Single-injection, EGR-diluted PPCI in heavy-duty engines

Fig. 30 shows illustrations of a conventional diesel combustion model, (left column) and the extension for low-load, single-injection, EGR-diluted, partially premixed low-temperature DI diesel combustion (middle and right columns). The heavy-duty extension applies to both early and late injection conditions, though the spatial extent of some features (e.g., liquid fuel penetration) and the

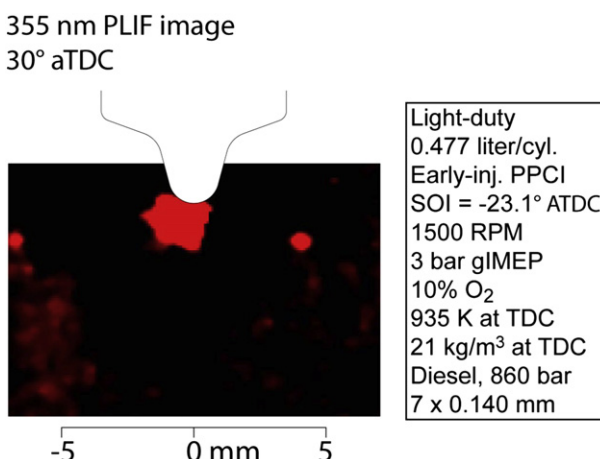


Fig. 27. Side view of liquid droplets and diffuse, gas-phase UHC near the injector same light-duty engine as Fig. 20 (data not previously published).

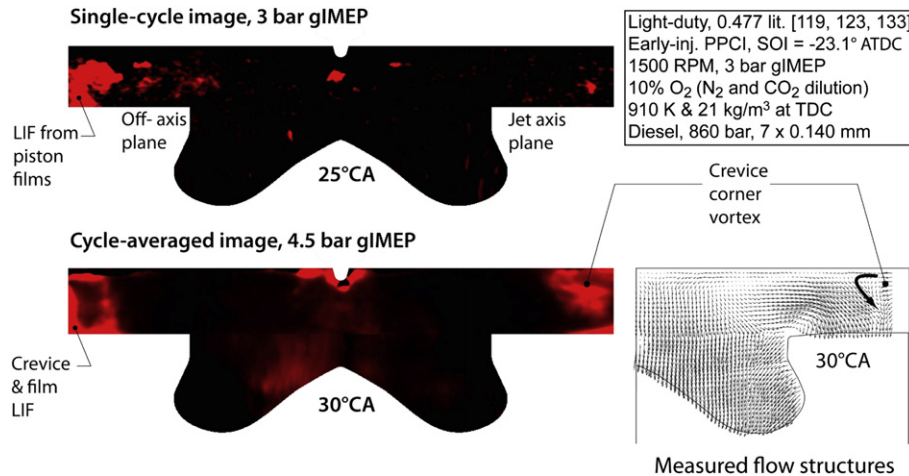


Fig. 28. Left: Images of UHC associated with fluid from the top ring-land crevice and piston-top fuel films formed under early-injection, PPCI combustion conditions in light-duty engines (top image from [119] Reprinted with permission, SAE paper 2009-01-1446 (c) 2009, SAE International; bottom image unpublished, from dataset of [123]). Bottom-right: PIV flow measurements showing corner vortex [133].

timing of some events (e.g., ignition) will shift depending on operating conditions and fuel injection timing, as described in the following discussion.

The conventional diesel combustion model originally proposed by Dec has been modified slightly to include contributions from Refs. [44,47,48,50,59,60]. The conceptual model has been simplified somewhat, in that both soot and its precursors are represented by a single color (red), since no such distinction is yet available for LTC conditions. In addition, the conventional model shown includes formaldehyde (first-stage ignition), which was not drawn schematically in the original model of Dec [44]. A comparative description of the evolution of diesel combustion for conventional and LTC conditions follows.

For the first three crank angle degrees (~ 0.5 ms) of the fuel injection, the evolution of the diesel jet is similar for conventional and LTC conditions. Liquid fuel (dark brown) and vapor (light brown) fuel penetrate together until near 3° ASI, after which the vapor penetrates beyond the liquid. For early-injection LTC conditions into lower-temperature, less dense ambient gases, the jet penetrates somewhat faster, and the liquid length (35 mm or more) is typically longer than for conventional conditions (~ 25 mm). For late-injection LTC conditions, with fuel injection near TDC, the temperature and density of the in-cylinder gases are comparable to

conventional diesel conditions, so the jet penetration rate and liquid length are also similar. For the low-load LTC conditions, injection is shorter than for conventional diesel jets, so that the injection rate peaks shortly after, or even before, the quasi-steady liquid length is established.

After the injection rate peaks, the deceleration of the liquid fuel exiting the nozzle increases local entrainment of ambient gases near the nozzle. Jet model simulations show that the region of increased entrainment propagates downstream in a wave at twice the jet penetration rate. The head of the entrainment wave, which initiates at the peak injection rate near 5° ASI, is indicated by a vertical dotted line. As the injection rate ramps down and ends, the entrainment wave propagates downstream, temporarily increasing entrainment in its wake. The fate of the liquid fuel spray after the peak injection rate depends on the duration of the end-of-injection transient relative to the time for convection of jet fluid to the liquid length. Typically, the duration of the end-of-injection transient is comparable to the liquid-length convection time. As a result, after the head of the entrainment wave passes the liquid length at 7° ASI, increased mixing helps to vaporize the downstream portions of the fuel jet and the instantaneous liquid length typically shortens. Under the PPCI conditions explored here, fuel is fully vaporized within 1° after the end of injection. For conditions

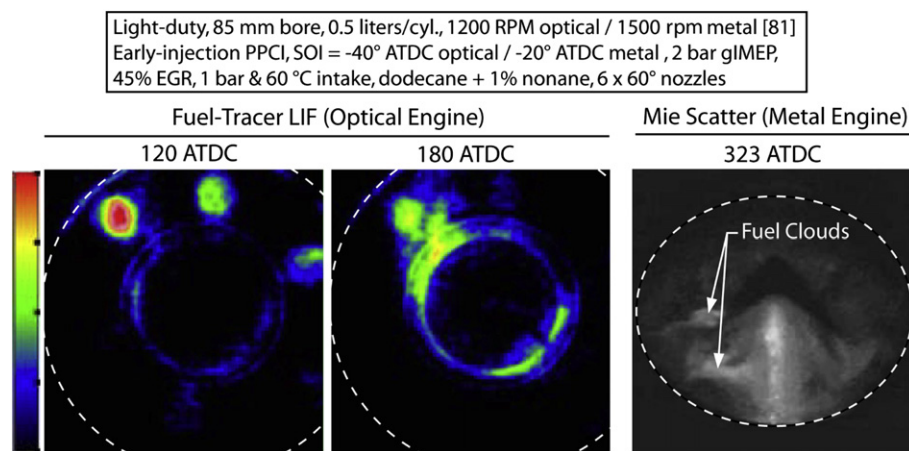


Fig. 29. Ensemble-averaged fuel-tracer fluorescence in an light-duty optical engine (left) and endoscope view of Mie scattering from liquid fuel clouds in a light-duty metal engine (right) for an early-injection LTC condition with a narrow-angle injection system [81]. Reprinted with permission, SAE paper 2007-01-1836 (c) 2007, SAE International.

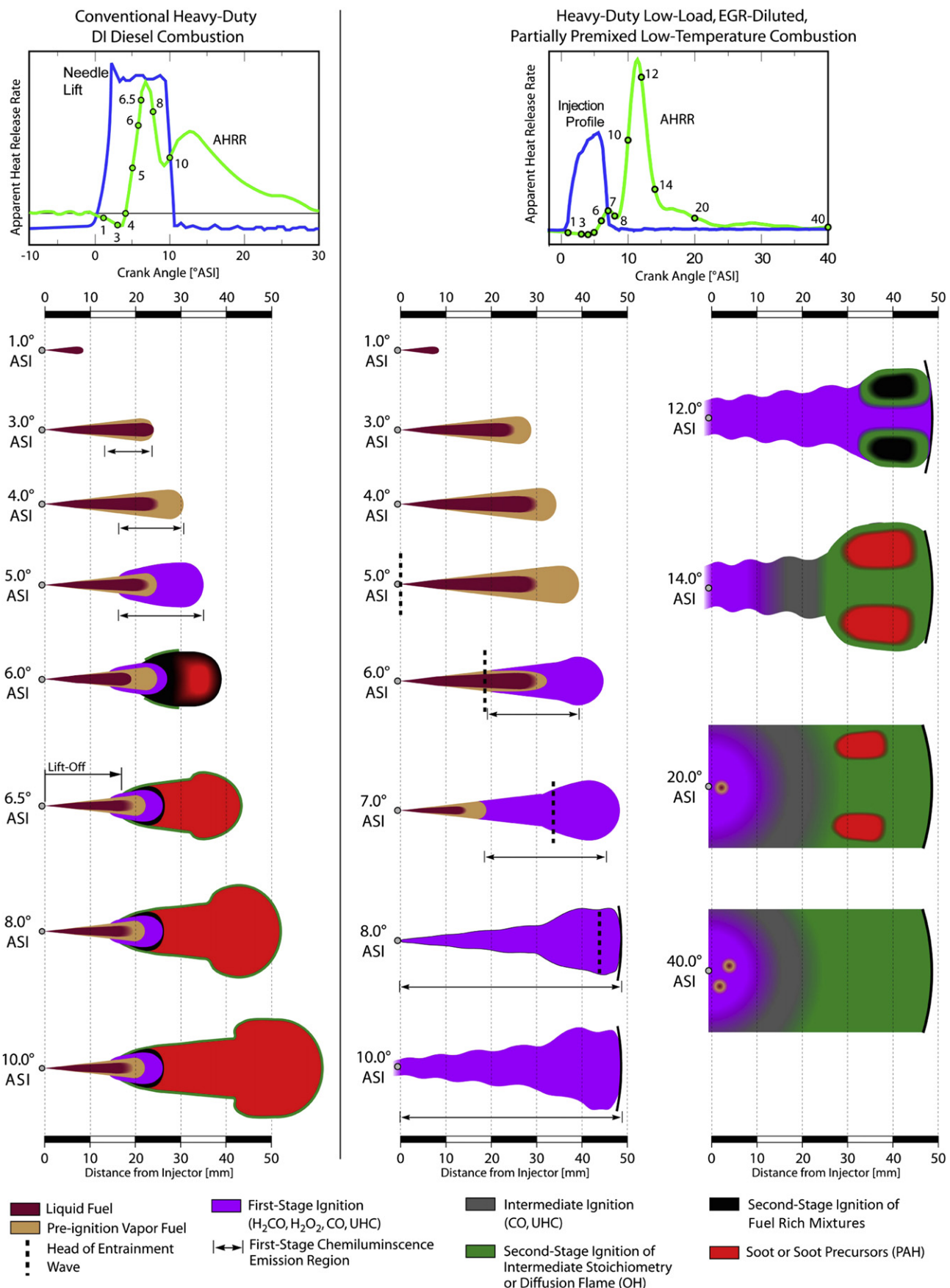


Fig. 30. Conceptual model for conventional heavy-duty diesel combustion (left column) and extension to low-load, single-injection, EGR-diluted, PPCI low-temperature heavy-duty DI diesel combustion (middle and right columns).

with relatively longer liquid-length convection times, such as very early injection into cooler and less dense ambient gases, or injections with a more rapid end-of-injection transient, the liquid spray may either detach from the injector or separate into individual segments (not shown), and may persist as liquid much later into the cycle. For all jets, however, penetration is reduced after the entrainment wave reaches the head of the jet, and mixing and fuel vaporization are enhanced in the wake of the entrainment wave, so that wall-wetting can be mitigated to some degree by shortening the injection duration.

After the initial jet penetration, the ignition processes for the LTC jet diverge from those of the conventional jet. Chemiluminescence emission from first-stage pre-ignition reactions (indicated by double-ended arrows) appears early in the downstream part of the conventional jet, near 3° ASI. For the LTC jet, chemiluminescence emission is not detectable until later, near 6° ASI for the conditions explored here. For the conventional jet, the premixed burn occurs within 1–2° after chemiluminescence is first detectable, and no clear distinction between first-and second-stage ignition is discernible in the AHRR. For the LTC jet, the chemiluminescence persists much longer, and the AHRR shows a distinct first-stage ignition event near 7° ASI. Formaldehyde (violet) appears throughout much of the jet at first-stage ignition, from fuel-lean to fuel-rich mixtures. Formaldehyde also forms during first-stage ignition for conventional diesel combustion [47,50,59], even in fuel-rich regions that later form soot. The appearance of formaldehyde during the early stages of combustion, for both conventional and low-temperature combustion, is consistent with chemical kinetics modeling results for both fuel-rich and fuel-lean reactions – as given in Fig. 13, for example.

Depending on the timing of first-stage ignition relative to the end of injection for LTC, the first-stage ignition heat release may help to vaporize liquid fuel, especially in the downstream parts of the jet. After the end of injection, the boundaries of the jet gradually widen from the more strictly conical shape established during injection, and the boundaries of the jet show structure, as the boundaries of formaldehyde fluorescence and equivalence ratio contours become wavy. Very late in the cycle, as the jet continues to widen, the original conical jet structure is no longer distinguishable, with adjacent jets blending into each other.

For conventional diesel conditions, portions of the jet that first ignite are fuel-rich and soot precursors (red) appear during the premixed burn, followed by soot formation (also red) a short time later. The timescales of second-stage ignition, OH formation, and soot precursor formation are very short because of the rapid temperature increase. OH (green) may appear in isolated spots at the periphery of the jet [111] at close to the same timing as soot precursor formation (see schematic at 6° ASI) [50], indicating nearly simultaneous combustion of fuel-rich and intermediate stoichiometry regions of the jet. Within a short time after ignition, the OH layer grows to form a diffusion flame on the periphery of the jet [50,111]. A zone of first-stage combustion products (formaldehyde) persists upstream of the lifted diffusion flame (i.e., the OH layer) [48,50]. The degree of premixing of fuel with ambient gases upstream of the lift-off length is critical for soot formation in the jet. During the processes of second-stage ignition, the liquid length decreases somewhat, likely due to local temperature rise at the onset of combustion, including a temperature increase because of compression heating from the premixed burn.

For LTC conditions, fuel injection ends before second-stage ignition, so that a quasi-steady lift-off length cannot be established. Instead, OH appears near the peak of the second-stage ignition AHRR, and it is distributed through much of the downstream jet cross section where mixtures are of intermediate stoichiometry. Some thin structures are apparent at the initial

appearance of OH, but within a few °CA, the OH distribution becomes more uniform across the downstream jet. The OH and formaldehyde distributions do not overlap spatially, consistent with chemical kinetics considerations. Some fuel-rich pockets (black) are evident in the downstream jet, where formaldehyde is consumed but OH does not appear because the mixtures are too rich to accumulate significant OH, consistent with chemical kinetics simulations. A few crank angle degrees later, soot precursors and/or soot appear within the rich pockets, typically surrounded by OH. Unlike conventional diesel jets, for which soot fills the jet cross-section, the soot pockets for LTC jets form far downstream, near the head vortex, or in regions where neighboring jets interact after impinging on the piston bowl-wall. Similar conceptual soot distributions have been proposed for comparable conditions, based on multi-dimensional model predictions [34]. After initially growing in size, the soot pockets gradually oxidize as the cycle progresses.

The original conceptual model for conventional diesel combustion applied only through the quasi-steady period, prior to the end of injection, so it did not describe late-cycle processes occurring after the end of injection. Later works showed that the soot in the jet could persist late in the cycle for some conditions, and its oxidation depended on the fate of OH [120].

For PPCI conditions, downstream fuel-rich and intermediate stoichiometry mixtures reach second-stage ignition, but upstream fuel-lean mixtures may not have sufficient time to fully ignite before expansion-cooling as the piston moves back down. For early-injection LTC conditions, compression-heating after first-stage ignition can help to propel fuel-lean mixtures into second-stage ignition, especially at higher loads. For conditions with very long ignition dwells, or for late injections, however, the fuel-lean mixtures near the injector typically do not reach or complete the second-stage ignition process. As a result, formaldehyde, UHCs, and CO persist late in the cycle, in the fuel-lean mixtures between the injector and the richer downstream regions where OH appears during second-stage ignition. Chemical kinetics simulations predict that some CO should exist in any fuel-lean mixture that has reached first- but not second-stage ignition. Within those regions, CO should reach a peak (gray zone) near the boundary between downstream mixtures that have reached second-stage ignition and leaner upstream mixtures that have not. CO should also form in the same fuel-rich mixtures that form soot and its precursors, but late-cycle mixing and combustion likely oxidizes much of the rich-source CO for low-load PPCI conditions.

Finally, late in the cycle, liquid droplets can dribble from the injector holes and/or sac volume. They may create locally fuel-rich regions and can contribute modestly to unburned hydrocarbon and CO emissions.

6.2. Single-injection, EGR-diluted conditions in light-duty engines

In light-duty engines, the physical and chemical processes of fuel jet mixing and ignition are similar to those in heavy-duty engines, though the mixing processes can be impacted considerably by interaction of the fuel jet with the piston bowl-wall and cylinder wall. Swirling in-cylinder flows, with radial and axial gradients in the swirl velocity, also sweep the fuel away from the jet axis and cause further distortion of the jet structure. Despite these complicating factors, an approximate picture of how the low-temperature combustion conceptual model applies to light-duty engines is presented in Figs. 31 and 32. Both figures depict the evolution of the fuel distribution and the combustion process in a plane that nominally intersects the center of the jet structure at each crank angle. Considering the differences in spray penetration and interaction with the piston bowl between early- and late-injection PPCI combustion systems, there are surprising

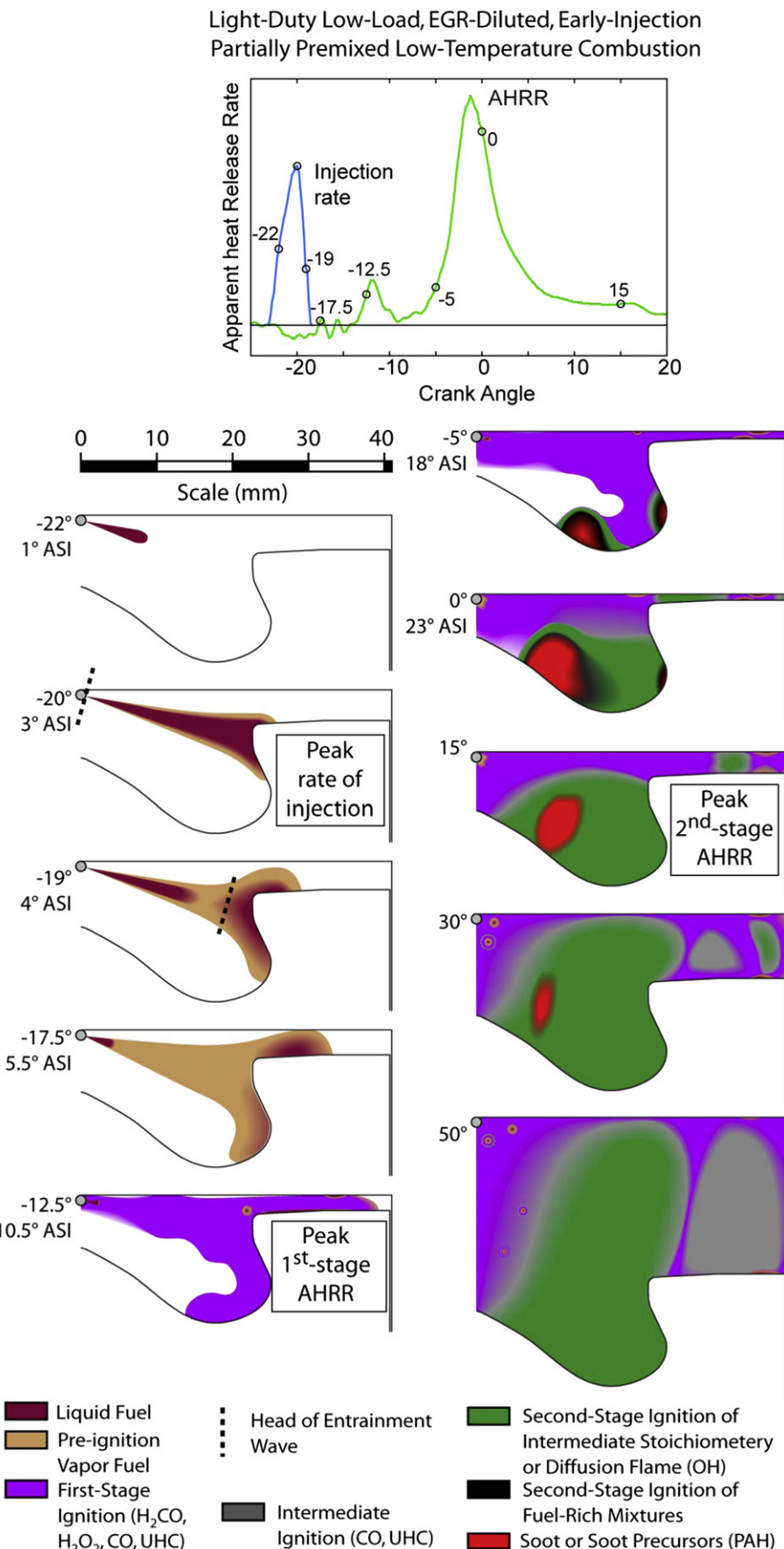


Fig. 31. Conceptual model for single early-injection, low-load, EGR-diluted, PPCI low-temperature light-duty DI diesel combustion.

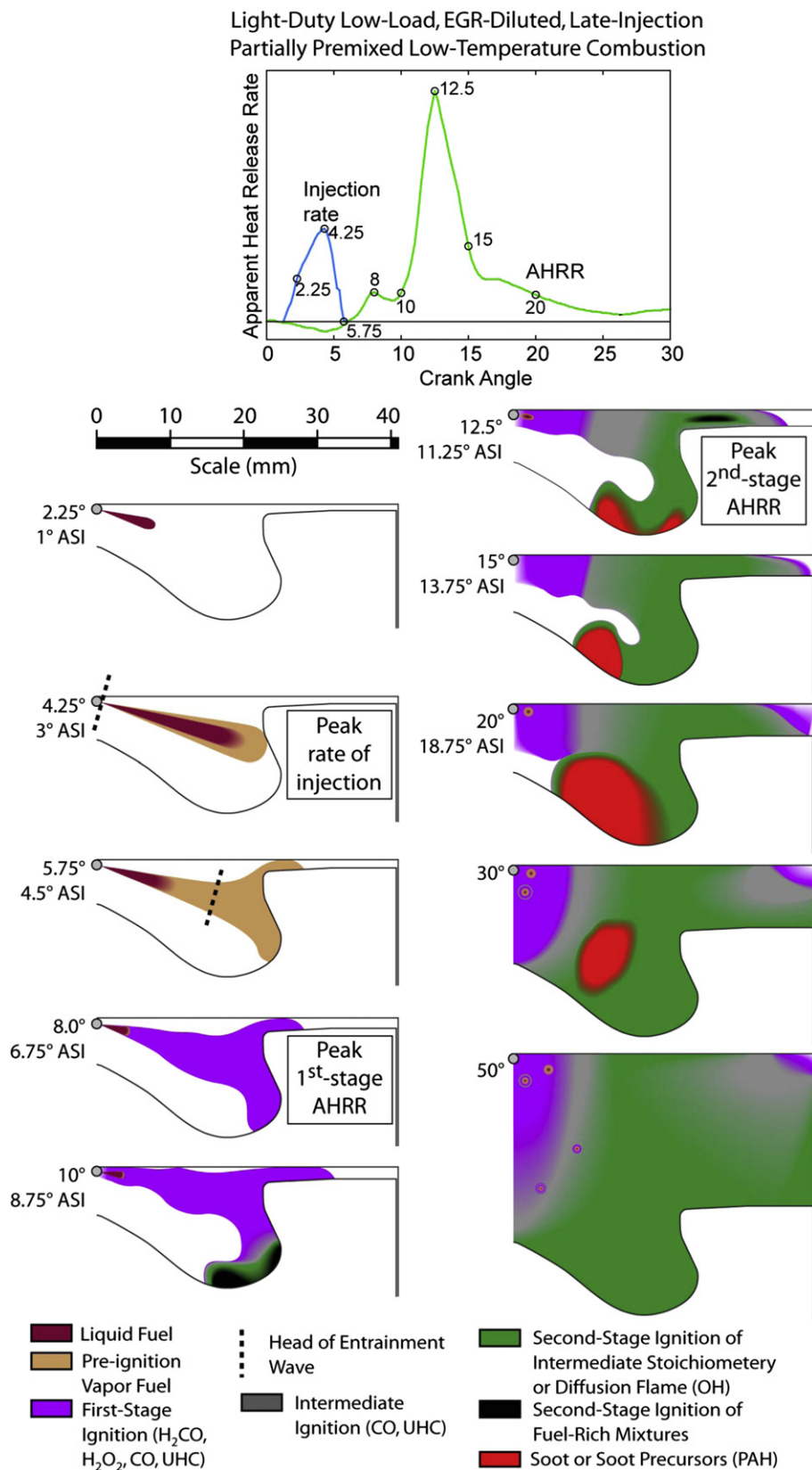


Fig. 32. Conceptual model for single late-injection, low-load, EGR-diluted, PPCI low-temperature light-duty DI diesel combustion.

similarities in the evolution of the combustion process. Nevertheless, separate schematics for both systems are provided, since there are important differences between the two.

Like the behavior seen in heavy-duty engines, liquid and vapor fuel initially penetrate together, with little difference seen in the penetration of the two phases. The jet penetration rate is higher with early injection (Fig. 31) than with late injection (Fig. 32), due to the lower ambient density at the time of injection. For the light-load considered here, the peak rate of injection occurs at 3° ASI. As the injection rate falls after 3° ASI, the entrainment wave is initiated at the injector, but with early injection (SOI ~ -23° ATDC) the liquid phase has already impacted the bowl rim. With late injection (SOI ~ 1.25° ATDC), the maximum liquid penetration is 1–2 mm short of the rim. Near the end of injection at 4.5° ASI, the liquid core retreats toward the injector much like for the heavy-duty engine, which is consistent with increased vaporization due to enhanced mixing after the passage of the entrainment wave. In the case of early injection, liquid fuel also remains near the bowl rim, at the head of the jet. The liquid near the bowl rim persists for a few more °CA, and penetrates farther into the squish volume and deeper into the bowl, as well as leaving a fuel film around the bowl rim. Generally, the maximum liquid penetration is similar to the maximum observed vapor penetration.

Focusing first on the late-injection schematic in Fig. 32, the delay from SOI to the first stage of ignition (about 7° CA) is approximately 4° CA less than for early-injection, as expected from the higher temperature and density at the time of injection and the simulation results shown in Fig. 22. However, mixing rates are expected to be somewhat greater with late-injection due to the higher ambient density, and late-injection operating modes typically have a higher O₂ concentration in the intake charge. These factors will counteract the reduced mixing times as compared to early-injection combustion systems. The fuel sprays also impact the piston at a point lower in the bowl with late injection. Overall, we expect mixture distributions formed during the ignition delay period to be similar to those shown for the early-injection operating condition of Fig. 16, though with leaner mixtures and less penetration in the squish volume and richer mixtures within the bowl.

Shortly after the first stage of ignition, just as the heat release associated with the second stage of ignition is starting, a two-zone spatial distribution of fluorescence is regularly observed deep in the bowl. The two zones are often separated by a fluorescence-free zone. Although the mixture preparation processes leading to this two-zone structure are not well understood, toluene fuel-tracer PLIF measurements, such as those shown in Fig. 16, indicate that both zones are fuel rich, as shown in the schematic at 10° ATDC.

As the second-stage ignition process progresses through the period of peak AHRR, the two-zone behavior persists. Fluorescence from deep in the bowl near the head of the jet, likely associated with PAH, becomes more pronounced, but dim fluorescence is still regularly seen from near the reentrant region of the bowl. During this period the mixture within the squish volume also enters second-stage combustion, largely oxidizing the mixture in this region. This picture changes little as the combustion process transitions into a mixing-controlled regime, though by 20° ATDC the fluorescence is dominated by PAH/soot emissions from deep in the bowl. Note that these dominant PAH/soot emissions occur at a similar time as the peak combustion luminosity due to soot in the heavy-duty engine. Later in the cycle, the spatial extent of PAH/soot is reduced, and by 50° ATDC fluorescent emissions from these species are rarely observed. CO concentrations in the mixture leaving the bowl are also low, indicating that late-cycle mixing has effectively completed the oxidation of the richer bowl-mixtures. At this time, the UHC images, though qualitative, indicate that the cylinder center region is an important source of engine-out UHC

emissions, due to globally over-lean mixture and to embedded fuel droplets which are likely surrounded by locally rich mixture pockets. UHC is also found within the squish volume, but tends to be concentrated in the upper cylinder, near the head. The measured CO distributions, however, indicate that CO emissions are dominated by the squish volume. Like UHC, CO tends to be found in higher concentrations in the upper portion of the cylinder.

When injection is retarded further, in-cylinder imaging studies [123] show that the increase in both UHC and CO emissions observed in Fig. 1 is primarily associated with the squish volume. Retarding injection has several effects. First, the descending piston motion results in the jet impacting the bowl higher on the bowl lip, such that more fuel is placed within the squish volume. Second, the increasing reverse squish flow and the increased ignition delay promote faster and more extensive mixing of the fuel near the lip and in the squish volume. Third, the lean-mixture oxidation limit shown in Fig. 23 shifts toward richer mixtures. These factors combine to result in a greater mass of fuel within the squish volume at equivalence ratios that either do not achieve second-stage ignition, or do not complete the second-stage process.

Returning to the early-injection combustion process shown in Fig. 31, the heat release associated with the first stage of ignition peaks near -12.5° ATDC, and is delayed considerably from the injection event as compared to late injection. Fluorescence is observed throughout a region similar in shape to that seen with late injection, though the fuel has penetrated deeper into the bowl and farther into the squish volume. Although liquid fuel is not observed directly at this crank angle, images obtained at -15° indicate that liquid has penetrated nearly to the cylinder wall, and later images of UHC fluorescence strongly suggest the presence of films on the piston top and on the head. Large droplets near the bowl rim are a regular feature of the images, and may be formed by shearing of a liquid film on the piston surface by the squish flow. There is little change to this picture throughout much of the second-stage pre-ignition period, although, as evidenced by images taken later in the cycle, UHC is transferred from the squish volume into the top ring-land crevice.

By -5° ATDC, at the start of the second-stage heat release, a distinct two-zone distribution of fluorescence is again observed deep in the bowl. As with late-injection, fuel tracer PLIF measurements indicate that both zones are associated with fuel rich mixture. Just beyond the peak apparent heat release rate near TDC, second-stage ignition has been reached in much of the mixture deep in the bowl (0° ATDC). At this time, PAH (soot) fluorescence from the head of the jet – now positioned in the inner portion of the bowl – is more pronounced and fluorescence from the outer, re-entrant region of the bowl is considerably reduced. Second-stage ignition is also achieved within the squish volume at this time. Although fuel-rich mixture is measured within the squish volume at the start of second-stage heat release, equivalence ratios are sufficiently low that significant soot or PAH is not formed. While over-lean mixture between the fuel jets is undoubtedly present and leads to regions of unburned H₂CO and HC, strong fluorescence is only observed from regions near liquid films: along the head near the bowl rim and well within the squish volume, on both the head and piston surface.

From this time onward (0° ATDC and later), volume expansion due to heat release within the bowl and the reverse squish flow induced by piston motion push/draw the lean mixture exhibiting continued H₂CO fluorescence into the squish volume, eventually forming a two-zone distribution of UHC and CO. In the inner zone near the cylinder center, the UHC and the CO distribution is dominated by lean mixture within which discrete fuel droplets are embedded, as seen with late-injection. A second zone within the squish volume is generally larger in extent than that observed with

late-injection, and positioned closer to the piston top than to the head. With late-injection, the squish-volume UHC and CO are primarily associated with over-lean mixture that was injected directly into the squish volume. In contrast, with early injection, the squish volume UHC and CO are associated with at least four different sources: lean mixture from the edges of the fuel jets that penetrate directly into the squish volume; lean, bulk-gas mixtures from near the bowl rim and the central clearance volume that are forced/drawn into the squish volume; liquid films and associated rich mixtures on the piston top and surface of the head; and crevice UHC which is trapped in the upper corner of the cylinder and along the cylinder wall. At the light-load operating condition considered here, lean bulk-gas mixtures within the squish volume and the central region of the cylinder are the dominant sources of engine-out UHC and CO emissions.

7. Concluding remarks

The conceptual model extension described herein strictly applies only to the low-load, EGR-diluted, partially premixed conditions outlined in the introduction. For other conditions, the evolution of combustion may be significantly different from that described here. For instance, increasing the injection duration (load) or moving the start of injection closer to conventional diesel timings shortens the ignition dwell and produces a jet that is more similar to the description of the conventional diesel conceptual model, even while achieving LTC conditions due to EGR dilution. Furthermore, other combustion chamber and spray geometries, or multiple injection strategies, may create flow patterns that significantly alter the spatial and temporal development of mixing, ignition, and combustion processes.

Acknowledgments

Support for this research was provided by the U.S. Department of Energy, Office of Vehicle Technologies. The authors' research took place at the Combustion Research Facility, Sandia National Laboratories in Livermore, California. Sandia is a multiprogram laboratory operated by Sandia Corporation, a Lockheed Martin Company, for the United States Department of Energy's National Nuclear Security Administration under contract DE-AC04-94AL85000. The authors express their gratitude to John Dec and Julien Manin of Sandia National Laboratories for their helpful discussions and suggestions for improvement of the article.

Nomenclature

a	ambient (subscript)
d_0	injector orifice diameter
P	pressure
T	temperature
ϕ	equivalence ratio
ρ	density
AEI	after end of injection
AHRR	apparent heat release rate
ASI	after start of injection
ATDC	after top-dead center
CA	crank angle
CO	carbon monoxide
DOI	duration of injection
EGR	exhaust-gas recirculation
glMEP	gross indicated mean effective pressure
H_2CO	formaldehyde
H_2O_2	hydrogen peroxide
HCCI	homogeneous charge compression ignition

HCO	formyl radical
HO_2	hydroperoxy radical
KHP	ketohydroperoxide
LIF	laser-induced fluorescence
LLNL	Lawrence Livermore National Laboratory
LTC	low-temperature combustion
MK	modulated kinetics
NO_x	nitrogen oxides (NO and NO_2)
OH	hydroxyl radical
PAH	polycyclic aromatic hydrocarbons
PCCI	premixed charge compression ignition
PCI	premixed compression ignition
PLIF	planar laser-induced fluorescence
PPCI	partially premixed compression ignition
PM	particulate matter
R	radical
RO_2	peroxy radical
RPM	rotations per minute
SOI	start of injection
TDC	top-dead center
UHC	unburned hydrocarbons

References

- [1] United States Environmental Protection Agency. Fact sheet: diesel exhaust in the United States; 2003. EPA420-F-03-022.
- [2] Council of the European Communities. European Union council directive of 3 December 1987 on the approximation of the laws of the Member States relating to the measures to be taken against the emission of gaseous and particulate pollutants from diesel engines for use in vehicles; 1988. 88/77/EEC.
- [3] Council of the European Communities. Directive 1999/96/EC of the European parliament and of the council of 13 December 1999; 1999. 1999/96/EC.
- [4] European Parliament and the Council of the European Union. Regulation (EC) No 595/2009 of 18 June 2009; 2009.
- [5] DieselNet. <http://www.dieselnet.com/>; 2009.
- [6] US EPA. Summary of current and historical light-duty vehicle emissions standards, www.epa.gov/greenvehicles/detailedchart.pdf; 2010.
- [7] Majewski WA, Khair MK. Diesel emissions and their control. Warrendale, PA: SAE International; 2006.
- [8] Johnson TV. Diesel emission control in review; 2009. SAE Paper 2009-01-0121.
- [9] Plee SL, Ahmad T, Myers JP. Flame temperature correlation for the effects of exhaust gas recirculation on diesel particulate and NO_x emissions. SAE Paper 811195 SAE Transactions 1981;90(4):3738–54.
- [10] Plee SL, Ahmad T, Myers JP, Faeth GM. Diesel NO_x emissions – a simple correlation technique for intake air effects. Proceedings of the Combustion Institute 1982;19:1495–502.
- [11] Ladommatos N, Abdelhalim SM, Zhao H, Hu Z. The dilution, chemical, and thermal effects of exhaust gas recirculation on diesel engine emissions – part 1: effect of reducing inlet charge oxygen; 1996. SAE Paper 961165.
- [12] Kellerer H, Koch R, Wittig S. Measurements of the growth and coagulation of soot particles in a high-pressure shock tube. Combustion and Flame 2000; 120:188–99.
- [13] Dobbins R. Soot inception temperature and the carbonization rate of precursor particles. Combustion and Flame 2002;130:204–14.
- [14] Park C, Appleton JP. Shock-tube measurements of soot oxidation rates. Combustion and Flame 1973;20:369–79.
- [15] Huestis E, Erickson PA, Musculus MPB. In-cylinder and exhaust soot in low-temperature combustion using a wide-range of EGR in a heavy-duty diesel engine. SAE Paper 2007-01-4017 SAE Transactions 2007;116(4):860–70.
- [16] Noehre C, Andersson M, Johansson B, Hultqvist A. Characterization of partially premixed combustion; 2006. SAE Paper 2006-01-3412.
- [17] Colban WF, Miles PC, Oh S. Effect of intake pressure on emissions from an automotive diesel engine operating in low temperature combustion regimes. SAE Paper 2007-01-4063 SAE Transactions 2007;116(4):957–77.
- [18] Ogawa H, Miyamoto N, Shimizu H, Kido S. Characteristics of diesel combustion in low oxygen mixtures with ultra-high EGR; 2006. SAE Paper 2006-01-1147.
- [19] Akihama K, Takatori Y, Inagaki K, Sasaki S, Dean AM. Mechanism of the smokeless rich diesel combustion by reducing temperature. SAE Paper 2001-01-0655 SAE Transactions 2001;110(3):648–62.
- [20] Cheng AS, Upatnieks A, Mueller CJ. Investigation of fuel effects on dilute, mixing-controlled combustion in an optical direct-injection diesel engine. Energy and Fuels 2007;21(4):1989–2002.
- [21] Glassman I. Soot formation in combustion processes. Proceedings of the Combustion Institute 1988;22:295–311.

- [22] Assanis D, Najt PM, Dec JE, Eng JA, Asmus TN, Zhao F. Homogeneous charge compression ignition (HCCI) engines – key research and development issues. Warrendale, PA: SAE; 2003.
- [23] Yang Y, Dec J, Dronniou N, Sjoberg M, Canella W. Partial fuel stratification to control HCCI heat release rates: fuel composition and other factors affecting pre-ignition reactions of two-stage ignition fuels. SAE Paper 2011-01-1359 SAE International Journal of Engines 2011;4:1903–20.
- [24] Keeler B, Shayler PJ. Constraints on fuel injection and EGR strategies for diesel PCCI-type combustion; 2008. SAE Paper 2008-01-1327.
- [25] Kook S, Bae C, Miles PC, Choi D, Pickett LM. The influence of charge dilution and injection timing on low-temperature diesel combustion and emissions. SAE Paper 2005-01-3837 SAE Transactions 2005;114(4):1575–95.
- [26] Hardy WL, Reitz RD. A study of the effects of high EGR, high equivalence ratio, and mixing time on emissions levels in a heavy-duty diesel engine for PCCI combustion; 2006. SAE Paper 2006-01-0026.
- [27] Kitano K, Nishiumi R, Tsukasaki Y, Toshiaki T. Effects of fuel properties on premixed charge compression ignition combustion in a direct injection diesel engine; 2003. SAE Paper 2003-01-1815.
- [28] Kanda T, Hakozaiki T, Uchimoto T, Hatano J, Kitayama N, Sono H. PCCI operation with early injection of conventional diesel fuel. SAE Paper 2005-01-0378 SAE Transactions 2005;114(3):584–93.
- [29] Lee S, Reitz RD. Spray targeting to minimize soot and CO formation in premixed charge compression ignition (PCCI) combustion with a HSDI diesel engine. SAE Paper 2006-01-0918 SAE Transactions 2006;115(3):532–41.
- [30] Kanda T, Hakozaiki T, Uchimoto T, Hatano J, Kitayama N, Sono H. PCCI operation with fuel injection timing set close to TDC; 2006. SAE Paper 2006-01-0920.
- [31] Nevin RM, Sun Y, Gonzalez DMA, Reitz RD. PCCI investigation using variable intake valve closing in a heavy duty diesel engine; 2007. SAE Paper 2007-01-0903.
- [32] Horibe N, Takahashi K, Kee S-S, Ishiyama T, Shioji M. The effects of injection conditions and combustion chamber geometry on performance and emissions of DI-PCCI operation in a diesel engine. SAE Paper 2007-01-1874 SAE Transactions 2007;116(4):387–95.
- [33] Weall A, Collings N. Highly homogeneous compression ignition in a direct injection diesel engine fuelled with diesel and biodiesel. SAE Paper 2007-01-2020 SAE Transactions 2007;116(4):646–60.
- [34] Klingbeil AE, Juneja H, Ra R, Reitz RD. Premixed diesel combustion analysis in a heavy-duty diesel engine. SAE Paper 2003-01-0341 SAE Transactions 2003;112(3):445–59.
- [35] Murata Y, Kusaka J, Odaka M, Daisho Y, Kawano D, Suzuki H, et al. Achievement of medium engine speed and load premixed diesel combustion with variable valve timing; 2006. SAE Paper 2006-01-0203.
- [36] Karra P, Kong S-C. Diesel emission characteristics using high injection pressure with converging nozzles in a medium-duty engine. SAE Paper 2008-01-1085 SAE International Journal of Fuels and Lubricants 2009;1:578–92.
- [37] Lewander M, Ekholm K, Johansson B, Tunestål P, Milovanovic N, Keeler B, et al. Investigation of the combustion characteristics with focus on partially premixed combustion in a heavy duty engine. SAE Paper 2008-01-1658. SAE International Journal of Fuels and Lubricants 2009;1:1056–62.
- [38] Kimura S, Aoki O, Ogawa H, Muranaka S, Enomoto Y. New combustion concept for ultra-clean and high-efficiency small DI diesel engines. SAE Paper 1999-01-3681 SAE Transactions 1999;108(3):2128–37.
- [39] Kimura S, Aoki O, Kitahara Y, Aiyoshizawa E. Ultra-clean combustion technology combining a low-temperature and premixed combustion concept for meeting future emission standards. SAE Paper 2001-01-0200 SAE Transactions 2001;110(4):239–48.
- [40] Cho K, Han M, Sluder CS, Wagner RM, Lilik GK. Experimental investigation of the effects of fuel characteristics on high efficiency clean combustion in a light-duty diesel engine; 2009. SAE Paper 2009-01-2669.
- [41] Miles PC, Choi D, Pickett LM, Singh IP, Henein N. Rate-limiting processes in late-injection, low-temperature diesel combustion regimes. Paper presented at Thermo- and Fluid-Dynamic Processes in Diesel Engines: THIESEL 2004 (Valencia, Spain) 2004.
- [42] Risberg P, Kalghatgi GT, Ångström H-E. Auto-ignition quality of diesel-like fuels in HCCI engines. SAE Paper 2005-01-2127 SAE Transactions 2005;114(4):883–93.
- [43] de Ojeda W, Zoldak P, Espinosa R, Kumar R. Development of a fuel injection strategy for diesel LTC; 2008. SAE Paper 2008-01-0057.
- [44] Dec JE. A conceptual model of D.I. diesel combustion based on laser-sheet imaging. SAE Paper 970873 SAE Transactions 1997;106(3):1319–48.
- [45] Bruneaux G. A study of soot cloud structure in high pressure single hole common rail diesel injection using multi-layered laser-induced incandescence. 5th International Symposium on Diagnostics and Modeling of Combustion in Internal Combustion Engines (Comodia) (Nagoya, Japan) 2001; 622–30.
- [46] Taschek M, Koch P, Egermann J, Leipertz A. Simultaneous optical diagnostics of HSDI diesel combustion processes; 2005. SAE Paper 2005-01-3845.
- [47] Kosaka H, Aizawa T, Kamimoto T. Two-dimensional imaging of ignition and soot formation processes in a diesel flame. International Journal of Engine Research 2005;6(1):21–42.
- [48] Idicheria CA, Pickett LM. Formaldehyde visualization near lift-off location in a diesel jet. SAE Paper 2006-01-3434 SAE Transactions 2006;115(4):683–95.
- [49] Pickett LM, Siebers DL. Soot formation in diesel fuel jets near the lift-off length. International Journal of Engine Research 2006;6:103–30.
- [50] Bruneaux G. Combustion structure of free and wall-impinging diesel jets by simultaneous laser-induced fluorescence of formaldehyde, poly-aromatic hydrocarbons, and hydroxides. International Journal of Engine Research 2008;9:249–65.
- [51] Flynn PF, Durrett RP, Hunter GL, zur Loye AO, Akenyemi OC, Dec JE, et al. Diesel combustion: an integrated view combining laser diagnostics, chemical kinetics, and empirical validation. SAE Paper 1999-01-0509 SAE Transactions 1999;108(3):587–600.
- [52] Naber JD, Siebers DL. Effects of gas density and vaporization on penetration and dispersion of diesel sprays. SAE Paper 960034 SAE Transactions 1996;105(3):82–111.
- [53] Ricou FP, Spalding DB. Measurements of entrainment by axisymmetrical turbulent jets. Journal of Fluid Mechanics 1961;11(1):21–32.
- [54] Pope SB. Turbulent flows. Cambridge University Press; 2000.
- [55] Pickett LM, Manin J, Genzale CL, Siebers DL, Musculus MPB, Idicheria CA. Relationship between diesel fuel-jet vapor penetration/dispersion and local fuel mixture-fraction. SAE Paper 2011-01-0686 SAE International Journal of Engines 2011;4:764–99.
- [56] Siebers DL. Scaling liquid-phase fuel penetration in diesel sprays based on mixing-limited vaporization. SAE Paper 1999-01-0528 SAE Transactions 1999;108(3):703–28.
- [57] Canaan RE, Dec JE, Green RM. The influence of fuel volatility on the liquid-phase fuel penetration in a heavy-duty D.I. diesel engine. SAE Paper 980510 SAE Transactions 1998;107(3):583–602.
- [58] Desantes JM, López JJ, Garcia J, Pastor JM. Evaporative diesel spray modeling. Atomization and Sprays 2007;17:193–231.
- [59] Dec JE, Espy C. Chemiluminescence imaging of autoignition in a D.I. diesel engine. SAE Paper 982685 SAE Transactions 1998;107(3):2230–54.
- [60] Dec JE, Espy C. Ignition and early soot formation in a D.I. diesel engine using multiple 2-D imaging diagnostics. SAE Paper 950456 SAE Transactions 1995;104(3):853–75.
- [61] Higgins B, Siebers D. Measurement of the flame lift-off location on D.I. diesel sprays using OH chemiluminescence. SAE Paper 2001-01-0918 SAE Transactions 2001;110(3):739–53.
- [62] Siebers DL, Higgins BS. Flame lift-off on direct-injection diesel sprays under quiescent conditions. SAE Paper 2001-01-0530 SAE Transactions 2001;110(3):400–21.
- [63] Pickett LM, Siebers DL. Orifice diameter effects on diesel fuel jet flame structure. Proceedings of the Fall Technical Conference of the ASME Internal Combustion Engine Division 2001; ICE 37–41.
- [64] Singh SS, Reitz RD, Musculus MP, Lachaux T. Validation of engine combustion models against detailed in-cylinder optical diagnostics data for a heavy-duty compression-ignition engine. International Journal of Engine Research 2007;8(1):97–126.
- [65] Siebers DL. Liquid-phase fuel penetration in diesel sprays. SAE Paper 980809 SAE Transactions 1998;107(3):1205–27.
- [66] Espy C, Dec JE. The effect of TDC temperature and density on the liquid-phase fuel penetration in a D.I. diesel engine. SAE Paper 952456 SAE Transactions 1995;104(4):1400–16.
- [67] Kook S, Pickett LM, Musculus MPB, Gehmlich RK. Influence of diesel injection parameters on end-of-injection liquid length recession. SAE Paper 2009-01-1356 SAE International Journal of Engines 2009;2:1194–210.
- [68] Atassi N, Boree J, Charnay G. Transient behavior of an axisymmetric turbulent jet. Applied Scientific Research 1993;51:137–42.
- [69] Boree J, Atassi N, Charnay G. Phase averaged velocity field in an axisymmetric jet subject to a sudden velocity decrease. Experiments in Fluids 1996;21:447–56.
- [70] Boree J, Atassi N, Charnay G, Taubert L. Measurements and image analysis of the turbulent field in an axisymmetric jet subject to a sudden velocity decrease. Experimental Thermal and Fluid Science 1997;14:45–51.
- [71] Breidenthal R. The turbulent exponential jet. Physics of Fluids 1986;29(8):2346–7.
- [72] Breidenthal RE. The effect of acceleration on turbulent entrainment. Physica Scripta 2008;T132:1–5.
- [73] Johari H, Padua R. Dilution and mixing in an unsteady jet. Experiments in Fluids 1997;23(4):272–80.
- [74] Zhang Q, Johari H. Effects of acceleration on turbulent jets. Physics of Fluids 1996;8(8):2185–95.
- [75] Musculus MPB, Kattke K. Entrainment waves in diesel jets. SAE Paper 2009-01-1355 SAE International Journal of Engines 2009;2:1170–93.
- [76] Hu B, Musculus MPB, Oefelein JC. The influence of large-scale structures on entrainment in a decelerating transient turbulent jet revealed by large eddy simulation. Physics of Fluids 2011;24:045106.
- [77] Kook S, Pickett LM, Musculus MPB, Gehmlich RK. Liquid-phase diesel spray penetration during end-of-injection transient. 7th COMODIA (Japan) 2008.
- [78] Musculus MPB, Lachaux T, Pickett LM, Idicheria CA. End-of-injection overmixing and unburned hydrocarbon emissions in low-temperature-combustion diesel engines. SAE Paper 2007-01-0907 SAE Transactions 2007;116(3):515–41.
- [79] Bruneaux G. Mixing process in high pressure diesel jets by normalized laser induced exciplex fluorescence part I: free jet. SAE Paper 2005-01-2100 SAE Transactions 2005;114(3):1444–61.
- [80] Martin GC, Mueller CJ, Milam DM, Radovanovic MS, Gehrke CR. Early direct-injection, low-temperature combustion of diesel fuel in an optical engine utilizing a 15-hole, dual-row, narrow-included-angle nozzle. SAE Paper 2008-01-2400 SAE International Journal of Engines 2008;1:1057–82.

- [81] Kashdan JT, Mendez S, Bruneaux G. On the origin of unburned hydrocarbon emissions in a wall-guided, low NO_x diesel combustion system. SAE Paper 2007-01-1836 SAE Transactions 2007;116(4):234–57.
- [82] Lechner GA, Jacobs TJ, Chryssakis CA, Assanis D, Siewert RM. Evaluation of a narrow spray cone angle, advanced injection timing strategy to achieve partially premixed compression ignition combustion in a diesel engine. SAE Paper 2005-01-0167 SAE Transactions 2005;114(3):394–404.
- [83] Shimazaki N, Tsurushima T, Nishimura T. Dual mode combustion concept with premixed diesel combustion by direct injection near top dead center. SAE Paper 2003-01-0742 SAE Transactions 2003;112(3):1060–9.
- [84] Hotta Y, Inayoshi M, Nakakita K, Fujiwara K, Sakata I. Achieving lower exhaust emissions and better performance in an HSDI diesel engine with multiple injection. SAE Paper 2005-01-0928 SAE Transactions 2005;114(3):883–98.
- [85] Pickett LM, Kook S, Williams TC. Transient liquid penetration of early-injection diesel sprays. SAE Paper 2009-01-0839 SAE International Journal of Engines 2009;2:439–59.
- [86] Malbec L-M, Bruneaux G. Study of air entrainment of multi-hole diesel injection by particle image velocimetry – effect of neighboring jets interaction and transient behavior after end of injection. SAE Paper 2010-01-0342 SAE International Journal of Engines 2010;3:107–23.
- [87] Kim T, Ghandhi JB. Quantitative 2-D fuel vapor concentration measurements in an evaporating diesel spray using the exciplex fluorescence method. SAE Paper 2001-01-3495 SAE Transactions 2001;110(3):2165–81.
- [88] Singh S, Musculus MPB. Numerical modeling and analysis of entrainment in turbulent jets after the end of injection. Journal of Fluids Engineering 2010;132(8):081203.
- [89] Obokata T, Hashimoto T. LDA analysis of diesel spray and entrainment air flow. 2nd Comodida (Kyoto, Japan) 1990; 231–6.
- [90] Genzale CL, Reitz RD, Musculus MPB. Effects of piston bowl geometry on mixture development and late-injection low-temperature combustion in a heavy-duty diesel engine. SAE Paper 2008-01-1330 SAE International Journal of Engines 2008;1(1):913–37.
- [91] Chevron Products Company. Diesel fuels technical review FTR-2; 1998.
- [92] Patel A, Kong SC, Reitz RD. Development and validation of a reduced reaction mechanism for HCCI engine simulations; 2004. SAE Paper 2004-01-0558.
- [93] Curran HJ, Gaffuri P, Pitz WJ, Westbrook CK. A comprehensive modeling study of n-heptane oxidation. Combustion and Flame 1998;114:149–77.
- [94] Curran HJ, Gaffuri P, Pitz WJ, Westbrook CK. A comprehensive modeling study of iso-octane oxidation. Combustion and Flame 2002;129:253–80.
- [95] Smith GP, Golden DM, Frenklach M, Moriarty NW, Eiteneer B, Goldenberg M, et al. GRI-mech 3.0, http://www.me.berkeley.edu/gri_mech/; 2005.
- [96] Kee RJ, Rupley FM, Miller JA. Sandia National Laboratories Technical Report SAND 89-8009; 1989.
- [97] Westbrook CK. Chemical kinetics of hydrocarbon ignition in practical combustion systems. Proceedings of the Combustion Institute 2000;28:1563–77.
- [98] Singh S, Musculus MPB, Reitz RD. Mixing and flame structures inferred from OH-PLIF for conventional and low-temperature diesel engine combustion. Combustion and Flame 2009;156(10):1898–908.
- [99] Brackmann C, Nygren J, Bai X, Li ZS, Bladh H, Axelson B, et al. Laser-induced fluorescence of formaldehyde in combustion using third harmonic Nd:YAG laser excitation. Spectrochimica Acta – A 2003;59(14):3347–56.
- [100] de Francqueville L, Thirouard B, Cherel J. Investigating unburned hydrocarbon (UHC) emissions in a GDI engine (homogeneous and stratified modes) using formaldehyde LIF and fast-FID measurements in the exhaust port; 2007. SAE Paper 2007-01-4029.
- [101] Hildingsson L, Persson H, Johansson B, Collin R, Nygren J, Richter M, et al. Optical diagnostics of HCCI and low-temperature diesel using simultaneous 2-D PLIF of OH and formaldehyde. SAE Paper 2004-01-2949 SAE Transactions 2004;113(4):1809–16.
- [102] Richter M, Collin R, Nygren J, Aldén M, Hildingsson L, Johansson B. Studies of the combustion process with simultaneous formaldehyde and OH PLIF in a direct-injected HCCI engine. JSME International Journal B 2005;48(4):701–7.
- [103] Sarner G, Richter M, Aldén M, Hildingsson L, Hultqvist A, Johansson B. Simultaneous PLIF measurements for visualization of formaldehyde- and fuel-distributions in a DI HCCI engine; 2005. SAE Paper 2005-01-3869.
- [104] Kosaka H, Drewes VH, Catalfamo L, Aradi A, Iida N, Kamimoto T. Two-dimensional imaging of formaldehyde formed during the ignition process of a diesel fuel spray; 2000. SAE Paper 2000-01-0236.
- [105] Musculus MPB. Multiple simultaneous optical diagnostic imaging of early-injection low-temperature combustion in a heavy-duty diesel engine. SAE Paper 2006-01-0079 SAE Transactions 2006;115(3):83–110.
- [106] Genzale CL, Reitz RD, Musculus MPB. Optical diagnostics and multi-dimensional modeling of spray targeting effects in late-injection low-temperature diesel combustion. SAE Paper 2009-01-2699 SAE International Journal of Engines 2009;2(2):150–72.
- [107] Musculus MPB, Lachaux T. Two-stage ignition and unburned fuel emissions for heavy-duty diesel low-temperature combustion of neat n-heptane. 5th US Combustion Meeting (San Diego) 2007.
- [108] Pickett LM. Engine combustion network, <http://www.sandia.gov/ecn/>; 2009.
- [109] Petersen BR, Sahoo D, Miles PC. Equivalence ratio distributions in a light-duty diesel engine operating under partially premixed conditions. SAE Paper 2012-01-0692 SAE International Journal of Engines 2012;5:526–37.
- [110] Petersen BR, Ekoto IW, Miles PC. Effect of fuel properties on UHC and CO emissions from partially premixed combustion. Proceedings of the 10th International Congress on Engine Combustion Processes and Modern Techniques (Munich, Germany) 2011.
- [111] Dec JE, Coy EB. OH radical imaging in a DI diesel engine and the structure of the early diffusion flame. SAE Paper 960831 SAE Transactions 1996;105(3):1127–48.
- [112] Bruneaux G, Maligne D. Study of the mixing and combustion processes of consecutive short double diesel injections. SAE Paper 2009-01-1352 SAE International Journal of Engines 2009;2(1):1151–69.
- [113] Bobba MK, Musculus MPB. Effect of ignition delay on in-cylinder soot characteristics of a heavy duty diesel engine operating at low temperature conditions. SAE Paper 2009-01-0946 SAE International Journal of Engines 2009;2:911–24.
- [114] Aronsson U, Chartier C, Andersson Ö, Johansson B, Sjöholm J, Wellander R, et al. Analysis of EGR effects on the soot distribution in a heavy duty diesel engine using time-resolved laser induced incandescence. SAE Paper 2010-01-2104 SAE International Journal of Engines 2010;3:137–55.
- [115] Idicheria CA, Pickett LM. Ignition, soot formation, and end-of-combustion transients in diesel combustion under high-EGR conditions. International Journal of Engine Research 2011;12:376–92.
- [116] Rizk W. Experimental studies of the mixing processes and flow configurations in two-cycle engine scavenging. Proceedings of the Institution of Mechanical Engineers E 1958;172:417–24.
- [117] Dec JE, Canaan RE. PLIF imaging of NO formation in a DI diesel engine. SAE Paper 980147 SAE Transactions 1998;107(3):176–204.
- [118] Ekoto IW, Colban WF, Miles PC, Aronsson U, Andersson Ö, Park SW, et al. UHC and CO emissions sources from a light-duty diesel engine undergoing late-injection low-temperature combustion. Proceedings of the ASME Internal Combustion Engine Division 2009 Fall Technical Conference (Lucerne, Switzerland) 2009; ICEF2009–14030.
- [119] Ekoto IW, Colban WF, Miles PC, Park SW, Foster DE, Reitz RD. Sources of UHC emissions from a light-duty diesel engine operating in a partially premixed combustion regime. SAE Paper 2009-01-1446 SAE International Journal of Engines 2009;2(1):1265–89.
- [120] Dec JE, Kelly-Zion PL. The effects of injection riming and diluent addition on late-combustion soot burnout in a DI diesel engine based on simultaneous 2-D imaging of OH and soot. SAE Paper 2000-01-0238; 2000.
- [121] Pires da Cruz A, Dumas JP, Bruneaux G. Two-dimensional in-cylinder soot volume fractions in diesel low temperature combustion mode. SAE Paper 2011-01-1390 SAE International Journal of Engines 2011;4:2023–47.
- [122] Boariuci A, Foucher F, Mounaim-Rousselle C, Pajot O. Estimate measurement of soot diameter and volume fraction inside the bowl of a direct-injection-compression-ignition engine: effect of the exhaust gas recirculation. Combustion Science and Technology 2007;179:1631–48.
- [123] Ekoto IW, Colban WF, Miles PC, Park SW, Foster DE, Reitz RD, et al. UHC and CO emissions sources from a light-duty diesel engine undergoing dilution-controlled low-temperature combustion. 9th International Conference on Engines and Vehicles (Naples, Italy) 2009.
- [124] Ekoto IW, Colban WF, Kim D, Miles PC. Distribution of unburned hydrocarbons for low temperature light-duty diesel combustion. 7th COMODIA; 2008.
- [125] Idicheria CA, Pickett LM. Effect of EGR on diesel premixed-burn equivalence ratio. Proceedings of the Combustion Institute 2007;31:2931–8.
- [126] Lachaux T, Musculus MPB. In-cylinder unburned hydrocarbon visualization during low-temperature compression-ignition engine combustion using formaldehyde PLIF. Proceedings of the Combustion Institute 2007;31:2921–9.
- [127] Petersen BR, Ekoto IW, Miles PC. Optical investigation of UHC and CO sources from biodiesel blends in a light-duty diesel engine operating in a partially premixed combustion regime. SAE Paper 2010-01-0862 SAE International Journal of Fuels and Lubricants 2010;3:414–34.
- [128] Colban W, Kim D, Miles PC, Oh S, Opat R, Krieger R, et al. A detailed comparison of emissions and combustion performance between optical and metal single-cylinder diesel engines at low temperature combustion conditions. SAE Paper 2008-01-1066 SAE Transactions 2008;117(4):505–19.
- [129] Greeves G, Khan IM, Wang CHT, Fenne I. Origins of hydrocarbon emissions from diesel engines. SAE Paper 770259 SAE Transactions 1977;86(2):1235–51.
- [130] Koci CP, Ra Y, Krieger R, Andris M, Foster DE, Siewert RM, et al. Detailed unburned hydrocarbon investigations in a highly-dilute diesel low temperature combustion regime. SAE Paper 2009-01-0928 SAE International Journal of Engines 2009;2(1):858–79.
- [131] Chartier C, Andersson Ö, Johansson B, Musculus MPB, Bobba MK. Effects of post-injection strategies on near-injector over-lean mixtures and unburned hydrocarbon emissions in a heavy-duty optical diesel engine. SAE Paper 2011-01-1383 SAE International Journal of Engines 2011;4(1):1978–92.
- [132] Ra Y. Private communication. University of Wisconsin; 2009.
- [133] Colban W, Ekoto I, Kim D, Miles PC. In-cylinder PIV measurements in an optical light-duty diesel at LTC conditions. THIESEL 2008.
- [134] Siewert RM. Spray angle and rail pressure study for low NO_x diesel combustion; 2007. SAE Paper 2007-01-0122.
- [135] Opat R, Ra Y, Gonzalez MA, Krieger R, Reitz RD, Foster DE, et al. Investigation of mixing and temperature effects on HC/CO emissions of highly dilute low temperature combustion in a light duty diesel engine; 2007. SAE Paper 2007-01-0193.
- [136] Cursente V, Pacaud P, Mendez S, Knop P. System approach for compliance with full load targets on a wall guided diesel combustion system. SAE Paper 2008-01-0840 SAE International Journal of Engines 2008;1:501–13.